UNIVERSITY OF CALIFORNIA

Santa Barbara

Multiscale mechanics of bioinspired dry adhesives

A dissertation submitted in partial satisfaction of the

requirements for the degree Doctor of Philosophy

in Mechanical Engineering

by

Jamie A. Booth

Committee in charge:

Professor Kimberly L. Foster, Chair

Professor Matthew R. Begley

Professor Robert M. McMeeking

Professor Megan T. Valentine

June 2019

The dissertation of Jamie A. Booth is approved.

_____

Matthew R. Begley

_____

Robert M. McMeeking

_____

Megan T. Valentine

_____

Kimberly L. Foster, Committee Chair

May 2019

Multiscale mechanics of bioinspired dry adhesives

ACKNOWLEDGEMENTS

This work ought to have a very long list of authors, encompassing the colleagues, friends, and family without whom I would not have been able to pursue (never mind complete) my doctoral studies. Repaying this debt of gratitude will undoubtedly take me far longer than was required to complete this document.

Firstly, I must thank Professor Kimberly Foster, who welcomed me in to her research group with open arms and has since been a source of support in the most trying of times. Members of the Foster Group, past and present, have been a valuable sounding board for ideas and have made it a pleasure to come to work every day. A ‘yours aye’ goes to Professor Robert McMeeking, who has been a beacon of knowledge with a familiar brogue, and with whom it has been an honor to work. Professors Matthew Begley and Megan Valentine have been a constant source of guidance, for which I am extremely grateful. I would also like to thank the late Professor Jacob Israelachvili, who graciously put forth his time in service of this work.

My collaborators deserve special acknowledgement. Mattia Bacca played an important role in guiding the direction of this work. My colleagues at the Leibniz Institute for New Materials have not only immeasurably improved the quality of this research, but have been such tremendous hosts during my time in Germany.

I would like to thank the staff of the Mechanical Engineering Department, particularly Laura Reynolds, Josh Johnson, and Dave Bothman, who were nothing but patient and

accommodating as I littered their inboxes with streams of questions. Serving the students of the department as a teaching assistant and instructor has been a welcome distraction from research, and their enthusiasm has allowed me to discover my passion as an engineering educator.

My friends in Santa Barbara have made me feel truly at home in my time here, and ‘the biyz’ have provided comic relief when it was needed most. My family, both Scottish and Armenian alike, have provided me with immeasurable support and have asked for nothing in return. I would particularly like to thank my parents, to whom I apologize for the occasional lack of phone calls. Their selflessness in support of my goals knows no bounds.

Finally, I would like to thank my wife Calia, who is my source of inspiration in life. I would not have made it through this endeavor were it not for her unending patience and love.

VITA OF JAMIE A. BOOTH
June 2019

Research interests

Adhesion, contact and fracture mechanics, biomimetics, microarchitectured materials

Education

University of California, Santa Barbara, Santa Barbara, CA USA

Ph.D. Mechanical Engineering, June 2019

Certificate in College and University Teaching, June 2019

University of Glasgow, Glasgow, Scotland UK

M.Eng, 1st Class Honors, Mechanical Engineering, June 2013

Selected journal articles

Jamie A. Booth, Mattia Bacca, Robert M. McMeeking, Kimberly L. Foster 'Benefit of backing layer compliance in fibrillar adhesive patches - resistance to peel propagation in presence of interfacial misalignment', *Advanced Materials Interfaces* (2018) 1800272 DOI: 10.1002/admi.201800272

Nicholas Cadirov, **Jamie A. Booth**, Kimberly L. Foster, and Jacob N. Israelachvili, 'Influence of humidity on grip and release adhesion mechanisms for gecko-inspired microfibrillar surfaces', *ACS Applied Materials and Interfaces* 9(16) (2017) 14497–14505 DOI: 10.1021/acsami.7b01624

Mattia Bacca*, **Jamie A. Booth***, Kimberly L. Foster, Robert M. McMeeking, 'Load sharing in bioinspired fibrillar adhesives with backing layer interactions and interfacial misalignment', *Journal of the Mechanics and Physics of Solids* 96 (2016) 428-444 DOI: 10.1016/j.jmps.2016.04.008

*Equal contribution

Selected conference presentations

Jamie A. Booth, Mattia Bacca, Robert M. McMeeking, Kimberly L. Foster, 'Adhesive load sharing in arrays of bioinspired fibrils', ASME Conference on Smart Materials, Intelligent Systems, and Adaptive Structures (SMASIS) 2016, Stowe, VT, USA, September 28th-30th 2016

Teaching experience

University of California, Santa Barbara, Santa Barbara, CA USA

Instructor

- Engineering Mechanics: Dynamics, Summer 2017

Guest Instructor

- Physics of Transducers, Fall 2014

Teaching Assistant

- Strength of Materials, Winter 2019
- Design and Analysis of Structures, Fall 2018
- Engineering Mechanics: Statics, Fall 2016
- Mechanical Engineering Design, Winter 2014
- Design and Analysis of Structures, Fall 2013

Selected service

Gordon Research Seminar, Science of Adhesion 2019, South Hadley, MA USA

Co-chair, July 2017 - Present

Virtual Humboldt Cluster on the Mechanics and Physics of Adhesion and Grip, Santa Barbara, CA USA

Workshop co-organizer, Modeling on adhesion, grip, and related topics, October 2018

Selected honors

UCSB Mechanical Engineering Department Outstanding Teaching Assistant 2018-19

UCSB Graduate Student Association Excellence in Teaching Award Nominee 2014 and 2017

IMechE Certificate for Best Masters Project 2013

IMechE Fredrick Barnes Waldron Prize for Best Mechanical Engineering Graduate 2013

University of Glasgow Melville and Sheila Tuck Prize for Best Mechanical Engineering Graduate 2013

University of Glasgow George Harvey Prize for Best Graduate in Dynamics 2013

ABSTRACT

Multiscale mechanics of bioinspired dry adhesives

by

Jamie A. Booth

The adhesive systems of climbing animals have served as inspiration for a new class of temporary adhesive utilizing surface microstructure in place of intrinsically soft and viscoelastic materials. These have the potential to address requirements for robust, releasable, and reusable bonding. Efforts to characterize synthetic dry adhesives, as well as to scale adhesive patches to large areas while maintaining performance, necessitate consideration of features of the system across length scales. This work addresses two topics which require that the behavior of individual microfibrils be accounted for explicitly within large-scale loading configurations.

Under ideal conditions the strength of fibril arrays is known to be controlled by an array edge load concentration associated with compliance of the backing layer. Laboratory experiments have revealed that the strength is sensitive to the alignment of the adhesive and substrate surfaces, however no systematic investigation of the response to these perturbations in the loading configuration has been performed. A contact mechanics model is developed, considering the role of backing layer compliance in addition to misalignment. A monotonic decay in the adhesive strength of the array with increasing misalignment angle is confirmed. More interestingly, regimes of dominance of backing layer compliance and misalignment in

control of the adhesive strength are revealed. Where circumferential detachment gives way to peel-like detachment, compliance of the backing layer is found to be beneficial to performance. This is the result of shielding of the peel-front load concentration by backing layer deformation. Subsequent experimental characterization of a mushroom-tipped synthetic fibril array shows that this regime is dominant for misalignment angles of just ~ 0.2° over a patch size of 2 mm. These results can be utilized to anticipate the performance of fibrillar adhesive patches on flat surfaces without precise control of alignment, or of sub-arrays within a larger hierarchy where surface undulations may lead to local misalignment.

While the potential importance of the variability in fibril adhesive strength in controlling the performance of microstructure arrays has been highlighted in past work, there has been no effort to systematically characterize the strength distribution or understand its effect on performance further. The capabilities of an experimental platform with in-situ contact visualization are leveraged to provide strength data on a fibril-by-fibril basis. A framework is developed, based upon the statistical theory of fracture, allowing for the decoupling of two defect populations and assessment of the impact of fabrication imperfections on performance. A subsequent theoretical investigation is performed with a view to understanding the combined effect of variability in fibril adhesive strength and load concentrations at the array scale. It is shown that, dependent on the severity of the load concentration, increased variability in fibril adhesive strength can modulate the influence of load concentrations and lead to independence of the adhesive strength of the array from properties such as backing layer compliance or substrate curvature. This is highly significant, given that the severity of load concentrations is a key factor in designing hierarchical structures for adhesive strength.

Some of the content in Chapter 3 is reprinted with permission from: Mattia Bacca, Jamie A. Booth, Kimberly L. Foster, Robert M. McMeeking, 'Load sharing in bioinspired fibrillar adhesives with backing layer interactions and interfacial misalignment', *Journal of the Mechanics and Physics of Solids* 96 (2016) 428-444 DOI: 10.1016/j.jmps.2016.04.008

Some of the content in Chapter 4 is reprinted with permission from: Jamie A. Booth, Mattia Bacca, Robert M. McMeeking, Kimberly L. Foster 'Benefit of backing layer compliance in fibrillar adhesive patches - resistance to peel propagation in presence of interfacial misalignment', *Advanced Materials Interfaces* (2018) 1800272 DOI: 10.1002/admi.201800272

TABLE OF CONTENTS

Chapter 1

Introduction

1.1 Motivation

Temporary bonding applications often rely on pressure sensitive adhesives (PSAs) [1, 2]. Comprised of intrinsically soft and viscoelastic polymers, with elastic modulii below 100 kPa, they are capable of conformation to surface asperities leading to the generation of molecular contact. This permits utilization of universal intermolecular forces for adhesion, rather than any material-specific bonding or chemical reaction. Cavitation and fibrillation [3, 4], as well as the viscous response of the material [5] can increase the energy requirement for separation above the intrinsic levels of the intermolecular interaction. This allows the load, applied remote to the contact or interface, to be increased to higher levels without failure of the joint. However, the use of these materials has its drawbacks. Their viscoelastic nature can render PSAs prone to creep when subject to loading over extended periods of time. Their low stiffness means that the surfaces are often fouled by contaminant particles, self-adhere, or leave residues on the target substrate, all of which act to limit their reusability.

Other strategies for temporary bonding, particularly relevant in the industrial handling of components, include mechanical gripping, suction or vacuum, electrostatic and

electromagnetic attraction [6]. Each approach possesses specific limitations. Vacuum gripping, for example, is not possible on permeable objects or in reduced pressure environments. Many of these systems require bulky power-consuming external systems, which limit their usefulness in miniaturized systems, in mobile applications, or in weight-critical fields such as space travel.

Together, these technological drivers have led to the pursuit of 'dry adhesives' [7-23], using intrinsically stiffer materials and thus being capable of temporary bonding with enhanced reusability and reversibility. As is increasingly common in engineering, to solve this complex technical problem researchers have looked to biology, and the adhesive systems of insects [24] and reptiles [25], for inspiration. As the largest of the species with adhesive toe-pads, the Tokay (*Gekko*) gecko has received the greatest attention. It possesses the ability to climb on vertical and inverted surfaces at speeds up to $1\ \mathrm{m/s}$ [26], supporting a body mass of $\sim 50\ \mathrm{g}$ on a pad area of $\sim 220\ \mathrm{mm}^2$ [25]. This suggests that the gecko can transition quickly between strong attachment and easy detachment. It wasn't until the late 19th and early 20th centuries that advances in microscopy permitted first observation of the hierarchical microstructure of the gecko toe-pad [27-29], ultimately allowing the mechanisms facilitating this sticking ability to be investigated.

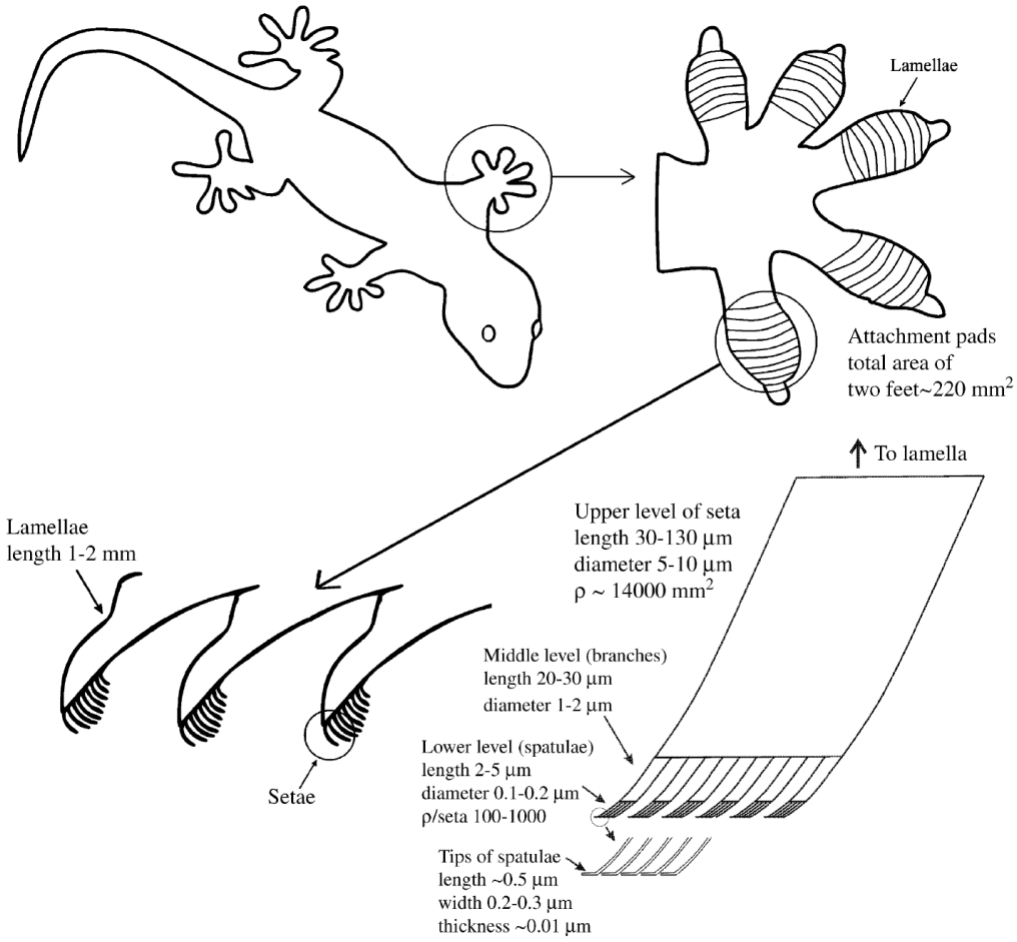

Figure 1.1. Features of the adhesive system of the *Gekko gecko* and their approximate characteristic dimensions. Reproduced with permission from [30].

Figure 1.1 is a schematic representation of the features of the Tokay gecko's adhesive system. Its functionality begins with the skeletal and muscular features of the body (length scale $\sim 10 - 100$ mm), responsible for actuation and control of the feet and toes. Each toe-pad bears overlapping scales with modified geometry, known as lamellae (length scale ~ 1 mm). Distributed across the lamellae are arrays of setal fibers (length scale $\sim 10 - 100$ µm). Typical setae are $5 - 10$ µm in diameter at their proximal end, tapering to 2 µm in diameter as they branch. The setae are curved such that branches approach the contacting surface normally.

Branches are terminated by triangular spatulae (length scale ~ 100 nm), approximately $100 - 1000$ per seta. The outer surface of the lamellae, including the setal fibers, are comprised of β-keratin [31]. This protein has a relatively high bulk stiffness (~ 1 GPa [32]). This is thought to be of fundamental importance to the anti-fouling properties of the toe pad [33], permitting attachment over tens of thousands of repeat cycles without loss of performance [34]. The question therefore becomes, how can the gecko generate sufficiently high adhesive forces using this intrinsically stiff material?

At the root of any adhesion problem is a source of bonding or interaction between the substrate and the adhesive surface. After a lengthy debate surrounding the potential source of attractive forces between gecko toe-pad structures and the substrate [29, 35-37] , it is now widely accepted that the universal intermolecular van der Waals interaction is the dominant contributor [38]. However, the mere existence of these surface-chemistry-independent forces is insufficient to ensure strong attachment to substrates of considerable roughness and curvature, over areas sufficient to bear loads of engineering significance. It is the mechanics associated with the hierarchical fibrillar structure which are key to addressing these challenges.

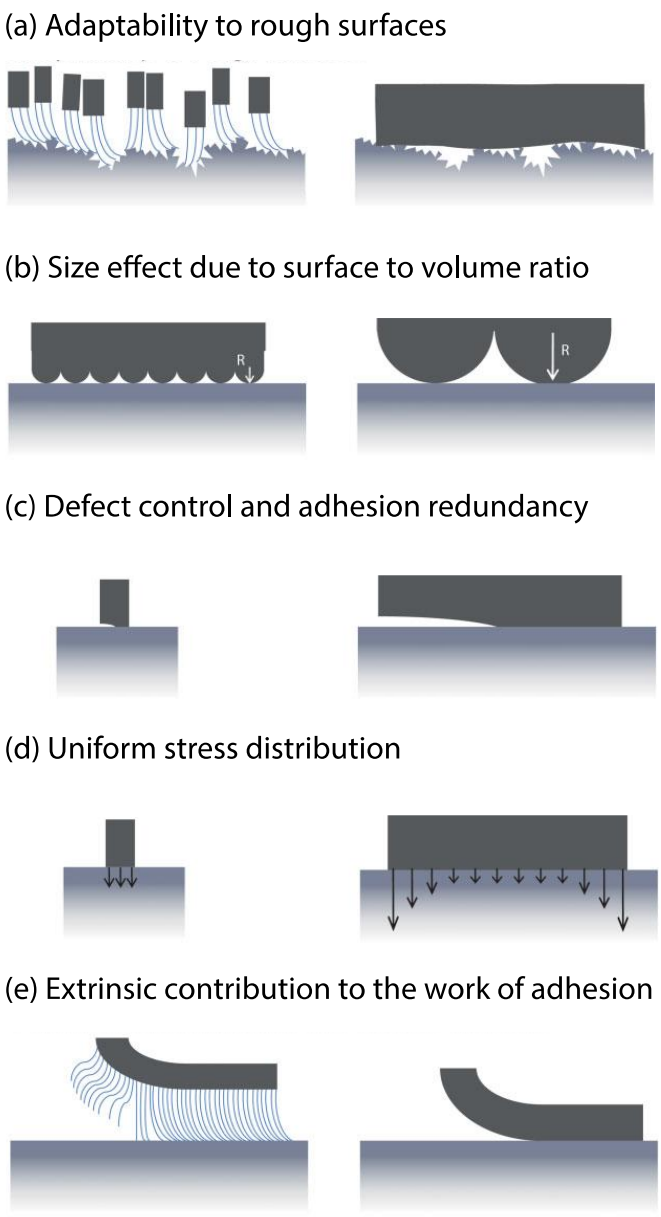

Figure 1.2. Summary of the proposed cooperative adhesion enhancement mechanisms for a hierarchical fibrillar microstructure. Adapted with permission from [39].

Figure 1.2 is a schematic summary of the multiple cooperative mechanisms of adhesion enhancement which have been proposed [39]. First consider the attachment process, where it is vital that intimate molecular contact be generated over a large area if short-ranged

intermolecular forces are to be harnessed. The slender fibrillar structures possess low bending stiffness, rendering the effective modulus during attachment many orders of magnitude lower than the intrinsic modulus of the β-keratin [30, 40-43]. The strain energy stored in the adhesive during preload, which can act to drive detachment, is minimal. The fibril hierarchy allows for conformation to surface roughness across length scales, generating contact with the spatula tips over the projected area of the toe-pads (Figure 1.2a).

Even when intimate molecular contact is generated at terminal sub-contacts, stress concentrations at the interface have the potential to reduce the adhesive strength. Intermolecular forces are overcome locally leading to the nucleation and propagation of interfacial defects and the detachment of the fibril. The strength of the sub-contact is reduced as only a fraction of the interface supports near maximum stresses at any instant. This is addressed through the use of small sub-contacts, which can enhance adhesive strength by increasing the surface-to-volume ratio (surface energy gain vs. strain energy cost) [44] (Figure 1.2b), as well as limiting the size of interfacial defects [45] (Figure 1.2c) and reducing interfacial stress concentrations at these defects and at the sub-contact edge [46-48]. If the size is reduced below a critical value then the interfacial stress will be approximately uniform, and strength will saturate at the intrinsic maximum associated with the adhesive interaction (Figure 1.2d).

As we view the larger scale features of the system, and the projected view of the contact area increases, load concentrations among subsets of fibrils are possible due to variations in displacement across the contact and at the contact edge. These become more severe as the

dimensions of the contact increase. If fibrils detach then an array-scale defect is formed, ultimately reducing the strength of the contact. However, fibrils are compliant can deform elastically, reducing the associated concentration of load. As they detach, the strain energy stored in the fibril is not available to drive the detachment of neighboring fibrils. In this way they provide a contribution to the toughness which is inversely proportional to their axial stiffness [40, 46, 49, 50] (Figure 1.2e). The utilization of hierarchy ensures that this mechanism prevails across length scales [51], allowing short-ranged intermolecular forces to be harnessed across macroscopic areas to bear loads of engineering significance.

The preceding features address the requirement for strength. Equally interesting is the ability of the gecko to detach with minimal force [52], ultimately facillitating high speed climbing. This can also be attributed to the fibrillar microstructure. Based on the observation of in-plane displacement during attachment, and normal displacment via digital hyperextention during detachment [29], it was proposed that the fibrillar adhesive system exhibits load-orientation depedent strength. It was revealed that this is a feature of the anisotropic geometry of the seta [48, 50], with loading angles $< 30°$ yielding highest strength. Consequently, the gecko may use in-plane loading of the adhesive system to modulate the setal loading angle, and the normal force which can be sustained without peeling. When climbing on walls frictional loading is a natural consequence of gravity, while on ceilings it is achieved by oppositely orienting the feet of the fore and hind limbs and loading via muscular contraction [53].

There have been considerable efforts to build upon the preceding knowledge to fabricate synthetic surface microstructures for dry adhesion. These can be primarily categorized as

passive, based upon normal contact at tips of vertical axisymmetric fibrils (e.g. [8-15]), or active, based upon shear-actuated side contact of geometrically anisotropic fibrils (e.g. [16-19]). Notable exceptions to these categorizations include angled tip-contact structures [20], defect-induced anisotropic tip-contact structures [21], film-terminated fibrillar structures [22], and fabric-elastomer composite adhesives without surface microstructure [23].

Axisymmetric tip-contact fibrils are typically designed to bear load normal to the interface, with their primary advantage being the simplicity of the macroscopic loading configuration. This is in contrast to shear-actuated side contact fibrils which, to bear load in the normal direction, require more complex configurations with oppositely oriented patches and mechanisms which maintain in-plane forces during load bearing (e.g. [54, 55]). These active systems do, however, have a tremendous advantage with respect ease of detachment. As in the biological system of the gecko, in-plane forces can be relaxed leading to low-force peeling. Alternative approaches have been devised for easy release of normal tip-contact fibrils, most notably fibril buckling [56-58].

Figure 1.3 shows several synthetic fibrillar microstructures, exemplifying both tip-contact [10, 11] and side-contact [16, 18] designs. As has proved most successful, these are all fabricated by replica molding. A curable polymer is cast in microfabricated master template, the features of which are typically defined by photolithography and etching. Using such processes, the minimum characteristic dimensions of individual structures have typically been limited to $1-10$ μm.

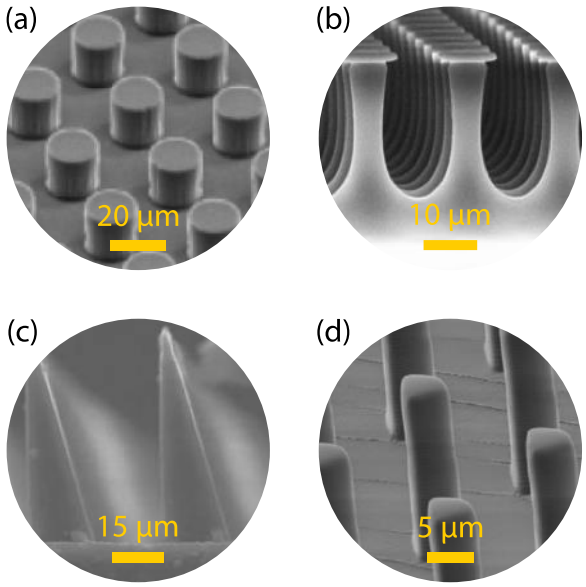

Figure 1.3. Examples of surface microstructures for synthetic dry adhesives; (a) Flat-ended cylindrical ('punch-like') fibrils, fabricated in polydimethylsiloxane (PDMS) via replica molding from a lithographically defined negative mold [10], (b) Mushroom-tipped fibrils fabricated in polyurethane (PU) using a lithography-based positive-negative-positive replica molding process [11], (c) Wedge-shaped microstructures fabricated in PDMS via replica molding from a lithographically defined negative mold [16], (d) Half-cylinder microstructures fabricated in PDMS via replica molding from a lithographically defined negative mold [18]. Reproduced with permission.

In accordance with the scope of this work, attention is limited to tip-contact fibrils from this point forward. The first performance metric of interest is adhesive strength of individual fibrillar sub-contacts. In this regard, perhaps the most fundamental principle raised by study of the gecko adhesive system was uniformity of the stress distribution at the interface of the substrate and nanometer scale spatulae, and the associated insensitivity to defects and the contact edge. Synthetic fibrils at the micron scale do not appear to be operating in this regime.

This has been directly evidenced by observation of defect propagation at the interface of the fibril tip and substrate (e.g. [59-62]). It is also implied by the dependence of the performance to changes in the tip geometry. Flange-tipped 'mushroom' fibrils, for example, have shown a 20-fold increase in detachment force over otherwise-identical punch-like counterparts [10]. This is now known to be associated with a reduction in the severity of the stress concentration at the contact edge [63, 64]. A significant emphasis has therefore been placed on the design of tip structures for improvement of the interfacial stress distribution. In addition to mushroom tips, notable examples include soft-tip layer composite fibrils [12-14], and 'funnel-shaped' microstructures [15].

Of equal importance, and having received significantly less attention, is the performance of synthetic dry adhesives at larger length scales. This encompasses arrays of fibrils, and must consider their backing structure and macroscale loading configuration. Often these lead to non-uniform load distributions among fibrils, which can become more severe as array size is increased. Scaling up the size of adhesive patches is necessary if problems of engineering significance are to be addressed. It is therefore vital that fibril design efforts be accompanied by approaches to improve the load distribution among fibrils. Hierarchy in the form of multi-level fibrillar structure has been explored as means to achieve this (e.g. [65, 66]). Adhesion enhancement has been inconsistent, owing to the complexity of fabrication [67]. Alternative approaches which avoid the requirement for fibrillar subdivision and which are commensurate with fabrication capabilities must therefore be explored.

In addition to performance in application, the load distribution across the array is of fundamental importance to the experimental characterization of fibrils. The measure of fibril adhesive strength (e.g. local detachment force), or strength per unit area of fibrillar interface (e.g. maximum stress or work of adhesion) will invariably be dependent on the local surface roughness and intrinsic material properties of the contacting surface. However, it is important that it be independent of the global properties of the measurement system in order to allow for comparison across experimental investigations. The geometry of the probe [68], control of alignment of probe and sample [69], and the compliance of the backing layer [70] can all give rise to non-uniform load distributions. Regardless of their source, these render the reporting of adhesion strength as the detachment force normalized by the projected contact area meaningless outside of the context of that specific study. Consequently, data suitable for comparison across experimental studies has been limited, either to investigations utilizing a well-aligned flat probe and backing layer which is sufficiently thin, or to a geometry which, although yielding a non-uniform load distribution, follows a well characterized adhesion or fracture mechanics model from which an intrinsic property of the fibrillar interface and contacting surface can be extracted.

Furthermore, an intrinsic measure of fibril strength is not the only physically relevant parameter which an ideal experiment should be able to capture. Variation in the size and character of the major flaw from fibril to fibril within the array will result in a corresponding distribution of fibril strength [45]. A measure of variability in strength, representative of this distribution, would provide a richer experimental characterization. The downside of traditional adhesion tests is that the standard deviation on the mean strength from repeated measurements

does not have direct physical relevance. Understanding the statistical properties of fibril adhesive strength may help to understand the role of roughness at the fibril tip, contaminant particles, and fabrication imperfections. Variability in fibril adhesive strength may also influence the performance in application, altering or precluding the role of other effects at large length scales such as backing layer compliance, substrate geometry, or large-scale roughness.

1.2 Outline

The broad goal of this work is to address the preceding challenges, furthering understanding of how the performance of individual, tip-contact fibrillar microstructures is coupled to larger length scale features of the contact. Two primary effects are studied. The first is the load distribution among fibrils, and its dependence on the geometry of the loading condition and the elastic properties of the backing layer. The second is the statistical variation in the strength of individual fibrils. In each case we focus on how the adhesive performance is impacted, and consider the relevance of this to both laboratory experimental characterization and system-level application.

Chapter 2 is a summary of the background information necessary to understand the details of the work described in subsequent chapters. It begins with a description of intermolecular forces, and their underlying strength. The theories of elasticity and linear elastic fracture mechanics are then described, with a view to understanding the reduction in strength associated with defect-controlled detachment. We finish by reviewing efforts to apply these theories to understand the performance of fibrillar adhesives, both at the single fibril level and at the fibril-array-scale.

Chapter 3 describes a theoretical parametric exploration of the performance of fibrillar arrays subject to non-ideal loading in the form of misalignment between adhesive surface and substrate. The work of Chapter 4 seeks to verify experimentally, hypotheses formed in Chapter 3 regarding the influence of backing layer compliance on the performance of an adhesive subject to misalignment.

Chapter 5 introduces the study of variability in fibril adhesive strength using the statistical theory of fracture. An experimental methodology is developed to verify the appropriateness of the theory, and to explore the significance of the statistical parameters it yields. Chapter 6 seeks to combine the fibril adhesive strength distribution characterized in Chapter 5 with the model of fibril load distribution utilized in preceding chapters, examining the coupling of these effects.

Chapter 2

Background

2.1 Intermolecular and surface forces

The general question to which we seek an answer is, for two bodies in contact, what it is the critical level of load required to cause absolute separation? The first step in the formulation of this problem is to examine the properties of the intermolecular interactions between bodies, determining the forces to which these give rise as a function of separation at the interface.

Interactions which play a role in adhesion can be extremely diverse [71]. Their origins can be electrostatic, entropic, and quantum mechanical by nature. In a given system they can be rate-dependent, non-additive, and influenced by the surrounding solvent media. In line with the goal of achieving temporary bonding, independent of surface chemistry, we limit our attention to the van der Waals interaction. This interaction is made up of electrostatic dipole-dipole (Keesom) and dipole-induced dipole (Debye) contributions, as well as the quantum mechanical dispersion (London) contribution. The latter is associated with instantaneous dipoles formed by electron and nucleus, which in turn induce dipoles in surrounding molecules and yield an attractive interaction. This charge fluctuation exists even in non-polar molecules, rendering the interaction universal.

The van der Waals pair potential for two dissimilar molecules in vacuum, assuming a single orbital frequency, ν, [72] is given by

$$w_{\mathrm{vdW}}(r) = -\left[({u_1}^2\alpha_2 + {u_2}^2\alpha_1) + \frac{{u_1}^2{u_2}^2}{3kT} + \frac{3\alpha_1\alpha_2 h\nu_1\nu_2}{2(\nu_1+\nu_2)}\right]\frac{1}{(4\pi\varepsilon_0)^2 r^6} = -\frac{C_{\mathrm{vdW}}}{r^6} \quad (2.1)$$

where w_{vdW} is the potential energy change is associated with bringing molecules to a separation r, from a reference state at $r = \infty$. The molecules each possess a permanent dipole moment, u, and an electronic polarizability, α. The Planck constant is h, the Boltzmann constant is k, the temperature is T, and the permittivity of free space is ε_0. Noting the tendency of atoms and molecules to adopt the configuration which minimizes their potential energy, we observe that the interaction is attractive.

Steric repulsion, associated with the overlapping of electron clouds, can be modelled with a so called hard-wall potential which becomes infinite at an assumed contact separation, r_0. Alternatively utilizing an inverse 12$^{\mathrm{th}}$-power law we obtain the ubiquitous Leonard-Jones potential

$$w_{\mathrm{LJ}}(r) = -\frac{C_{\mathrm{vdW}}}{r^6} + \frac{C_{\mathrm{steric}}}{r^{12}} \quad (2.2)$$

Molecular interaction potentials of the form given in (2.2) can be utilized in the derivation of energy and force laws for macroscopic bodies by summation over all molecules. The normal

force per unit area for the interface of two infinite surfaces (i.e. formed by two half-spaces) separated by distance z, is referred to here as the normal traction-separation law (where traction is in general the force per unit area acting at a material point on a surface) and was first derived by de Boer [73], as

$$\sigma(z) = \frac{A_{\mathrm{H}}}{6\pi {z_0}^3}\left[\left(\frac{z_0}{z}\right)^3 - \left(\frac{z_0}{z}\right)^9\right] \tag{2.3}$$

where z_0 is the equilibrium separation. We identify the material-dependent Hamaker constant [74] as $A_{\mathrm{H}} = \pi^2 C_{\mathrm{vdW}} \rho_1 \rho_2$, where ρ_1 and ρ_2 are the densities of the interacting bodies. Hamaker constants for interactions occurring in vacuum or air do not depend significantly on the media of the interacting bodies and are typically on the order of 10^{-19} J.

This result can be utilized to clarify several important energy and force definitions. The thermodynamic work of adhesion, W, is the energy per unit area associated with normal separation. It is the depth of the potential well at contact, and can be obtained from (2.3) according to

$$W = \int_{z_0}^{\infty} \sigma(z) dz = \frac{A_{\mathrm{H}}}{16\pi {z_0}^2} \tag{2.4}$$

We note that the surface energy is the free energy change associated with the creation of a unit area of free surface. This is half of the thermodynamic work of adhesion of two similar media in vacuum forming a perfect lattice. The maximum adhesive traction which can be supported

by the interface is termed the intrinsic strength, σ_0. Determining the maxima from (2.3), and combining with (2.4) we obtain

$$\sigma_0 = \frac{16}{9\sqrt{3}}\frac{W}{z_0} \tag{2.5}$$

Assuming that the contact separation is on the order of $0.1 - 1$ nm, the work of adhesion is on the order of $1 - 100$ mJ. Adopting a value of 10 mJ, the intrinsic strength of the van der Waals interaction in is on the order of $10 - 100$ MPa.

Using a force law of the form C_{vdW}/r^n, Bradley [75] demonstrated by integration that the maximum adhesive force between rigid spheres could be stated in terms of the work of adhesion as

$$F_{\max} = 2\pi RW \tag{2.6}$$

where the effective radius $R = R_1R_2/(R_1 + R_2)$. Notably, this result is independent of the power n, and thus the functional form of the force law. The same result was later reached by Derjaguin [76] using a geometric approach in which the force between two bodies with curved geometries is obtained by superposition of infinitesimal flat surface-surface interactions.

2.2 Theory of elasticity

While (2.5) and (2.6) represent important results for the interaction of rigid bodies, elastic deformation of bodies in contact can significantly influence the adhesive strength of a contact. With this noted we briefly review the central concepts of the theory of elasticity and linear elastic fracture mechanics, before exploring specific applications of these theories to relevant problems in contact and adhesion.

The goal of continuum mechanics is to analyze the distribution of internal stress and the deformation of a solid body which result from a combination of known displacements and tractions on its boundary. Such an analysis relies on three core concepts. The first is the conservation of linear momentum or an equivalent statement such as the principle of virtual work. Neglecting inertial effects, the former can be stated as

$$\underline{\nabla} \cdot \underline{\sigma} + \underline{b} = 0 \tag{2.7}$$

where $\underline{\nabla}$ is the gradient operator, $\underline{\sigma}$ is the Cauchy stress tensor, and $\underline{b}$ the body force (per unit volume). The stress tensor can be used to obtain the traction (force per unit area) on any plane with normal, $\underline{n}$, via Cauchy's law, as

$$\underline{T} = \underline{n} \cdot \underline{\sigma} \tag{2.8}$$

The second requirement is a set of kinematic relationships which relate displacement, $\underline{u}$, to a relevant measure of deformation. The infinitesimal strain tensor is given by

$$\underline{\varepsilon} = \frac{1}{2}\left[\underline{\nabla}\,\underline{u} + \left(\underline{\nabla}\,\underline{u}\right)^{\mathrm{T}}\right] \tag{2.9}$$

In three dimensions it describes deformation at a point encompassed by the stretching and relative rotation of three mutually orthogonal line elements.

The third and final statement encompasses the constitutive behavior of the material. We restrict our attention to linear infinitesimal strain elasticity, for which

$$\sigma_{ij} = C_{ijkl}\varepsilon_{kl} \tag{2.10}$$

where C_{ijkl} are the components of the elasticity tensor, which in general contains 21 independent material constants. For isotropic materials the number of independent constants reduces to 2, and the constitutive law can be stated in the concise form

$$\sigma_{ij} = \frac{E}{1+\nu}\left(\varepsilon_{ij} + \frac{\nu}{1-2\nu}\delta_{ij}\varepsilon_{kk}\right) \tag{2.11}$$

where E is Young's modulus and ν is Poisson's ratio. The elastic strain energy stored in the deformed configuration of the body is given by

$$\Pi_{\mathrm{el}} = \frac{1}{2}\int_V \varepsilon_{ij}\, C_{ijkl}\varepsilon_{kl}\, dV \tag{2.12}$$

where V is the volume of the body.

Eq. (2.7), (2.9), and (2.11) combine to yield 2nd order linear partial differential equations governing elastostatics. Typically, analytical solutions to these equations are only available for problems of reduced dimensionality. Stress function methods can be utilized in the solution of problems in which bodies are subject to traction boundary conditions only. Solutions which satisfy the boundary conditions of many interesting problems are available, including in contact and adhesion. Where these are not available, numerical methods such as finite element analysis are ubiquitous.

2.3 Linear elastic fracture mechanics

Defects or cracks in components are known to cause severe concentration of elastic stresses at their apex or tip. As the applied load is increased, bond rupture may occur in this region, thus extending the crack. If this extension increases the severity of the stress concentration then the crack will propagate in an unstable manner, leading to ultimate failure of the component. This is known as flaw-sensitive or defect-controlled failure. Since only a small region supports elevated stresses associated with bond rupture at any instant, the external load at which failure occurs is significantly reduced as compared to a defect free system in which the nominal stress in the entire body could be raised to the level of the bond strength.

The field of fracture mechanics was developed to study failure in brittle materials, but its concepts have proven extremely useful in the study of adhesion. Regions of the interface where the separation of surfaces exceeds the range of the interaction concentrate elastic stresses in a

similar manner to cracks in bulk materials. The general approach is to assume that failure occurs when a parameter encompassing defect geometry, component geometry, elastic properties and external applied loading, reaches a critical value which is a measure of the resistance of the bulk material or interface to defect propagation.

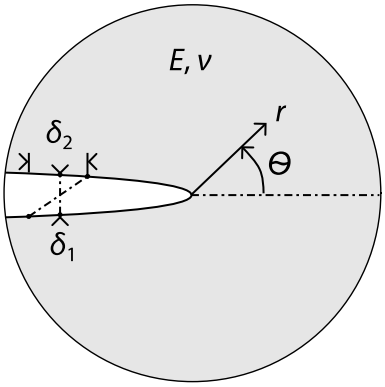

Figure 2.1. Schematic of crack in an isotropic linear elastic body, showing the polar coordinate system, (r, θ), used in the formulation of linear elastic fracture mechanics. Crack opening displacements, δ_1 and δ_2, are also shown.

Figure 2.1 shows a crack in an isotropic linear elastic body. Griffith theory [77] considers the energetics of crack growth, noting that crack advance must be accompanied by strain energy release as the crack surface is necessarily traction free, and that the strain energy released must account for the energy of the newly created crack surface. This was formalized by Irwin [78] who defined the energy release rate as

$$G = -\frac{\partial \Pi}{\partial A} \tag{2.13}$$

where Π is the total mechanical potential energy (elastic strain energy and potential of the applied loads) and A is the crack area. By solution of the elasticity problem for the cracked component, the energy release rate can be obtained in terms of crack geometry, component geometry, the elastic properties, and the applied load. It is assumed that defect propagation occurs when the energy release rate exceeds a critical value termed the toughness, G_c. Griffith's assumption that the toughness $G_c = 2\gamma$ is violated in all but highly brittle solids due to the contribution of dissipative effects, as is discussed below.

The insight gained from the preceding theory made be somewhat surprising given that it does not rely on the fundamental observation that fracture proceeds as and when the stress ahead of a crack tip is raised significantly enough to cause bond rupture. The asymptotic elastic crack-tip stress fields have the form [79]

$$\sigma_{ij}(r,\theta) = \frac{K_{\mathrm{I}}}{\sqrt{2\pi r}} f_{ij}{}^{\mathrm{I}}(\theta) + \frac{K_{\mathrm{II}}}{\sqrt{2\pi r}} f_{ij}{}^{\mathrm{II}}(\theta) \tag{2.14}$$

where the polar coordinate system, (r,θ), is shown in Figure 2.1. The angular dependence is encompassed by the functions $f_{ij}{}^{\mathrm{I}}$ and $f_{ij}{}^{\mathrm{II}}$. An inverse square root singularity at the crack tip is observed, the strength of which is controlled by the coefficients K_{I} and K_{II}. These are termed the stress intensity factors. The crack opening displacements are given by

$$\delta_1 = \frac{8K_{\mathrm{I}}}{E'}\sqrt{\frac{r}{2\pi}}$$
$$\delta_2 = \frac{8K_{\mathrm{II}}}{E'}\sqrt{\frac{r}{2\pi}} \tag{2.15}$$

where the modulus $E' = E$ for plane stress $E' = E/(1-\nu^2)$ for plane strain. The displacement δ_1 is the normal separation of the crack faces, while the displacement δ_2 is the sliding of one face relative to the other. These are shown in Figure 2.1.

The angular dependencies of ${f_{ij}}^{\mathrm{I}}$ and ${f_{ij}}^{\mathrm{II}}$ are such that K_{I} and K_{II} independently control normal stress, $\sigma_{\theta\theta}$, and shear stress, $\sigma_{r\theta}$, ahead of the crack tip, respectively. The *mode mixity* is characterised by the ratio of sliding and opening of the crack face, or by the ratio of shear and normal stresses ahead of the crack tip, via the phase angle

$$\psi = \tan^{-1}\left(\frac{\sigma_{r\theta}(r,0)}{\sigma_{\theta\theta}(r,0)}\right) \tag{2.16}$$

In isotropic materials the ratio $\sigma_{r\theta}/\sigma_{\theta\theta}$ is independent of the distance from the crack tip. Furthermore, the normal and shear stresses are independently controlled by the stress intensity factors K_{I} and K_{II}, respectively. This allows (2.16) to be rewritten as

$$\psi = \tan^{-1}\left(\frac{K_{\mathrm{II}}}{K_{\mathrm{I}}}\right) \tag{2.17}$$

Just as for the energy release rate, the stress intensity factors are determined by solution of the elasticity problem, and are functions of the crack geometry, the component geometry, and the applied load. Failure is once again assumed to occur when the stress intensity factor reaches a material dependent critical value, K_c, also termed the toughness. The equivalence of energy release rate and stress intensity factor approaches was demonstrated by Irwin [80] through consideration of the work done by the crack tip stresses in moving through the opening displacements during crack extension, leading to

$$G = \frac{{K_{\mathrm{I}}}^2}{E'} + \frac{{K_{\mathrm{II}}}^2}{E'} \tag{2.18}$$

In applying fracture mechanics concepts to the study of adhesion we are concerned with a crack plane at the interface of two bodies with differing mechanical properties. Interfacial fracture mechanics is considerably more involved as mode mixity is dependent on the elastic mismatch across the interface, and the toughness of the interface is typically a function of the mode mixity. For a concise review of these concepts, readers are referred to ref. [81]. Fortunately, much of the complications of interfacial fracture mechanics are avoided in this work as we are primarily concerned with the contact of elastomeric materials and much stiffer substrates. The Dundurs parameters [82], which describe fully describe the elastic mismatch at the interface for plane problems, are

$$\alpha_{\mathrm{D}} = \frac{E_1' - E_2'}{E_1' + E_2'}$$
$$\beta_{\mathrm{D}} = \frac{G_1(\kappa_2 - 1) - G_2(\kappa_1 - 1)}{G_1(\kappa_2 - 1) + G_2(\kappa_1 - 1)} \tag{2.19}$$

where the shear modulus $G = E/[2(1+\nu)]$, $\kappa = 1 + \nu$ for plane stress and $\kappa = 3 - 4\nu$ for plane strain. For a set of incompressible materials, where one material is considerably stiffer than the other, the Dundurs parameters are $\alpha = \pm 1$ and $\beta = 0$. In this case the bimaterial asymptotic crack tip stress fields [83] simplify to the form presented in (2.14). We note that both the opening displacements of (2.15) and the Irwin relationship of (2.18) must be modified by a factor of ½, accounting for the fact that opening only occurs on the compliant side of the interface.

In applying the concepts of fracture mechanics to the study of adhesion, the interfacial toughness is equivalent to the work of adhesion, $G_{\mathrm{c}} = W$. The critical value of the mode I stress intensity factor is, via (2.18) when modified by a factor of ½, $K_{\mathrm{c}} = \sqrt{2E'W}$. Adopting the thermodynamic work of adhesion of Section 2.1 as the failure criterion is analogous to the surface energy hypothesis of Griffith. In most material systems, non-linear and dissipative processes at the crack tip may increase the energy requirement for separation. Given this observation, it is worth considering the validity of a failure criterion based on linear elasticity.

The preceding framework is based upon the assumption that the region close to the crack tip where rupture occurs, termed the 'fracture process zone', is embedded within a stress field which is accurately represented by (2.14). For this to hold, the dimensions of the fracture

process zone must be much smaller than that of the component or adhesive contact. In this case the asymptotic elastic crack tip stress fields effectively control the details of failure inside the fracture process zone. All of these details, including dissipative contributions not associated with bond rupture, will therefore be captured when the toughness or work of adhesion is determined by experiment. In general the toughness or work of adhesion can include dissipative contributions from any microstructural features with shorter characteristic length scales than are included the formulation of the elasticity problem. In this way the same fundamental elasticity solution can, for example, be utilized to examine the adhesion of a single asperity achieving molecular contact with a surface and interacting via van der Waals forces, or to model the adhesion of a macroscale probe with a microstructured surface. In the former case, the work of adhesion would be the thermodynamic property identified in Section 2.1, while in the latter case it would be a property of the microstructure and the interface formed with the substrate.

The validity of the assumption of a small-scale fracture process zone must be assessed by estimating its size. Estimating the extent of the region over which the elastic stresses at the crack tip exceed the intrinsic strength, a characteristic length scale emerges

$$c = \frac{E'W}{{\sigma_0}^2} \tag{2.20}$$

When the geometric features of the contact are on the order of c, failure is termed flaw-insensitive. Separation no longer occurs via nucleation and propagation of defects. The entirety of the interface supports the maximum stress permitted by the microscale mechanics,

maximizing the load bearing capability of the joint. This is typically the optimal condition when designing for adhesive strength.

Dugdale presented an alternative framework [84] which correctly predicts the asymptotic limits and transition between flaw-sensitivity (as predicted by LEFM) and flaw-insensitivity. The approach was first applied in the context of adhesion by Maugis [85]. It is based upon a simplified form of the traction separation law (being uniform up to a cut-off separation), which has been shown to lead to negligible error in the predicted condition for failure provided that the work of adhesion, W, and the theoretical strength, σ_0, are consistent [86].

2.4 Models of adhesion

Figure 2.2 shows three geometric configurations of relevance to the work at hand. In each case a compliant body of Young's modulus E, and Poisson's ratio ν, contacts a much stiffer substrate which is considered as rigid. The strength of the interface is characterized by the work of adhesion, W.

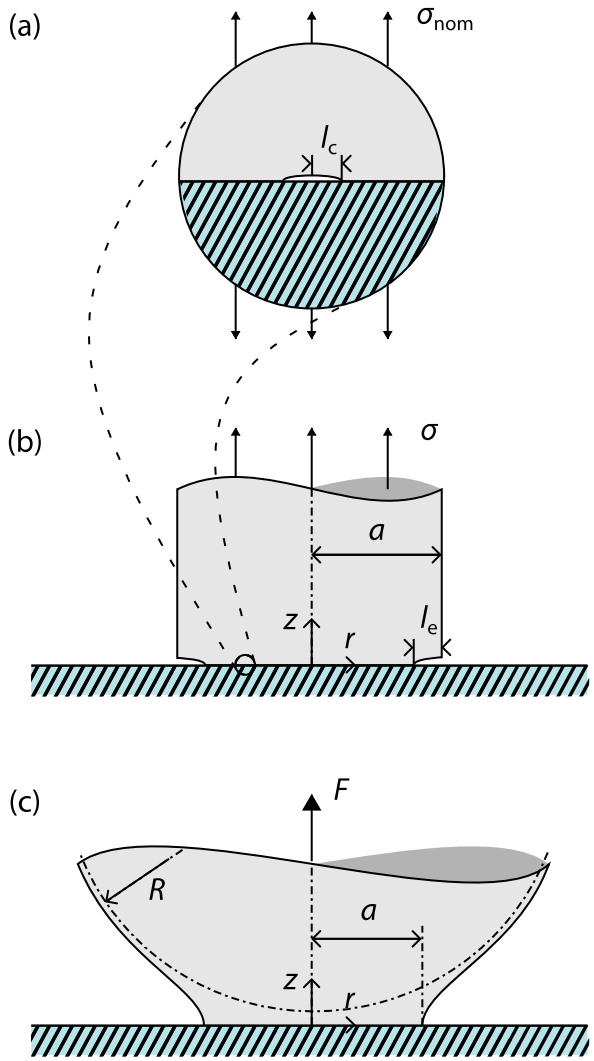

Figure 2.2. Schematic of three adhesive contact geometries of relevance to the current work: (a) A penny-shaped defect of radius l_c, located at the interface of a compliant body and a rigid substrate, far from any geometric features. The region of the interface in which it is located experiences nominal tensile stress, σ_{nom}; (b) A compliant cylindrical body of radius a, contacting a rigid substrate over its flat end. The body is subjected to remote tensile stress, σ. A circumferential defect, protruding in to the contact by length l_e is also considered; (c) A compliant body of uniform radius of curvature, R, contacting a rigid substrate. The circular contact which forms has radius a. The body is subject to a remote tensile load, F.

2.4.1 General interfacial defect

Figure 2.2a depicts a geometry in which the strength is controlled by a circular defect at the interface, far from any geometric features of the bodies. The radius of the defect is l_c. The interface experiences a nominal tensile stress, σ_{nom}, which is a function of the applied load and the geometry of the body but is independent of the defect geometry in the limit described. In general it is known that the nominal stress is linearly related to the remote applied tensile stress, σ, such that it can be written that $\sigma_{nom} = A\sigma$, where A is a geometry-dependent dimensionless 'shape factor'. It is assumed that the nominal shear stress at the interface is negligible.

This is a special case of one of the most fundamental problems of interfacial fracture mechanics [87]. As discussed in Section 2.3, we limit our attention to an incompressible compliant body contacting a rigid substrate. In this case the crack tip stress fields are equivalent to those in a homogeneous body and the stress intensity factors

$$K_I = B_I \sigma \sqrt{\pi l_c}$$
$$K_{II} = 0 \qquad (2.21)$$

where the shape factor $B_I = 2A/\pi$. The critical level of remote applied stress is therefore given by the criterion $K_I = K_c = \sqrt{2E^* W}$ and is

$$\sigma_{\max} = \frac{\pi}{2A}\left(\frac{2E^{*}W}{\pi l_{c}}\right)^{\frac{1}{2}} \tag{2.22}$$

If mathematically tractable, solution of the elasticity problem will yield the shape factor A (and therefore also B_{I}) in terms of the relevant geometric parameters of the system.

There are many cases of interest where the defect is located close to a geometric feature which is itself a stress raiser, in which case the shape factor is no longer independent of the crack geometry. In many cases the region of interest is the contact edge, which can give rise to singular stress fields independent of those at the tip of an interfacial defect in this region.

2.4.2 Contact edge of ideally flat interface

Figure 2.2b shows the first case of interest in which the contact edge is the critical stress raiser. It involves an abrupt contact edge, with a curvature much smaller than the contact dimensions, leading to the idealization of the geometry as a cylindrical elastic body of radius a, contacting a rigid substrate over its flat end. The presence of a circumferential defect protruding in to the contact by length l_{e} is considered in specific analyses.

While not exactly the problem at hand, it is worth first considering the opposite case of elastic mismatch i.e. where a rigid cylindrical body contacts an elastic half space. This problem permits a relatively straightforward solution and reveals qualitative trends which hold for the case of primary interest. This problem was addressed by Kendall [88] under assumption of a frictionless interface (and later shown to be valid for incompressible bodies independent of the

assumed friction condition [89]). The elasticity solutions utilized are derived via the potential functions of Boussinesq and Cerruti, as presented in ref. [90]. The displacement of the elastic half space must be uniform and equal to the remote applied displacement. The normal traction at the interface which satisfies this condition is

$$\sigma_{zz}(r) = \frac{1}{2}\sigma\left[1 - \left(\frac{r}{a}\right)^2\right]^{-1/2} \tag{2.23}$$

where r is the radial coordinate defined from the center of the contact. Performing a series expansion with respect to the distance from the contact edge, it is determined that the tensile stress in this region exhibits an inverse square root singularity. This renders the contact edge equivalent to the tip of an external circumferential crack, with the mode I stress intensity factor

$$K_{\mathrm{I}} = \frac{1}{2}\sigma\sqrt{\pi a} \tag{2.24}$$

The critical value of the applied load at which separation begins at the contact edge is given by the condition $K_{\mathrm{I}} = K_{\mathrm{c}} = \sqrt{2E^*W}$, leading to

$$\sigma_{\max} = \left(\frac{8E^*W}{\pi a}\right)^{1/2} \tag{2.25}$$

It is observed that the strength of the contact scales with the square-root of the work of adhesion, as well as the elastic modulus. The latter reflects the limitation of opening displacements, preventing absolute separation as the load is increased. It also scales with the

inverse-square-root of the contact radius, demonstrating that smaller contacts yield higher strength. The strength will saturate at the intrinsic level of the interaction as the validity of linear elastic fracture mechanics breaks down, when the contact radius is on the order of the fracture process zone size of (2.20).

When the cylindrical body is elastic and the substrate is rigid, the analysis is more involved. Under the same assumption that the interface is frictionless, the contact edge no longer concentrates stress. Under the assumption of full sticking (zero tangential displacement) the elastic stresses are singular at the contact edge, with the inverse power ~ 0.4 determined by Bogy [91]. We proceed considering this case, noting that it represents a lower bound on the strength of the contact with respect to the friction condition at the interface. Hui et al. [46] showed that for detachment is controlled by defect nucleation at the contact edge, the maximum remote tensile stress should scale as $(E^*W)^{0.4}{\sigma_{\text{th}}}^{0.2}/a^{0.4}$. It is observed that reduction in the strength of the contact with increasing contact radius is less severe than (2.25).

Khaderi et al. [89] have performed a more rigorous analysis of this contact problem for a full range of elastic mismatch. They first formalize the analysis of singular stresses at the contact edge (equivalent to that of Bogy [91]) for the study of fracture, introducing the concept of the 'H-field'. Two singular terms dominate at the contact edge, with the power-law dependence of each being dependent on the elastic mismatch through the Dundurs parameters of (2.19). Coefficients H_1 and H_2 control the singular terms in a manner analogous to K_{I}. Indeed, in the corresponding limit of elastic mismatch, the result of (2.24) can be obtained. For an

incompressible elastic cylinder on a rigid substrate, one singular term drops out and the asymptotic field as $r \to a$ is

$$\sigma_{zz}(\rho) = 0.386\sigma\left(\frac{a}{a-r}\right)^{0.4} \tag{2.26}$$

The presence of the circumferential defect at the contact edge is then considered. This defect introduces its own bimaterial singular stress field at its tip. As discussed in Section 2.3, for the case of the incompressible elastic cylinder on a rigid substrate avoids the complex nature of these fields is avoided. The stress intensity factors are

$$K_{\mathrm{I}} = B_{\mathrm{I}}\sigma\sqrt{\pi l_{\mathrm{e}}} \tag{2.27}$$

$$K_{\mathrm{II}} = B_{\mathrm{II}}\sigma\sqrt{\pi l_{\mathrm{e}}} \tag{2.28}$$

where the shape factors B_{I} and B_{II} are dependent on the ratio l_{e}/a. These are determined via finite element analysis using the domain integral method. The results are shown in Table 2.1 for a range of values of the ratio l_{e}/a. Their determination permits evaluation of the mode mixity, which is shown to be $< 20°$ in all cases. It is therefore reasonable to assume that separation is associated with the mode I work of adhesion, such that ${K_{\mathrm{I}}}^2 + {K_{\mathrm{II}}}^2 = 2E^*W$. The maximum remote tensile stress is therefore

$$\sigma_{\max} = \frac{1}{B}\left(\frac{2E^*W}{\pi l_{\mathrm{e}}}\right)^{\frac{1}{2}} \tag{2.29}$$

where $B = ({B_{\mathrm{I}}}^2 + {B_{\mathrm{II}}}^2)^{1/2}$. The maximum remote tensile stress can alternatively be stated in terms of the contact radius as

$$\sigma_{\max} = \frac{1}{C}\left(\frac{8E^{*}W}{\pi a}\right)^{1/2} \tag{2.30}$$

where the shape factor $C = 2B\sqrt{l_{\mathrm{e}}/a}$. The result is stated in a form which is directly comparable to the opposite case of elastic mismatch, given in (2.25). Values of the coefficients B_{I}, B_{II}, B and C are also listed in Table 2.1. The observation of monotonic increase of C as the ratio l_{e}/a increases indicates unstable defect propagation.

Defect size, l_e/a	Coefficient, B_I	Coefficient, B_{II}	Mode mixity, ψ	Coefficient, B	Coefficient, C
0.02	2.66	0.818	17.1°	2.78	0.786
0.10	1.51	0.487	17.8°	1.58	1.00
0.30	1.42	0.325	12.7°	1.45	1.58
0.50	1.92	0.218	6.4°	1.93	2.73
0.70	3.63	0.108	1.7°	3.63	6.07

Table 2.1. Table of coefficients for the problem of an incompressible elastic cylinder in contact with a rigid flat substrate ($\alpha = -1$ and $\beta = 0$), as reported in [89].

While the preceding results are instructive, the absence of an analytical solution for the dependence of the shape factors on the ratio l_e/a obfuscates the true scaling of the strength with these parameters. While this is not possible in the most general case, a result is reported by the authors in the limit that the defect is sufficiently small that it is embedded within the region of dominance of the edge singularity.

In this case, dimensional considerations yield the bimaterial stress intensity factors in terms of the H-field parameters. The coefficients are determined by the domain integral method in finite element analysis of the H-dominated region only. Once again for case of the incompressible elastic cylinder on a rigid substrate, the result is

$$K_{\mathrm{I}} = 0.537\left(\frac{a}{l_{\mathrm{e}}}\right)^{0.4}\sigma\sqrt{\pi l_{\mathrm{e}}} \tag{2.31}$$

$$K_{\mathrm{II}} = 0.165\left(\frac{a}{l_{\mathrm{e}}}\right)^{0.4}\sigma\sqrt{\pi l_{\mathrm{e}}} \tag{2.32}$$

The maximum remote tensile stress is therefore

$$\sigma_{\max} = \frac{1.42\sqrt{E^{*}W}}{{l_{\mathrm{e}}}^{0.1}a^{0.4}} \tag{2.33}$$

where we observe the same scaling with the contact radius as predicted by Hui et al. [46].

2.4.3 Contact edge of ideally curved interface

Figure 2.2c shows the final case of interest, which concerns the contact of an elastic body with a large radius of curvature, R. Contact with the rigid substrate occurs over a circular area of radius a. This is a special case of the more general problem of the adhesive contact of elastic spheres. This problem has received several theoretical treatments. We begin by considering the Johnson-Kendall-Roberts (JKR) theory [92]. This model is based on the assumption that the radii of curvature of the contacting bodies are much larger than the contact area itself, such that they can each be treated as an elastic half space. The Boussinesq-Cerruti family of elasticity solutions can once again be utilized. Unknown coefficients in the solution are determined on the basis of a free energy minimization (considering elastic strain energy and interfacial energy) which is equivalent to linear elastic fracture mechanics. It is assumed that the adhesive interaction occurs in the contact area only. The size of region in which high

normal stress causes separation of the bodies is small in comparison to the contact. This is exactly the assumption that the fracture process zone is small.

Before beginning it should be noted that for this configuration, the contact area changes continuously with the applied load. Without a clearly defined area with respect to which the remote applied load is normalized, the analysis is performed in terms of the load, F, itself. The condition on displacements of the bodies is based on avoiding interpenetration, and is therefore a known function of the radius of curvature. The surface displacement in the contact must be of the form

$$u_z(r) = \Delta + \frac{r^2}{2R} \tag{2.34}$$

where Δ is the remote applied displacement of the body, r is the radial coordinate defined from the center of the contact, and R is the radius of curvature. The normal traction at the interface which satisfies this condition is

$$\sigma_{zz}(r) = -\frac{2aE^*}{\pi R}\left[1-\left(\frac{r}{a}\right)^2\right]^{1/2} + \left(\frac{F}{2\pi a^2}+\frac{2aE^*}{3\pi R}\right)\left[1-\left(\frac{r}{a}\right)^2\right]^{-1/2} \tag{2.35}$$

where a is the contact radius, the modulus $E^* = E/(1-\nu^2)$, and the relationship between load and displacement is

$$F = \frac{2}{3}\pi a^2 \left(\frac{aE^*}{\pi R} + \frac{3E^*\Delta}{\pi a}\right) \tag{2.36}$$

Performing a series expansion with respect to the distance from the contact edge, it is confirmed that an inverse square-root singularity dominates close to the contact edge. The strength of the singularity is uniquely controlled by the coefficient on the second term of (2.35), with the stress intensity being

$$K_{\mathrm{I}} = \left(\frac{F}{2\pi a^2} + \frac{2aE^*}{3\pi R}\right)\sqrt{\pi a} \tag{2.37}$$

This configuration differs from a traditional fracture problem in that effective crack geometry, which is described by the contact radius, evolves continuously as the external load changes. For this reason, the stress intensity must always be at the critical level $K_{\mathrm{I}} = K_{\mathrm{c}} = \sqrt{2E^*W}$. Combining this condition with (2.37) allows for the determination of the contact radius as a function of the applied load

$$a^3 = \frac{3R}{4E^*}\left[-F + 3\pi RW \pm (-6\pi RWF + (3\pi RW)^2)^{1/2}\right] \tag{2.38}$$

Knowing that the crack propagation is continuous, determining the critical value of the applied load requires analysis of the stability, $\partial K_{\mathrm{I}}/\partial a = 0$. In load control the point of instability coincides with maximum tensile load

$$F_{\max} = \frac{3}{2}\pi RW \tag{2.39}$$

while in displacement control the contact remains stable as the load is reduced to $\frac{5}{6}\pi RW$.

Derjaguin-Muller-Toporov (DMT) theory [93] considers the adhesive contact of elastic spheres in an alternate manner. It is assumed that the deformed geometry of the contact follows Hertz theory [94], with the distribution of interfacial stress being compressive. The net force associated with the repulsive pressure in the contact region is supplemented by the net attractive force from regions outside of the contact. As the contact area is reduced the repulsive contribution to the total force is reduced. When the contact area is zero the entire body contributes to the attractive interaction. At this point the configuration is exactly equivalent to the Derjaguin result for undeformable bodies. The maximum adhesive force is given by

$$F_{\max} = 2\pi RW \tag{2.40}$$

The difference in the adhesion force predictions of JKR and DMT theories was first addressed by Tabor [95], who noted that the when the contact edge opening displacement or 'neck height' predicted by JKR theory is on the order of the molecular contact separation then the distinction between contact and non-contact is lost. This opening is on the order

$$h = \left(\frac{RW^2}{E^2}\right)^{1/3} \tag{2.41}$$

Determining the validity of JKR theory therefore requires comparison of the magnitude of the elastic deformation to the range of the surface interaction. Tabor concluded that when $h/z_0 > 5$ JKR theory can be applied with validity while DMT theory provides good approximation when $h/z_0 < 0.1$. For intermediate values an alternative analysis has been proposed by Maugis [85], which correctly predicts the asymptotic behavior of JKR and DMT. We see that while the elastic properties do not explicitly influence the adhesion force in either theory, the validity of each result is determined by the elastic modulus and its magnitude in comparison to the work of adhesion. For an elastomeric body contacting a rigid substrate, in the presence of van der Waals forces, this predicts validity of JKR theory when the radius of curvature exceeds 10 nm.

2.4 Adhesive performance of synthetic fibrils

In Section 2.4.2, the study of the contact of a compliant flat-ended cylinder in contact with a rigid substrate revealed the damaging influence of the contact edge stress concentration. The severity of this stress concentration was shown to increase with the size of the contact. Consequently, when detachment is controlled by defect nucleation or propagation from the contact edge, the strength was shown to decay with the inverse-power 0.4 of the contact radius in (2.33).

The design strategy suggested through study of the fibrillar adhesive systems in climbing animals, is to reduce the size and increase the density of individual contact elements [44-48]. However, in the creation of synthetic fibrillar systems, the size of individual fibrils is limited by the constraints of fabrication techniques. Typical fibrils fabricated by molding of

elastomeric materials are, at their smallest, on the order of $1-10$ μm. Consequently, detachment occurs via the propagation of defects at the interface of the fibril tip and substrate (e.g. [59-62]). Associated with this is a strong dependence of the strength on the fibril tip geometry [10].

Given that the strength is sensitive to the tip geometry, it is unsurprising that there has been considerable focus on the design of the fibril tip to improve strength. This has primarily been associated with reducing the severity of the contact edge stress concentration.

Figure 2.3 shows two of the most prevalent designs. The first is the 'mushroom-tipped' fibril, shown in Figure 2.3a, the design origins of which also can be traced to biological systems [59]. The inclusion of a thin flange around the tip has the effect of reducing strain energy at the contact edge and creating a turning action which results in a compressive contribution to the stresses in this region [63, 64]. Ballejipali et al. [64] provided a detailed analysis equivalent to that performed for a 'punch-like' flat-ended cylinder by Khaderi et al. [89]. It was assume that a circumferential defect of length l_{e} was fully embedded within the singular field at the contact edge, such that the scaling of strength is equivalent to (2.33). As such, it can be written that

$$\frac{\sigma_{\max}^{\mathrm{m}}}{\sigma_{\max}^{\mathrm{p}}} = \kappa_{\mathrm{m}} \tag{2.42}$$

where $\sigma_{\max}^{\mathrm{m}}$ is the maximum remote stress for the mushroom-tipped fibril, $\sigma_{\max}^{\mathrm{p}}$ is the maximum remote stress for the punch-like fibril, and κ_{m} is a coefficient which is dependent on the geometric properties of the mushroom.

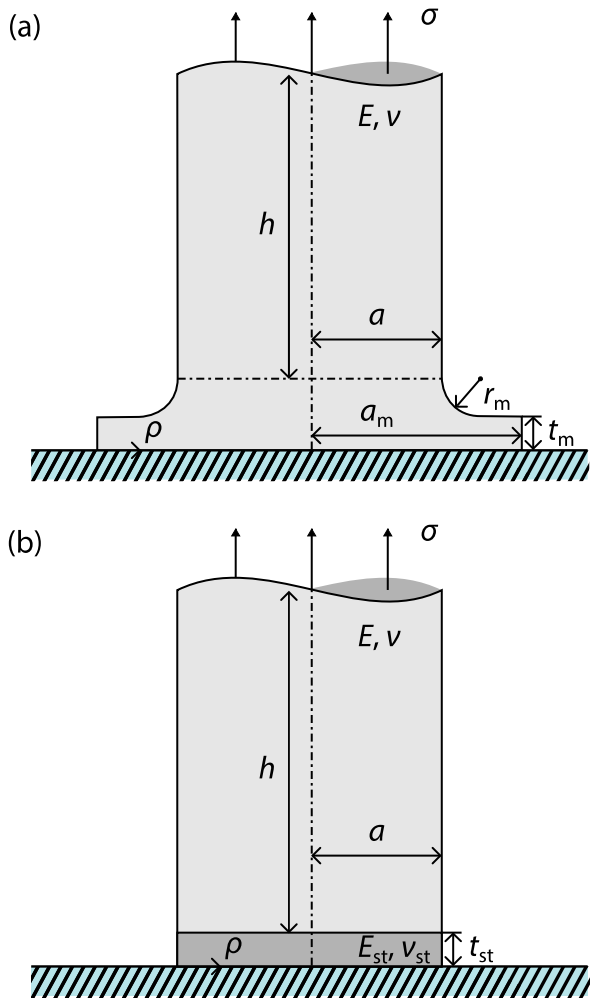

Figure 2.3. Schematic of synthetic fibril designs showing parameterization of the geometries; (a) 'Mushroom-tipped' fibril comprised of a cylindrical stalk with radius a and length h, and flange of radius a_{m} and thickness t_{m}. There is a filleted corner where the flange meets the stalk, with radius r_{m}; (b) 'Soft-tip-layer' fibril comprised of a cylindrical stalk with radius a and length h, and more compliant tip layer ($E \gg E_{\mathrm{st}}$) of thickness t_{st}.

Figure 2.4 shows the interfacial stress distribution under the assumption of full contact for two mushroom geometries, with and without a fillet at the joint of the flange and stalk, as well as

for the punch-like geometry. The results are shown on a log scale on account of the singularity at the contact edge.

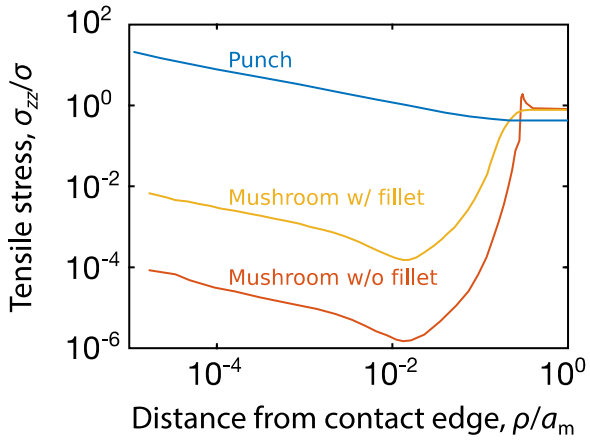

Figure 2.4. Tensile stress at the interface of fibril tip and substrate for three geometries - a flat-ended cylindrical fibril (blue); a mushroom-tipped fibril without a fillet at the intersection of flange and stalk, $r_m/a = 0$ (orange); a mushroom-tipped fibril with a fillet at the intersection of flange and stalk, $r_m/a = 0.23$ (yellow). For both mushroom fibrils the flange radius $a_m/a = 1.41$ and flange thickness $t_m/a_m = 0.016$. Reproduced under CC BY NC ND license from [64].

Table 2.2 provides the coefficient, κ_m, for various values of the flange radius a_m and the flange thickness, t_m, describing the enhancement of the adhesive strength associated with the mushroom-tip when controlled by defect propagation from the contact edge. It is observed that the strength increases as both the flange radius is increased, and as the flange thickness is reduced. The enhancement can be extreme when the flange is wide and thin, but this potential advantage must be weighed against the reduced structural stability of the tip. Additionally, where the contact edge stress concentration is sufficiently reduced, we observe in Figure 2.4

that the stresses are elevated at the contact center. In particular, stresses are highly concentrated under where the stalk meets the flange. The inclusion of a fillet, smoothing the transition between stalk and flange, reduces the severity of this stress concentration. Elevated stresses at the contact center may lead to the propagation of defects in this region. Typically the strength associated with center defect propagation of a mushroom-tipped fibril remains considerably higher than an edge defect propagation in a punch-like fibril, rendering the design beneficial to adhesive performance overall.

Flange radius ratio, a_{m}/a	Flange thickness ratio, $t_{\mathrm{m}}/a_{\mathrm{m}}$	Coefficient, κ_{m}
1.09	0.050	3.1
	0.084	1.8
	0.150	1.2
1.41	0.050	46.3
	0.084	8.4
	0.150	2.9
1.85	0.050	397.1
	0.084	27.8
	0.150	5.6

Table 2.2. Table of coefficients describing the ratio of maximum remote stress for mushroom-tipped and punch-like fibrils, $\kappa_{\mathrm{m}} = \sigma_{\mathrm{max}}^{\mathrm{m}}/\sigma_{\mathrm{max}}^{\mathrm{p}}$. Results are shown for a range of geometric parameters of the flange. Reported in [64].

Another design which has proved to reduce the severity of edge stress concentration is associated with the inclusion of a tip layer comprised of a more compliant material that the stalk of the fibril. The improvement in performance is associated with the following effect. The confinement of the layer on both sides leads to large shear stresses which resist Poisson contraction. Since these shear terms are of opposite sign on each side of the layer, there is a large gradient through its thickness. This must be balanced by the radial gradient in the radial stress, which builds up in the contact center. Since the stress state in the layer is hydrostatic to first order [96], the interfacial stress is also concentrated in this region and thus is reduced at the contact edge. Once again, Ballejipali et al. [96] performed a detailed analysis directly comparable to the punch-like fibril results of Khaderi et al. [89], leading to

$$\frac{\sigma_{\max}^{\mathrm{st}}}{\sigma_{\max}^{\mathrm{p}}} = \kappa_{\mathrm{st}} \tag{2.43}$$

where $\sigma_{\max}^{\mathrm{st}}$ is the maximum remote tensile stress for the soft-tip-layer fibril and κ_{st} is a shape factor which is dependent on the geometric properties of the soft-tip-layer.

Table 2.3 provides the coefficient, κ_{st} for various values tip-layer thickness t_{st} and the ratio of elastic modulii, E/E_{st}, describing the enhancement of the adhesive strength associated with the soft-tip-layer when controlled by defect propagation from the contact edge. Both materials are considered to be incompressible, $\nu = \nu_{\mathrm{st}} \cong 0.5$. It is observed that the strength is enhanced as both the layer thickness is reduced, and as the elastic modulus ratio is increased. The greater the reduction in the array edge stress concentration, the greater the stresses at the contact center.

There are, however, additional considerations when designing on the basis of these trends. Reducing the layer thickness to improve strength is likely to be limited by the increased potential for inhomogeneities in such a layer. Furthermore, finger crack instabilities have been observed in thin layers and have led to significantly reduced strength [96]. The elastic properties of the fibril are critical to performance at larger length scales, as will be discussed in the subsequent section. Changing the ratio E/E_{st} must also be considered this context.

Tip-layer thickness ratio, $t_{\mathrm{st}}/(h+t_{\mathrm{st}})$	Elastic modulus ratio, E/E_{st}	Coefficient, κ_{st}
0.05	2	1.27
	10	2.21
	100	3.93
	1000	4.41
0.15	2	1.11
	10	1.27
	100	1.33
	1000	1.36
0.25	2	1.03
	10	1.06
	100	1.08
	1000	1.08

Table 2.3. Table of coefficients describing the ratio of maximum remote stress for soft-tip-layer and punch-like fibrils, $\kappa_{\mathrm{st}} = \sigma_{\mathrm{max}}^{\mathrm{st}}/\sigma_{\mathrm{max}}^{\mathrm{p}}$. Results are shown for a range of geometric and material properties of the soft-tip-layer. Reported in [96].

The preceding results must be contextualized based on the properties of surface roughness of the fibril tip and substrate. The tip geometry will only control fibril strength where this roughness exists on length scales much smaller than the fibril itself (e.g. when the characteristic length scales of roughness do not exceed tens of nanometers for micron scale fibrils, corresponding to a surface considered to be 'smooth' in a qualitative sense). In this case the resulting defects will be imbedded within, and will nucleate from, the region where interfacial stresses are highest [59-62]. If roughness exists at larger length scales then it may disrupt the dominance of the tip geometry and the strength enhancement associated with refined design. In this case there is the potential for partial loss of contact, and for defect propagation from any region at the tip-substrate interface. Roughness on this scale of the fibrils themselves has, in general, been associated with a reduction in the adhesive strength [97-99].

2.5 Adhesive performance of fibril arrays

While the properties of the fibril tip play an important role in determining the strength of individual sub-contacts, there are other aspects of fibril design which influence performance at larger length scales. Features of the system at these scales also play a role in determining strength of fibril adhesives.

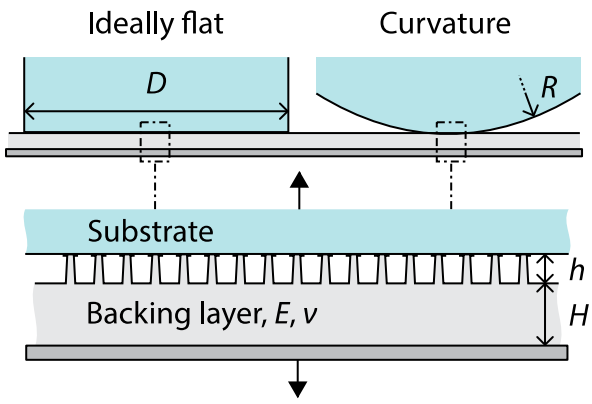

Figure 2.5. Schematic of a synthetic fibrillar adhesive consisting of an array of surface microstructures, length h, on a backing layer, thickness H. Two idealized substrate geometries are shown. The flat contact is circular with diameter D. The curved substrate has radius R.

Figure 2.5 shows a schematic of a typical adhesive patch consisting of a single level of fibrillar structures on a backing layer of the same component material, as is typical of soft molding fabrication techniques utilized. We limit our attention to systems where backing layer is itself supported by rigid structure, rather than forming a flexible membrane.

It has been proposed that the elastic energy stored in a fibril as it is deformed to the point of failure cannot be transmitted to neighboring regions of the interface, and as such is lost to the separation process. Consequently, when a fibril array forms the interface between two larger bodies, this energy can be considered the dominant contributor to the work of adhesion [40, 46, 49, 50]. This leads to

$$W = \rho\left(\frac{1}{2}\frac{{f_{\max}}^2}{k}\right) \tag{2.44}$$

where ρ is the areal density of fibrils (number per unit area), $f_{\max}$ is the force required to detach a fibril (obtained by multiplying the maximum remote stress by the cross-sectional area of the fibril), and $k = E\pi a^2/h$ is the axial stiffness of the fibril. We immediately observe a benefit associated with increasing the fibril density and the fibril length. Increases in the work of adhesion are limited by the tendency for slender densely packed fibrils to buckle, and thus condense, due to attractive forces between neighbors [7, 41, 48, 50, 100, 101].

If the fibril array and contact dimensions are sufficiently large and the backing layer is sufficiently thick and compliant, then continuum approaches using style of model reviewed in Section 2.4 are possible [50, 68]. In this case, fibrils are sufficiently small as to be considered part of the interface, and their deformation is only implicitly considered through use of the effective work of adhesion of (2.44). As the backing layer compliance or the contact dimensions are reduced, it becomes necessary to explicitly consider the elastic deformation of fibrils. In this regard, modeling efforts have considered fibrils as a continuous elastic foundation [68, 70, 102, 103], or as discrete contact elements [22, 104]. Together, these approaches have been used to study effects of significance to adhesive performance at the array scale. These efforts will now be reviewed in detail.

We first consider contact with an ideally flat rigid substrate. If the backing layer is thin, such that it can be considered rigid, the load distribution among fibrils will be uniform. The resulting adhesive strength of the array will be

$$\sigma_{\max} = \rho f_{\max} \tag{2.45}$$

where once again we note that the density will be limited by fibril condensation. If the backing layer is compliant, it is anticipated based on the discussion of Section 2.4.2 that there will be a load concentration at the contact edge. If backing is sufficiently thick and the contact is sufficiently large then these solutions can be used directly [50, 68]. If it is assumed that the backing layer extends laterally, beyond the contact edge, then the solution for contact of a rigid flat-ended cylinder and an elastic half space, given in (2.25), can be utilized. With (2.44) we obtain

$$\sigma_{\max} = \left(\frac{8\rho {f_{\max}}^2}{\pi(1-\nu^2)kD} \right)^{\frac{1}{2}} \tag{2.46}$$

where the D is the contact diameter, which describes the dimensions of the fibril array in contact.

Where the backing layer thickness dictates that the compliance of fibrils can no longer be neglected, they have been modeled as an elastic foundation on a finite thickness elastic layer. The conditions for flaw-insensitivity were considered by Kim et al. [102] and an approximate solution was provided by Long et al [70]. It was shown that the strength scales as $\sigma_{\max} \propto \rho f_{\max}/\sqrt{\beta}$ where β is a monotonically increasing function of the dimensionless ratios $\rho kD/E$ and H/D.

Together these efforts have demonstrated that, for ideally flat substrate and with a backing layer which is compliant relative to fibril layer, the strength of large arrays strength will be governed by nucleation of detachment at the array edge. Furthermore, the strength will decay with increasing array size. This is problematic for scaling of fibril adhesive patch sizes to meet the requirements of engineering applications, and necessitates the utilization of structural hierarchy. Consider that if the array size is limited then it is possible to obtain a uniform load distribution and approach the upper bound on strength given in (2.45). Equating the limits of (2.45) and (2.46) we obtain the critical array diameter

$$D_{\mathrm{t}} = \frac{8}{\pi(1-\nu^2)\rho k} \tag{2.47}$$

An equivalent condition was used by Yao et al. [50] to guide the design of a multi-level fibrillar structure, where the fibril stiffness in each layer was constrained by a fibril buckling condition and the condition for uniform distribution of the load was obtained by equating to the intrinsic strength of the preceding level.

An addition to designing for improved strength, the preceding result is important for the interpretation of results in adhesion tests performed using a punch-like indenter. We observe that the backing layer compliance will render the result dependent on the dimensions of the contact, which may lead to issues in comparing the strength of fibrils characterized using different indenter sizes.

The effect of substrate curvature has also been considered. The limit of a rigid backing layer was considered by Schargott et al. [103] using a model based on approximation of the fibrils as an elastic foundation. It was shown that the maximum strength, as represented by the detachment force, is

$$F_{\max} = \frac{\pi R \rho {f_{\max}}^2}{k} \tag{2.48}$$

which is in agreement with the Derjaguin limit for rigid spheres given in (2.6), when the effective work of adhesion of (2.44) is invoked. It was also shown that in the presence of adhesion hysteresis (jump-in to contact of individual fibrils occurring at considerably shorter separations than upon detachment), a critical compressive preload must be achieved in order to observe the level of strength reported in (2.48). This, as well as the dependence of the detachment force on the radius, R, is of considerable importance for comparison between adhesion tests using spherical probes [105].

For a compliant backing layer, the result of JKR theory given in (2.39) can be employed. This gives

$$F_{\max} = \frac{3}{4}\frac{\pi R \rho {f_{\max}}^2}{k} \tag{2.49}$$

where once again the backing layer compliance is observed to negatively impact strength. In this context the validity of JKR theory, as dictated by (2.41), requires that the ratio

$R\rho k f_{\max}/E^2 > 1000$. The result of (2.49) will consequently be valid when the contact is large, and the backing layer is compliant relative to the fibrils. A result for intermediate cases is only available in the plane strain limit, as reported by Long et al. [68].

The response of arrays subject to roughness on the length scale of the fibrils has also been considered. Persson [40] modeled fibrils as discrete elastic contacts and considered the energetics of the detachment process for a prescribed probability distribution of roughness height. It was demonstrated that the effective work of adhesion was of the form of (2.44), but modified by a coefficient which is a monotonically decreasing function of the ratio of characteristic roughness amplitude to the elongation of a fibril at detachment. Bhushan et al. [106] and Kim et al. [30] have also presented models based on discrete elastic elements, considering both single-level and multi-level hierarchy, evidencing the benefit of the later in regard to maintaining adhesive strength in the presence of roughness on the scale of fibrils. A similar model was presented by Schargott [43].

Statistical distribution in fibril adhesive strength was first considered by Hui et al. [107], on the basis of the historical statistical theory of the strength of thread bundles [108]. Assuming that the load distribution among fibrils was uniform and adopting a power law distribution for their adhesive strength, it was demonstrated that the strength of the array will decay monotonically with increasing variability. This was built upon by Porwal et al. [109], who additionally considered substrate roughness on the length scale of fibrils and performed Monte Carlo simulations to determine the resulting strength. McMeeking et al. [45] later hypothesized that defect-dependent detachment of fibrils should follow the statistical theory of fracture

[110]. Under the assumption of validity of the empirical defect density function of Weibull, it was shown that the scaling of adhesive strength with contact perimeter was dependent on the distribution of defect size, potentially reconciling discrepancies across experimental studies.

Chapter 3

Modeling interfacial misalignment and backing layer compliance

3.1 Introduction

Building upon the work highlighted in Section 2.5, there is considerable need for further investigation of adhesive strength at the array-scale. Previous investigations have highlighted that mechanical coupling of fibrils through a compliant backing layer gives rise to a circumferential load concentration, leading to detachment of fibrils beginning at the contact edge [70]. However, only ideal loading of a flat-on-flat interfacial configuration was considered. The adhesive strength under non-ideal loading conditions may alter or preclude the role of the circumferential load concentration, and associated disadvantage of backing layer compliance. Limiting our attention to the performance of millimeter-scale fibrillar adhesive patches designed for normal adhesive strength on smooth flat surfaces, we identify interfacial misalignment as the primary perturbation to ideal loading conditions. From laboratory experiments the adhesion force in flat-on-flat configurations is known to be sensitive to alignment [69]. Careful control using leveling systems is required. However, many synthetic fibrillar adhesives are designed for application in flat-on-flat configurations without precise control of alignment, e.g. pick-and-place grippers. We consider a flat-on-flat geometry,

removing the requirement for perfect alignment during separation of the adhesive and the contacting surface. We examine how the load distribution, detachment characteristics, and adhesive strength are impacted by the combined effects of backing layer mechanical coupling and misalignment.

3.2 Theoretical model

3.2.1 Analytical formulation

Figure 3.1 shows a schematic of the mechanical model utilized in this investigation. It is based on the example of Noderer *et al.* [22] and Guidoni *et al*. [104]. The model adhesive is comprised of an array of fibrils atop a backing layer composed of the same linear elastic, isotropic material. Fibrils are cylindrical with radius, a, and undeformed length, h. They are distributed in a square array with the distance between the centers of nearest neighbor fibrils, d. Globally, we consider a rectangular array for which n_x and n_y are the number of fibrils along the x- and y-axes, respectively. The total number of fibrils is $N = n_x n_y$. The reference system x, y, z is centered at the base of a reference fibril located at one of the corners of the array. Two limits on the backing layer thickness, and thus its compliance, are considered. In one limit $H = 0$, such that the rigid tile below the backing layer supports the fibril array. In the other limit the backing layer is considered to be an elastic half-space, so that it has infinite thickness, $H = \infty$, and extends indefinitely in the x and y directions. Fibrils contact a rigid substrate at their tip. A remote load acts to detach the adhesive from the substrate, generating a relative displacement of the substrate at a fixed angle of misalignment. Misalignment angles,

θ_x and θ_y, about the x- and y-axis respectively, are defined so that when they are both non-zero and positive, the fibril at the origin ($x = y = 0$) experiences the smallest displacement.

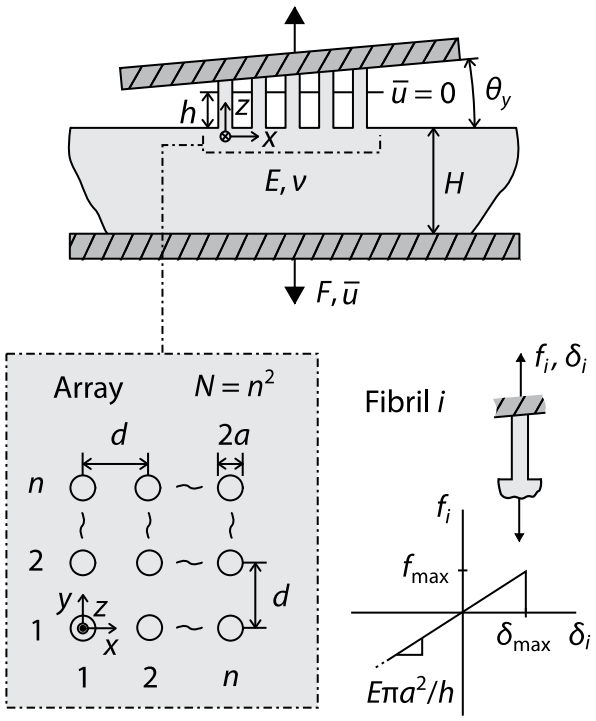

Figure 3.1. Schematic of the mechanical model for investigation of backing layer compliance and interfacial misalignment. The fibrillar array and backing layer material has Young's modulus, E, and Poisson ratio, ν. Fibrils are arranged in a square array, with characteristic fibril spacing d. Globally we consider a rectangular array for which n_x and n_y are the number of fibrils along the x- and y-axes, respectively, with the total number of fibrils being $N = n_x n_y$. Each fibril has radius a, and undeformed length h. The force, F, generates a relative displacement of the substrate, $\bar{u}$, at a fixed angle of misalignment about each axis, θ_x (not visible) and θ_y. In contact, individual fibrils respond as one-dimensional linear elastic elements, with the load and elongation of fibril i being f_i and δ_i, respectively. We assume unstable defect-controlled detachment of individual fibrils at tensile load $f_{\max}$.

Before considering the behavior of the adhesive sample in contact with the test surface further, we must first consider mechanical behavior an individual fibril. The intrinsic adhesive properties of the interface at the tip of an individual fibril are encompassed by the work of adhesion, W, defined as the energy per unit area required to generate absolute separation of the interface, and the intrinsic strength, σ_0, defined as the maximum force per unit area supported by the fibril-substrate interface during separation. Linear elastic fracture mechanics predicts defect-controlled detachment when the defect size exceeds $E^*W/{\sigma_0}^2$. For the van der Waals interaction occurring at the interface of an elastomer and a much stiffer substrate, this is on the order of nanometers. At the fibril tip we anticipate the presence of defects far exceeding this limit, and consequently expect defect-controlled detachment. We therefore consider the fibril to behave as a one-dimensional element which exhibits a linear elastic response up to a maximum tensile load, $f_{\max}$, at which point detachment of the fibril occurs in an unstable manner via propagation of a defect. This load represents the adhesive strength of an individual fibril. It is assumed that the fibril strength is uniform across the array, i.e. it is deterministic in nature. The significance of this assumption is discussed in Chapters 5 and 6.

Axial deformation of fibrils leads to the development of elastic force, f_i, equilibrated by intermolecular forces at the fibril tip. The sum of the forces developed in all fibrils in contact with the substrate must equilibrate the total force, therefore

$$F = \sum_{i=1}^{N} f_i \tag{3.1}$$

The maximum load supported by the fibrillar array is $F_{\max}$. While the simulations described are performed in displacement control, this is termed the detachment force on account of it being the point of instability in a load-controlled measurement. The theoretical bound on the strength of the fibril array corresponds to a uniform load distribution among fibrils, leading to simultaneous detachment across the array as the local load at each fibril exceeds $f_{\max}$. In this case the detachment force $F_{\max} = Nf_{\max}$. When the detachment force is normalized as $F_{\max}/Nf_{\max}$, we obtain a measure of the efficiency with which the fibril adhesive strength is harnessed at the array scale. Given that the area occupied by the array is proportional to the total number of fibrils, $F_{\max}/Nf_{\max}$ can alternatively be interpreted as a dimensionless and normalized form of the maximum stress supported by the fibrillar array i.e. its adhesive strength.

The displacement at the tip of the i–th fibril is

$$u_i = \bar{u} + x_i \tan\theta_y + y_i \tan\theta_x \tag{3.2}$$

where x_i and y_i are the coordinates that identify the position of the center of the fibril and $\bar{u}$ is the displacement, as defined in Figure 3.1. The tip displacement at the reference fibril is $\bar{u}$ and, assuming $\theta_x \geq 0$ and $\theta_y \geq 0$, the displacement for all other fibrils in contact is greater than this value. All tests consist of an approach phase ($\mathrm{d}\bar{u} < 0$) and a separation phase ($\mathrm{d}\bar{u} > 0$). In the approach phase it is ensured that contact is generated with all fibrils in the array. Where

misalignment is present, this necessitates that fibrils are shortened. The response of shortened fibrils is discussed subsequently.

The displacement, u_i, in (3.2) is the result of elastic deformation of the backing layer and of the i–th fibril, and thus by linear superposition

$$u_i = u_i^{\mathrm{fib}}(f_i) + \sum_{j=1}^{N} u_i^{\mathrm{BL}}(f_j) \tag{3.3}$$

The first term is the displacement accommodated by tensile strain on fibril i under the action of the force it experiences, f_i. The second term is the displacement due to elastic deformation of the backing layer at the base of fibril i. It is the result of load transmitted through each fibril to the backing layer, both locally ($f_j\ \forall j = i$) and by other fibrils in the array ($f_j\ \forall j \neq i$).

The displacement accommodated by tensile strain on the fibril, the first term on the right hand side of (3.3), is

$$u_i^{\mathrm{fib}}(f_i) = \frac{h f_i}{\pi a^2 E} \tag{3.4}$$

In the limit $H = \infty$, from Johnson's solutions for normal loading of an elastic half-space [90] we obtain the second term on the right hand side of (3.3) as

$$u_i^{\mathrm{BL}}(f_j) = \frac{f_j}{\pi r_{ij} E^*} \qquad \forall\, j \neq i$$
$$u_i^{\mathrm{BL}}(f_j) = \frac{16 f_j}{3\pi^2 a E^*} \qquad \forall\, j = i \tag{3.5}$$

where $E^* = E/(1-\nu^2)$, with E and ν being the Young modulus and the Poisson ratio of the backing layer, respectively. The distance separating the centers of the i–th and the j–th fibrils is r_{ij}. The result for $j \neq i$ is obtained when we approximate the pressure applied to the half-space at the base of fibril j with the resulting point force f_j applied at the center of its cross-section. We assume that the base displacement of fibril i which results is given by Johnson's formula, applied at the center of its cross-section. This is proven to give a maximum error that is within 3.5 % when compared to the solution for uniform pressure loading of the half-space, as reported in Appendix A. The result for $j = i$ is the average displacement of the cross-section of fibril j which results from a uniform pressure load applied to its section.

Eq. (3.3) can be rewritten in matrix form by substitution of (3.4) and (3.5), giving

$$u_i = c_{ij}\, f_j \tag{3.6}$$

where the compliance matrix, $\boldsymbol{c}$, has the components

$$c_{ij}{}^{H=0} = \frac{h}{\pi a^2 E} \quad \forall\, j = i \tag{3.7}$$

$$c_{ij}{}^{H=0} = 0 \quad \forall\, j \neq i$$

in the rigid backing layer limit and

$$\begin{aligned} c_{ij}{}^{H=\infty} &= \frac{1}{\pi r_{ij} E^*} \qquad \forall j \neq i \\ c_{ij}{}^{H=\infty} &= \frac{1}{\pi a E^*}\left[\frac{16}{3\pi} + \frac{h}{a(1-\nu^2)}\right] \qquad \forall\, j = i \end{aligned} \tag{3.8}$$

in the fully compliant limit. Mechanical coupling of fibrils via the off-diagonal terms of the compliance matrix of (3.8) is henceforth referred to as the backing layer interaction. Defining the stiffness matrix, $\boldsymbol{k} = \boldsymbol{c}^{-1}$, we find that inversion of (3.6) gives

$$f_j = k_{ji}\, u_i \tag{3.9}$$

When f_j is negative, the j–th fibril is in compression. The critical buckling load, f_{b}, represents the maximum compressive load which can be sustained, where we assume that upon further compression the post-buckling behavior of fibrils involves a fixed compressive load [111]. In the following sections all physical cases of finite and non-zero f_{b} are considered within the bounds of two limits, namely ideally slender fibrils ($f_{\mathrm{b}} = 0$) and ideally short fibrils ($f_{\mathrm{b}} = -\infty$). In the limit $f_{\mathrm{b}} = 0$, the total load during approach is zero and the separation phase begins when all fibrils contact the substrate. In the limit $f_{\mathrm{b}} = -\infty$, a compressive load is generated during approach. Separation begins when a specified preload, F_0, is met. In all cases examined, the preload specified is sufficient to bring all fibrils in to contact. It is assumed that upon

unbuckling the tip contact is reformed and the local detachment force is unaffected. The validity of this assumption will depend on the tip geometry; most significantly this feature has been demonstrated to hold for mushroom-tipped fibrils at moderate preloads [57].

Substituting (3.2) into (3.9) we obtain

$$f_j = \bar{u}\left(\sum_{i=1}^{N} k_{ji}\right) + k_{ji}x_i \tan\theta_y + k_{ji}y_i \tan\theta_x \tag{3.10}$$

With substitution of (3.10) into (3.1) we obtain the total load supported by the fibril array, F, as a function of the prescribed displacement, $\bar{u}$. However, we note that when the prediction of (3.10) for fibril j is such that $f_j < f_{\mathrm{b}}$, we then use $f_j = f_{\mathrm{b}}$ in the determination of the total force. Similarly, when $f_j > f_{\max}$ then the fibril detaches and $f_j = 0$ in the determination of the total force.

3.2.2 Numerical implementation

To facilitate ease of assessment of the adhesive strength of the fibril array, the total load is normalized as

$$\tilde{F} = F/Nf_{\max} \tag{3.11}$$

We define the dimensionless prescribed displacement as

$$\tilde{u} = \left(\frac{\bar{u}}{a}\right)\frac{\pi a^2 E^*}{f_{\max}} \tag{3.12}$$

This leads to the following expression for the dimensionless displacement at fibril i

$$\tilde{u}_i = \tilde{u} + \frac{\pi a^2 E^*}{f_{\max}}\frac{x_i}{a}\tan\theta_y + \frac{\pi a^2 E^*}{f_{\max}}\frac{y_i}{a}\tan\theta_x \tag{3.13}$$

where x_i/a, and y_i/a are linearly related to the fibril separation, d/a, specified within the model.

When considering misalignment, compatibility limits the possible range of the misalignment angles θ_x and θ_y. We limit the misalignment angle according to the condition that when all fibrils in the array contact the substrate, there should not be interference between the backing layer and substrate where the displacement is smallest. We also neglect interference of the substrate and backing layer outside of the fibrillar region, implying that the contact is finite in size. The resulting compatibility limit is

$$(n_x - 1)\tan\theta_y + \left(n_y - 1\right)\tan\theta_x \leq \frac{h}{d} \tag{3.14}$$

For simplicity in the consideration of compatibility we consider only unidirectional misalignment, $\theta_x = 0$ and $\theta_y = \theta$. In the sections which follow we explore variation in the

parameters n_x, n_y, h, and d, and so compatibility must be considered on a case by case basis according to (3.14). Within the bounds of compatibility for a given system, the range of misalignment adopted is such that all physical features of interest are revealed.

Furthermore, (3.13) dictates that to study misalignment we must assign a value to the term $f_{\max}/\pi a^2 E^*$. This is closely related to the strain on a fibril at detachment, differing only by a factor of $1-\nu^2$. Elastomeric mushroom-tipped fibrils typically exhibit detachment stresses on the order of 100 kPa. With an elastic modulus on the order of 1 MPa, we obtain an estimate on the critical strain of 10 %. We therefore choose to adopt $f_{\max}/\pi a^2 E^* = 0.1$. Provided that compatibility is independently ensured, the results presented will hold for systems in which $f_{\max}/\pi a^2 E^* \neq 0.1$ provided $\tan\theta$ is replaced with $\pi a^2 E^* \tan\theta / f_{\max}$ when one reads the results of Section 3.3.

A simulation commences with the dimensionless prescribed displacement $\tilde{u} = 0$. During approach the displacement is reduced by $\mathrm{d}\tilde{u}$. Contact is assessed on a fibril by fibril basis according to the relative position of the substrate and fibril tip. 'Jump-into-contact' of individual fibrils, which may occur in the presence of adhesive forces, is not considered. This is deemed a valid assumption as it typically occurs at separation distances much smaller than the critical stretch of a fibril. For each incremental step, rows and columns of the compliance matrix corresponding to fibrils not in contact are eliminated on the basis that $f_j = 0$. The reduced compliance matrix is then inverted to obtain the reduced stiffness matrix, and the force in each fibril in contact is computed from (3.10). If it predicts that the load in fibril j exceeds the detachment load such that $f_j > f_{\max}$, this fibril detaches. The compliance matrix is further

reduced, and the force is recomputed until no further detachments occur. The displacement is incremented and the process is repeated.

The choice of $\mathrm{d}\tilde{u}$ involves a trade-off between accuracy and computation time. For all of the results presented the incremental step in the prescribed dimensionless displacement is $\mathrm{d}\tilde{u} = 0.01$.

3.2.3 Analytical solution for rigid backing layer

Consideration of the solution for the case of a rigid backing layer, $H = 0$, is useful for isolating the effect of backing layer interactions from that of misalignment. For unidirectional misalignment the problem permits the following analytical approach.

Compliance terms associated with backing layer deformation are zero, hence compliance is given by (3.7). Since this is diagonal, it can easily be inverted to obtain an expression for the load. Combining the resulting stiffness matrix with (3.1) and (3.10) gives

$$F = \frac{\pi a^2 E}{h}\left[N_{\mathrm{a}}\bar{u} + \left(\sum_{i=1}^{N_{\mathrm{a}}} x_i\right)\tan\theta\right] \tag{3.15}$$

The displacement at maximum load, $F = F_{\max}$, is obtained by considering the condition of 'first detachment', when the first row of fibrils instantaneously experiences critical elongation, $\delta_{\max} = f_{\max}h/(\pi a^2 E)$ and is about to detach.

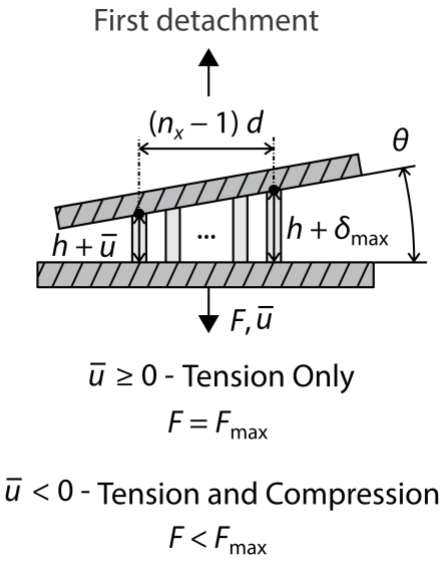

Figure 3.2. Configuration of the model system with rigid backing layer, $H = 0$, at the instant of first detachment. The elongation of fibrils at the right edge is $\delta_{\max} = f_{\max}h/(\pi a^2 E)$. The misalignment angle, θ, dictates whether first detachment occurs when the displacement $\bar{u} \geq 0$, in which case all fibrils are in tension, or $\bar{u} < 0$, in which case a region of fibril compression exists at the left edge of the array.

Figure 3.2 shows the configuration of the array at first detachment. For a given misalignment angle, θ, there are two possible regimes. If first detachment occurs when $\bar{u} \geq 0$ then all fibrils are in tension and the force is maximum in this configuration. This becomes clear when considering the detachment of the second row of fibrils. The configuration will have evolved in a self-similar manner but for the row furthest from the detachment front, which is no longer present. Since this row previously held tensile load, the total force is reduced for this and all subsequent detachments.

For the first regime, the critical value of the prescribed displacement, $\bar{u}$, is obtained from the geometry in Figure 3.2 as

$$\bar{u}_{\mathrm{c}} = \delta_{\max} - (n_x - 1)d\tan\theta \tag{3.16}$$

All fibrils are attached such that $N_{\mathrm{a}} = N$, and the sum of the x-positions of attached fibrils is

$$\sum_{i=1}^{N} x_i = \frac{1}{2}N(n_x - 1)d \tag{3.17}$$

Combining (3.15)-(3.17), we obtain the normalized detachment force

$$\frac{F_{\max}}{Nf_{\max}} = 1 - \frac{\pi a^2 E}{2f_{\max}}(n_x - 1)\tan\theta\ \frac{d}{h} \tag{3.18}$$

In the second regime, where first detachment occurs when $\bar{u} < 0$, a portion of the array is shortened. If fibrils respond elastically in compression (limit $f_{\mathrm{b}} = -\infty$) then, as fibril detachment progresses, the tensile region will evolve in a self-similar manner. Rows transition from compressive to tensile at the same rate as rows detach. This progressively reduces the compressive contribution to the total load. The maximum force will occur in the configuration for which no row of fibrils remains in compression. Consequently the critical prescribed displacement is always $\bar{u}_{\mathrm{c}} = 0$. Alternatively, if fibrils buckle under negligible load (limit $f_{\mathrm{b}} = 0$) then the tensile region also evolves in a self-similar manner. The total load is constant

throughout this evolution. Any configuration, including that in which $\bar{u}_{\mathrm{c}} = 0$, can be analyzed to determine the maximum load.

Figure 3.3 shows this configuration in which $\bar{u}_{\mathrm{c}} = 0$. The number of fibrils in contact is

$$N_{\mathrm{a}} = n_y \left(\frac{\delta_{\max}}{d \tan\theta} + 1 \right) \tag{3.19}$$

The sum of the x-positions of attached fibrils is

$$\sum_{i=1}^{N_{\mathrm{a}}} x_i = \frac{1}{2} n_y \left(\frac{\delta_{\max}}{d \tan\theta} + 1 \right) \frac{\delta_{\max}}{\tan\theta} \tag{3.20}$$

Knowing $\bar{u}_{\mathrm{c}} = 0$, we combine (3.15), (3.19) and (3.20) to obtain the detachment force

$$\frac{F_{\max}}{N f_{\max}} = \frac{1}{2 n_x} \left[1 + \frac{f_{\max}}{\pi a^2 E} \frac{h}{\tan\theta \, d} \right] \tag{3.21}$$

The transition misalignment angle, θ_{t}, is obtained by analyzing the configuration in Figure 3.2 with $\bar{u} = 0$, yielding

$$\tan\theta_{\mathrm{t}} = \frac{f_{\max}}{\pi a^2 E} \frac{h}{d(n_x - 1)} \tag{3.22}$$

When the misalignment angle, θ, is in the range $0 \leq \theta \leq \theta_t$ then the detachment force is given by (3.18), while for $\theta > \theta_t$ it is given by (3.21).

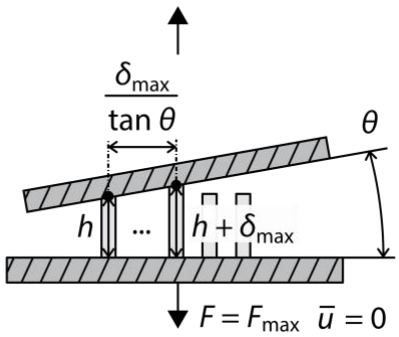

Figure 3.3. Configuration of model system with rigid backing layer, $H = 0$, at maximum load, $F = F_{max}$, for misalignment angle $\theta > \theta_t$ i.e. for which regions of tension and compression exist at first detachment.

3.3 Results

3.3.1 Effect of backing layer compliance

Figure 3.4 shows the force-displacement curve for an aligned system, $\theta = 0$. We examine a square array for which $n_x = n_y = 30$, the total number of fibrils being $N = 900$. The fibril length and spacing are $h = 5a$ and $d = 5a$, respectively.

During approach, the response of fibrils in compression must be considered. As, highlighted in Section 3.2, two limits on the bucking load, $f_b = -\infty$ and $f_b = 0$, are considered. For fibrils which respond elastically in compression ($f_b = -\infty$), the preload $F_0/Nf_{max} = -0.5$ is specified. Since all fibrils contact the substrate simultaneously, there is no difference in the stiffness during approach and retraction. If fibrils buckle under negligible compressive load

($f_b = 0$) then compressive preload cannot be applied, but the response in tension is identical to the preceding case. We therefore observe no difference between the two limits.

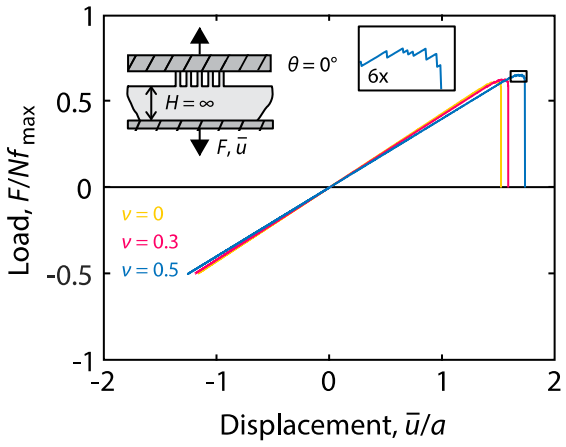

Figure 3.4. Force-displacement curve for the aligned state, $\theta = 0$. The normalized detachment force, F_{max}/Nf_{max}, is 0.62, 0.63, and 0.66 for Poisson ratio, ν, of 0, 0.3, and 0.5, respectively. The inset shows a six-fold magnification close to the maximum tensile load, evidencing drops in the load associated with fibril detachments. The bucking limits $f_b = -\infty$ and $f_b = 0$ are considered, but are indistinguishable.

The force-displacement curve exhibits a significant drop in F every time a set of fibrils detach, with this drop only being resolved in displacement control. Non-simultaneous detachment dictates that the load distribution is non-uniform, and thus the adhesive strength of the array is reduced. The normalized detachment force, $F_{max}/Nf_{max} < 1$. As the displacement is increased, the effective stiffness of the adhesive system, $dF/d\bar{u}$, is monotonically reduced as fibrils continue to detach, falling to zero at complete detachment. We note that the maximum value of the total force, F_{max}, is the point at which detachment would occur in an unstable manner in load control.

Figure 3.5 demonstrates the evolution of detachment in the aligned state. We examine the point of maximum load, $F = F_{\max}$, for the case of $\nu = 0.5$. An array edge load concentration results as we transition from the bulk. Diminished backing layer deformation at the base of array edge fibrils is the result of a reduction in nearest neighbors. A larger share of the prescribed displacement must be accommodated by fibril stretching, resulting in load concentration. Fibrils at the array corners, where the reduction in neighbors is most pronounced, exceed their critical load first and detach. This leads the shape of the attached portion of the array to evolve toward that of a circle, where the number of neighboring fibrils is uniform around the perimeter.

Returning briefly to Figure 3.4, we initially explore three values of Poisson ratio. It is observed that an increase in the Poisson ratio yields an increase in the adhesive strength of the array. Specifically, the normalized detachment force is increased from $F_{\max}/Nf_{\max} = 0.62$ for $\nu = 0$ to $F_{\max}/Nf_{\max} = 0.66$ for $\nu = 0.5$. This is a result of lateral contraction/expansion of the backing layer limiting its compliance and thus inhibiting the interaction that leads to load concentration at the array edge. From this point on we proceed with $\nu = 0.5$, representative of the incompressible elastomeric materials typically used to fabricate synthetic fibrillar adhesives.

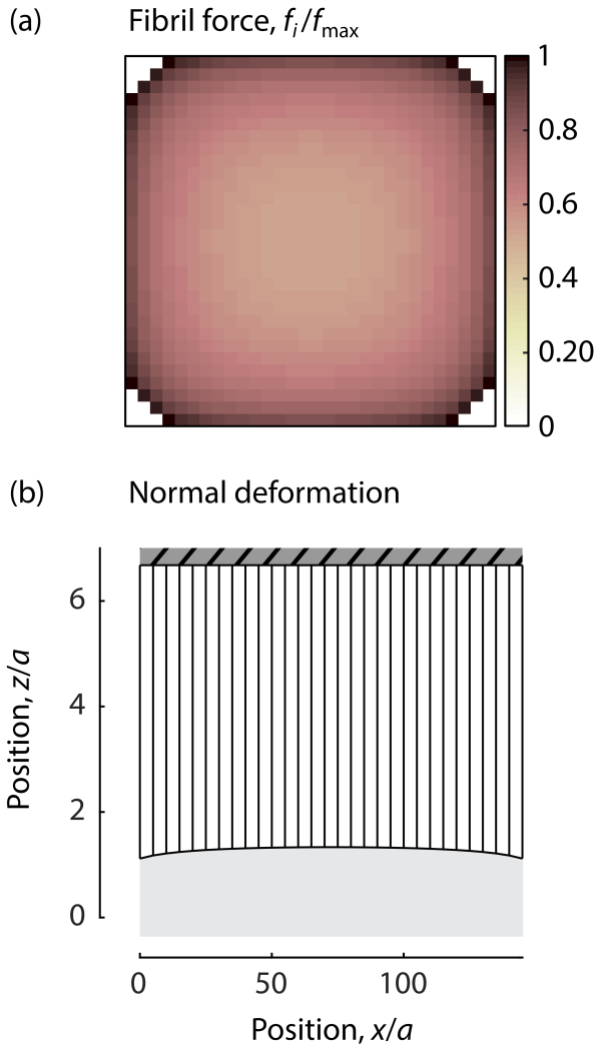

Figure 3.5. Load distribution and normal deformation of model fibrillar adhesive in the aligned state, at maximum tensile load $F = F_{\max}$; (a) Fibril force, $f_i/f_{\max}$; (b) Normal deformation for a section through the center of the array, parallel to the x-axis. Note that the scale of x and z are not equal.

3.3.2 Effect of misalignment

Figure 3.6 shows the force-displacement curve for the aligned state, and for two values of the misalignment angle, θ. The presence of misalignment leads to differences in behavior of the two limiting cases of the fibril bucking load, f_{b}, described in Section 3.2. If fibrils respond

elastically in compression ($f_b = -\infty$, solid line) then during approach the stiffness of the system increases as fibrils progressively contact the substrate. If fibrils buckle under negligible compressive load ($f_b = 0$, dashed line) then the load is zero during approach. Upon contact with all fibrils, the stiffness increased as fibrils are brought in to tension and contact at the tip is reformed. Eventually, upon reaching the state in which all fibrils are in contact and bear tensile load, the behavior in each case is indistinguishable.

It is apparent from the normalized detachment force, F_{max}/Nf_{max}, that increasing misalignment results in a more severe load concentration, and a greater reduction in the adhesive strength of the fibril array.

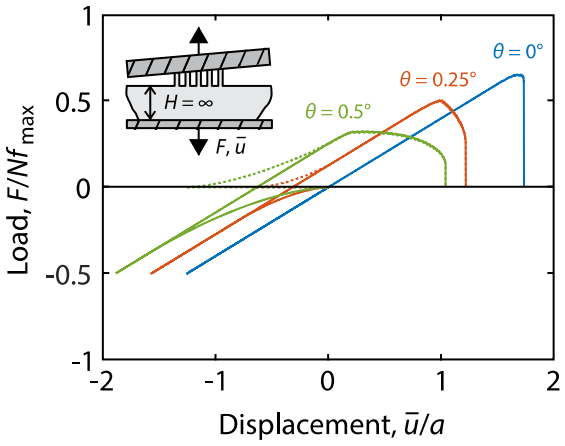

Figure 3.6. Force-displacement curves for three values of the misalignment angle, θ. The normalized detachment force, F_{max}/Nf_{max}, is 0.66, 0.50, and 0.32 for misalignment angles $\theta = 0$, $\theta = 0.25°$, and $\theta = 0.5°$, respectively. The bucking limits $f_b = -\infty$ (solid lines) and $f_b = 0$ (dashed lines) are considered.

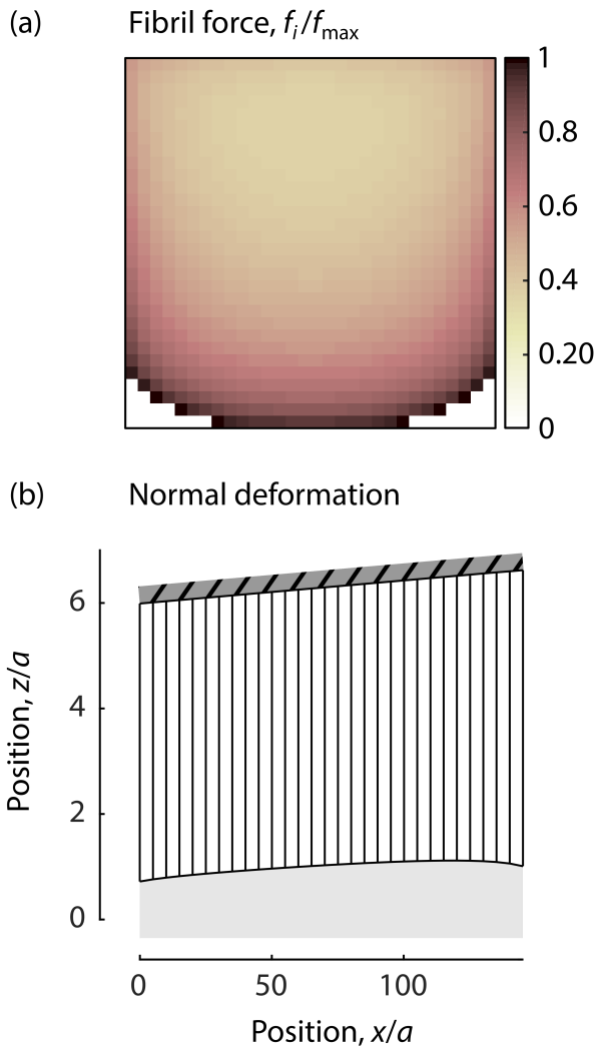

Figure 3.7. Load distribution and normal deformation of model fibrillar adhesive in a misaligned state, $\theta = 0.25°$, at maximum tensile load $F = F_{\max}$; (a) Fibril force, $f_i/f_{\max}$; (b) Normal deformation along for a cut through the center of the array, parallel to the x-axis. Note that the scale of x and z are not equal.

Figure 3.7 highlights the evolution of detachment for the system, with misalignment, $\theta = 0.25°$. Once again, we examine the point of maximum load, $F = F_{\max}$. As the prescribed displacement, $\bar{u}$, is increased, the bias for fibril deformation at one edge of the array persists

resulting in initial detachment at this edge and the propagation of the detachment front across the array.

Although not examined quantitatively here, when bidirectional misalignment is considered and compatibility is ensured the detachment front propagates in the direction of maximum misalignment. The tangent of the angle subtended by the detachment front and the x-axis is approximately equal to the ratio $\tan\theta_x / \tan\theta_y$. Reduced adhesive strength is observed in mutual combination for both misalignment angles being nonzero and positive.

3.3.3 Effect of array size

In Figure 3.8 we examine a square array ($n_x = n_y = n$) and report the influence of the total number of fibrils, $N = n^2$, on the normalized detachment force, $F_{\max}/Nf_{\max}$. Both a rigid backing layer, $H = 0$, and a fully compliant backing layer, $H = \infty$, are examined in the aligned state and with misalignment, $\theta = 0.25°$. This allows for the isolation of backing layer and misalignment effects, as well as examination of their influence in combination.

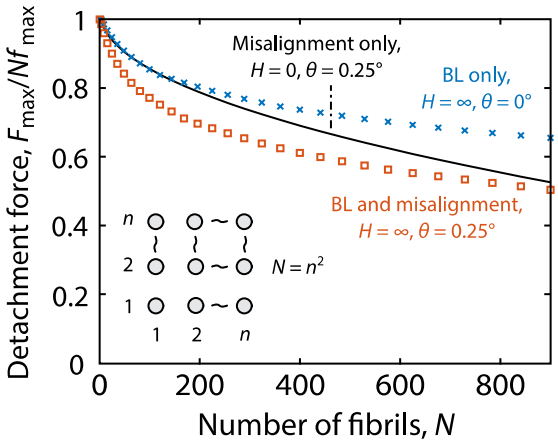

Figure 3.8. Normalized detachment force, $F_{\max}/Nf_{\max}$, versus the total number of fibrils, N. A square array of fibrils for which $n_x = n_y = n$ and $N = n^2$ is examined. Results are presented for a rigid backing layer, $H = 0$, for which the result is given by (3.18) and (3.21), and a compliant backing layer, $H = \infty$. For the aligned state, the rigid backing layer achieves a uniform load distribution and the theoretical maximum strength independent of the fibril separation. Consequently $F_{\max} = Nf_{\max}$, and the result is not visible on the plot. We distinguish the three remaining results on the basis of the presence of backing layer compliance (BL) and misalignment.

For model adhesive on a rigid backing layer in the aligned state it is known that the load distribution is uniform. The upper bound on adhesive strength of the array is achieved independent of the array size. Introduction of backing layer compliance (BL only) results in a monotonic decay in the adhesive strength of the array with increasing size, is associated with an increase in the severity of the array edge load concentration. This has been highlighted in past work [70, 102]. It should be noted that asymptotic scaling associated with the limit of an infinitely thick backing layer presented in previous studies, which would predict that $F_{\max}/Nf_{\max} \propto 1/N^{1/4}$, is not observed. Consideration of the approximate size of the fracture process zone reveals the reason for this. Adopting the effective work of adhesion of (2.44),

and identifying that the intrinsic strength is $f_{\max}/d^2$, the normalized size of the fracture process zone is approximately $\tilde{d}^2\tilde{h}$. For the system examined, this is of order 10^2. For the maximum array size examined, the normalized dimensions are of the same order. Linear elastic fracture mechanics solutions cannot, therefore, be used with validity.

With only misalignment, we also observe that there is a monotonic decay in adhesive strength of the array with increasing array size. Introducing backing layer compliance in combination, the reduction in strength is seen to be more severe for small array sizes. However, for large arrays the results for each limit on backing layer compliance converge. This suggests that interfacial misalignment is the dominant effect controlling the adhesive strength of the array in this regime.

3.3.4 Effect of fibril spacing and length

Figure 3.9 demonstrates the effect of fibril spacing, d, on the normalized detachment force, $F_{\max}/Nf_{\max}$. As before, both a rigid backing layer, $H = 0$, and a compliant backing layer, $H = \infty$, are examined in the aligned state and with misalignment, $\theta = 0.25°$.

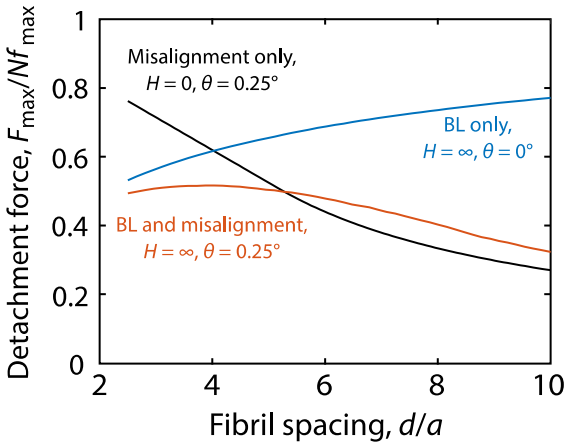

Figure 3.9. Normalized detachment force, $F_{\max}/Nf_{\max}$, versus the fibril spacing, d/a, for the aligned state and for a misaligned state with $\theta = 0.25°$. As before, results are distinguished on the basis of the presence of backing layer compliance (BL) and misalignment.

With only misalignment the difference in displacement between two arbitrary fibrils, and the resulting load concentration, is linearly proportional to the fibril separation, d. This proportionality translates to the decay in the adhesive strength of the array, as represented by the normalized detachment force $F_{\max}/Nf_{\max}$ given in (3.18) and (3.21).

For the aligned state, increased fibril spacing yields a monotonic increase in the adhesive strength of the array. Individually, elastic interactions associated with the backing layer compliance are known to decay as $1/r_{ij}$. Consequently, the collective effect is reduced as fibril spacing is increased. The severity of the array edge load concentration is reduced. In the limit that fibrils are infinitely far apart backing layer interactions decay to zero, and the adhesive strength of the array would tend toward the theoretical limit, with the normalized detachment force $F_{\max}/Nf_{\max} \to 1$.

When considering the combined effect of backing layer compliance and misalignment, the benefit of increased spacing holds also for the misaligned system up to a critical spacing, d^*. This is referred to as the 'backing layer compliance dominated regime'. For the specified misalignment, the critical spacing yields the highest adhesive strength for the compliant backing layer. It represents the transition to the 'misalignment dominated regime'. Here the decay in adhesive strength with fibril separation, which results due to misalignment and was highlighted for the rigid backing layer, prevails over the benefit provided by reduced backing layer interactions. We note that in the case considered, d^* is approximately $4a$.

It is also observed that the decay in the adhesive strength of the array with increased spacing is less severe for the compliant backing layer than the rigid backing layer, and that for sufficiently large spacing the backing layer compliance can be beneficial to the adhesive strength of the array. The mechanism behind this adhesion enhancement is discussed shortly.

Figure 3.10 demonstrates the effect of fibril length, h, on the normalized detachment force, $F_{\max}/Nf_{\max}$. Once again, both a rigid backing layer, $H = 0$, and a compliant backing layer, $H = \infty$, are examined in the aligned state and with misalignment, $\theta = 0.25°$. Increasing fibril length, h, yields increased fibril compliance. Where there is load concentrations, either as a result of backing layer deformation or misalignment, the difference in load is inversely proportional to the fibril compliance. Reduction in the severity of load concentration with increasing fibril length, h, yields a monotonic increase in the adhesive strength of the array for all cases examined, as reflected in the normalized detachment force $F_{\max}/Nf_{\max}$. Once again,

we observe a regime in which the adhesive strength of the array is greater for the compliant backing layer than the rigid, in this case occurring at sufficiently small fibril length.

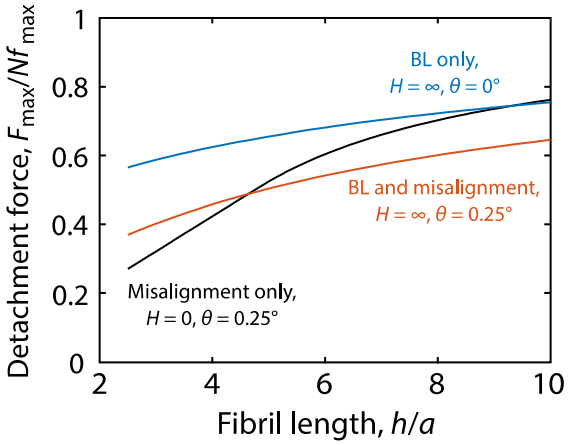

Figure 3.10. Normalized detachment force, $F_{\max}/Nf_{\max}$, versus the fibril length, h/a, for the aligned state and for a misaligned state with $\theta = 0.25$. As before, results are distinguished on the basis of the presence of backing layer compliance (BL) and misalignment.

We have noted that the compliant backing layer can yield improved adhesive strength when misalignment is severe, fibril spacing is large, or fibril compliance is low. This leads to the conclusion that, in this regime, backing layer deformation is counteracting the effect of misalignment. Without misalignment backing layer mechanical coupling was seen to create a load concentration at the array edge, resulting in non-simultaneous detachment and reduced adhesive strength of the array. In the misalignment dominated regime, however, deformation of the backing layer accommodates the largest displacement at the leading edge, decaying as we move away from this edge. This counteracts the differential fibril stretching and load

concentration which results from misalignment. We now seek to characterize the transition between these regimes in greater detail.

Figure 3.11 reports the misalignment an associated with transition between the misalignment dominated and backing layer compliance dominated regimes, as a function of the fibril spacing, d/a. For small arrays and large fibril spacing, the severity of the array edge load concentration due to backing layer compliance is reduced while the differential stretching due to misalignment increases. Consequently, this is associated with an expansion of the regime in which backing layer compliance is beneficial to performance.

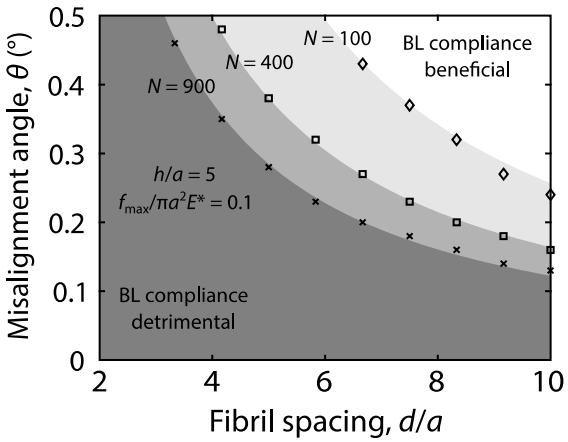

Figure 3.11. Transition misalignment angle versus fibril spacing, d/a. Results are presented for three array sizes. Shaded regions represent the evolution of the backing layer compliance detrimental regime and are based on power law fitting of the form $y = ax^b$.

Figure 3.12 maps the same regimes as a function of the fibril length, h/a. As the fibril length is increased, the range of misalignment angles over which the backing layer compliance plays

a detrimental role expands. This is expected given the result of Figure 3.10, where we observe that increasing the fibril compliance provides a more rapid enhancement of strength in the presence of misalignment than the array edge load concentration.

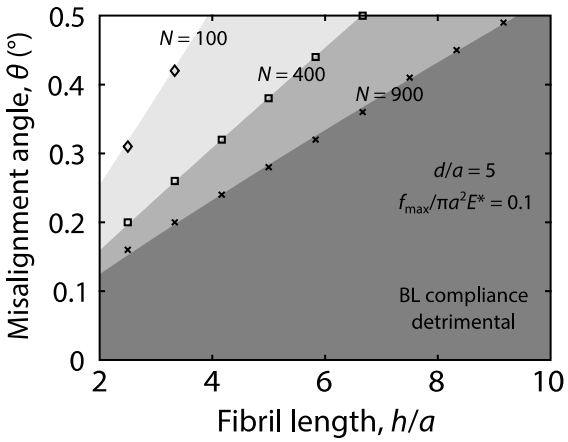

Figure 3.12. Transition misalignment angle versus fibril length, h/a. Results are presented for three array sizes. Shaded regions represent the evolution of the backing layer compliance detrimental regime and are based on power law fitting of the form $y = ax^b$.

3.3.5 Fibril compliance optimization

Thus far it can be observed that adhesive strength of fibrillar arrays has been below the theoretical upper bound, $F_{\max} < Nf_{\max}$, for all cases examined except for the that of a single fibril and an aligned system with a rigid backing layer. The reduction in strength is associated with the nucleation of detachment of a subset of fibrils, and propagation of the detachment front through the array. This has been shown to depend on both backing layer compliance and misalignment, which together control the nature of load concentrations in the fibril array.

Seeking to maximize adhesive strength, we identify that there are several theoretical paths to obtain a uniform load distribution at the instant of detachment. An infinitely stiff or infinitely thin backing layer prevents the elastic interactions which give rise to a load concentration at the array edge. In this case, for perfect alignment only, we reach the theoretical upper bound on strength. An alternative to altering backing layer properties is to manipulate the compliance distribution at the interface to counteract the effects described. For example, fibrils which experience the largest stretch could be made more compliant, and therefore capable of sustaining additional deformation without load concentration. If tailored correctly, backing layer interactions can be harnessed to provide optimal load redistribution, with all fibrils carrying the same load at detachment.

At detachment, such an interface has $f_j = f_{\max}\ \forall j$. In combination with (3.2) and (3.6), we obtain

$$\bar{u}_{\mathrm{c}} + x_i \tan\theta_y + y_i \tan\theta_x = f_{\max}\left(\sum_{j=1}^{N} c_{ij}\right) \tag{3.23}$$

with $\bar{u}_{\mathrm{c}}$ being the critical prescribed displacement at detachment, which cannot be determined a priori. However, since (3.23) holds for each fibril, we may identify an individual reference fibril, k, and rewrite the expression. We take the difference between (3.23) as expressed for both an arbitrary fibril i and the reference fibril k to obtain

$$(x_i - x_k)\tan\theta_y + (y_i - y_k)\tan\theta_x = f_{\max}\sum_{j=1}^{N}\left(c_{ij} - c_{kj}\right), \qquad \forall i \tag{3.24}$$

The compliance can in theory be tailored locally at an arbitrary fibril either by modulating the length or the elastic modulus. As a result we introduce an effective fibril compliance term, $\hat{h}_i = h_i\, E/E_i$, where h_i and E_i are the length and elastic modulus of fibril i, and E is the elastic modulus of the backing layer. This parameter can be utilized to investigate the tailoring of fibril length only, for which $\hat{h}_i = h_i$ (i.e. $E_i = E\ \forall i$), and the tailoring of fibril modulus only, for which $\hat{h}_i = h\, E/E_i$ (i.e. $h_i = h\ \forall i$). It should be noted that the practical applicability of the tailoring of fibril length requires careful consideration, as compatibility of the adhesive and contacting surface becomes more complex.

We replace h in (3.8) with the effective fibril compliance, $\hat{h}_i$, and substitute this into (3.24) to obtain

$$\hat{h}_i = \hat{h}_k + a(1-\nu^2)\left[\psi_k - \psi_i + \frac{\pi a^2 E^*}{f_{\max}}(\tilde{x}_i - \tilde{x}_k)\tan\theta_y + \frac{\pi a^2 E^*}{f_{\max}}(\tilde{y}_i - \tilde{y}_k)\tan\theta_x\right], \quad \forall i \tag{3.25}$$

where $\psi_i = \sum_{j=1}^{N} a/r_{ij}$, $\tilde{x}_i = x_i/a$, and $\tilde{y}_i = y_i/a$. This determines the distribution of the effective fibril compliance for an optimal interface. The compliance $\hat{h}_k$ is arbitrary and thus there is, in theory, an infinite number of optimal configurations. It is, however, important to guarantee positivity of $\hat{h}_i$, thus the choice of $\hat{h}_k$ must be consistent with this. For simplicity we

select as $\hat{h}_k$ the average effective fibril compliance $\langle\hat{h}\rangle = \frac{1}{N}\sum_{i=1}^{N}\hat{h}_i$, in light of the fact that (3.25) is linear in all the variables $\tilde{x}_i$, $\tilde{y}_i$, and ψ_i, thus

$$\hat{h}_i = \langle\hat{h}\rangle + a(1-\nu^2)\left[\langle\psi\rangle - \psi_i + \frac{\pi a^2 E^*}{f_{\max}}(\tilde{x}_i - \langle\tilde{x}\rangle)\tan\theta_y + \frac{\pi a^2 E^*}{f_{\max}}(\tilde{y}_i - \langle\tilde{y}\rangle)\tan\theta_x\right], \quad \forall i \tag{3.26}$$

with $\langle\psi\rangle = \frac{1}{N}\sum_{i=1}^{N}\psi_i$, $\langle\tilde{x}\rangle = \frac{1}{N}\sum_{i=1}^{N}\tilde{x}_i$, and $\langle\tilde{y}\rangle = \frac{1}{N}\sum_{i=1}^{N}\tilde{y}_i$.

In the case of a rigid backing layer, the only purpose of fibril compliance optimization is to counteract misalignment. This results in a reduction of (3.26), yielding

$$\hat{h}_i = \langle\hat{h}\rangle + a(1-\nu^2)\left[\frac{\pi a^2 E^*}{f_{\max}}(\tilde{x}_i - \langle\tilde{x}\rangle)\tan\theta_y + \frac{\pi a^2 E^*}{f_{\max}}(\tilde{y}_i - \langle\tilde{y}\rangle)\tan\theta_x\right], \quad \forall i \tag{3.27}$$

Figure 3.13 shows the optimal fibril compliance distribution in the aligned state. The result is independent of the choice of $\pi a^2 E^*/f_{\max}$. We consider the average fibril compliance $\langle\hat{h}\rangle = 5a$, and refer to previous sections for all other parameters. The compliance varies from $\hat{h}_{\min} = 0.50\langle\hat{h}\rangle$ at the array center, to $\hat{h}_{\max} = 1.91\langle\hat{h}\rangle$ at the array corners.

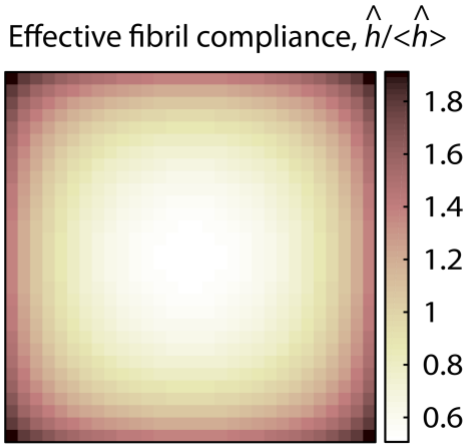

Figure 3.13. Effective fibril compliance distribution, $\hat{h}/\langle\hat{h}\rangle$, for the aligned system. The average effective fibril compliance $\langle\hat{h}\rangle = 5a$, with all other parameter values being equivalent to those in previous sections.

Figure 3.14 examines the normalized detachment force, $F_{\max}/Nf_{\max}$, as a function of the misalignment angle, θ, for three distinct cases: (i) a rigid backing layer, $H = 0$, and homogeneous fibril compliance; (ii) a compliant backing layer, $H = \infty$, and homogeneous fibril compliance; (iii) a compliant backing layer, $H = \infty$, with optimal distribution of fibril compliance given in Figure 3.13. We note that misalignment is typically not deterministic. Although re-optimization could be performed for each case of misalignment to yield the upper bound on adhesive strength of the array, it is of most practical significance to examine the robustness of case (iii) to misalignment.

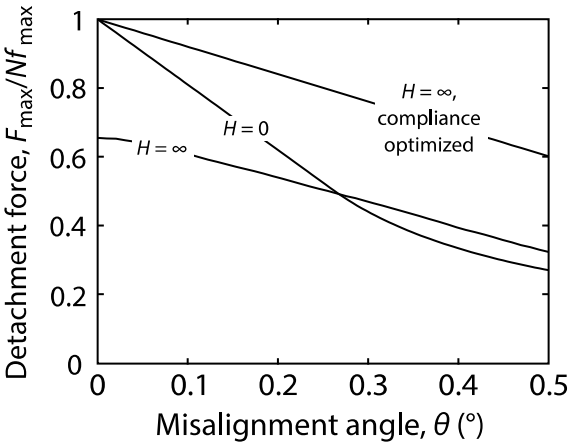

Figure 3.14. Normalized detachment force, $F_{\max}/Nf_{\max}$, versus misalignment angle, θ. Three distinct cases are considered: (i) a rigid backing layer, $H = 0$, and homogeneous fibril compliance; (ii) a compliant backing layer, $H = \infty$, and homogeneous fibril compliance; (iii) a compliant backing layer, $H = \infty$, with the distribution of fibril compliance given in Figure 3.13.

As evidenced by the figure, case (iii) yields the greatest efficiency across the entire range of misalignment examined. That is, despite being optimized in the aligned state, this distribution of fibril compliance exhibits superior performance to the homogenous array with misalignment. Furthermore, the performance of the optimized array is superior to the rigid backing layer. Although not shown, this holds for bidirectional misalignment. Through fibril compliance optimization, we have employed backing layer compliance to operate in a beneficial capacity, facilitating load redistribution to obtain simultaneous detachment without misalignment. Although this redistribution is no longer truly optimal with misalignment, it still provides a tremendous benefit with respect to reducing load concentrations.

3.4 Discussion

In summary, we have considered in the influence of perturbations in the ideal flat-on-flat loading configuration for a model fibrillar microstructured surface. The dominant role of the backing layer compliance controlled array edge load concentration is shown to be altered for even slight interfacial misalignment. Both the backing layer compliance and interfacial misalignment are shown to influence the decay in adhesive strength with increasing array size, motivating a detailed investigation of the associated mechanics.

Increased fibril compliance reduces the severity of load concentrations at the array edge, and due to differential stretching across the array. The examination of fibril spacing reveals backing layer and misalignment dominated regimes, the transition between which is additionally controlled by the misalignment angle and the fibril compliance. The misalignment dominated regime is of particular significance, with backing layer deformation seen to counteract the load concentration which results from misalignment. The compliant backing layer can exhibit improved adhesive strength when compared to the rigid backing layer, suggesting that stiffer and thinner backing layers may not reduce load concentrations among fibrils when interfacial misalignment is present. By tailoring the compliance of individual fibrils, the model system can harness backing layer compliance to provide a uniform load distribution, maximizing adhesive strength. The array optimized for perfect alignment is robust to misalignment, improving adhesive strength when compared to a homogenous array of fibrils on both compliant and rigid backing layers.

We have explored the effect of changes in fibril length and spacing, however their impact on performance must be further contextualized. By increasing fibril length we increase fibril compliance. Load concentration is reduced by compliant fibrils, effectively diminshing backing layer interactions. The result is improved adhesive strength of the array across the entire range of misalignment considered. However, in synthetic adhesives, fibril length is constrained by fabrication techniques as well as by clumping or matting under the action of the attractive interaction among neighboring fibrils [7, 41, 48, 50, 100, 101], often associated with low bending stiffness.

By increasing fibril spacing backing layer interactions are diminished. In the case of perfect alignment, the adhesive strength of the array is improved. On the other hand, the detrimental effect of misalignment is accentuated by increased fibril spacing. An optimal fibril spacing results from the combined effect of backing layer compliance and misalignment. The issue of optimization of fibril spacing is, however, a complex one. Misalignment is not typically deterministic, and therefore designing to the aforementioned criterion requires knowledge of the maximum misalignment and orientation that will be encountered in a given adhesive system. Furthermore, this model considers only the efficiency with which the fibril adhesive strength is realized at the array scale. When the area which can be patterned with adhesive in a given system is fixed, increasing the fibril spacing necessitates a reduction in the total number of fibrils. One must consider whether it is optimal to reduce the fibril density to improve the load distribution, or to increase the fibril density providing additional fibrils to bear adhesive load. As is true for fibril length, clumping or matting also limits fibril density. In any case, the results presented here highlight that a truly universal design criterion for fibril spacing in

synthetic adhesives must consider backing layer compliance and misalignment rather than simply maximizing fibril density to the point of avoiding fibril matting.

The reduction in the adhesive strength with increasing array size highlights the significance of the fibril compliance optimization problem introduced in Section 3.3.5. Fibril compliance can be viewed as diminishing the backing layer interactions by reducing the load concentration which results due to differing degrees of fibril deformation. Here we demonstrate that in theory we can tailor fibril compliance in order to harness the compliance of the backing layer to facilitate optimal load redistribution and obtain maximal adhesive strength. In this model we assume that fibril compliance can be tailored on an ad hoc basis, and without affecting the mechanical properties of the backing layer. Practical implementation of such an array would clearly present many challenges. However, we note that if the elastic modulus were graded such that the perimeter of the array and and backing layer were most compliant, then the load distribution should be improved even when the compliance distribution is sub-optimal. Variation of the elastic modulus as function of depth from the interface has been demonstrated as a viable path to flaw-insensitivity in monolithic adhesive contacts [112]. However, the transverse elastic modulus grading proposed in this work differs in its underlying mechanism. In fact it is exactly analogous to the shape optimization effect explored for a single adhesive contact [113], where the transverse variation of contact profile and elastic modulus are equivalent. Reducing the elastic modulus at the contact edge alleviates the elastic stress concentration and can result in flaw-insensitivity.

Surface roughness of the substrate is not considered in the preceding model system. We expect its influence to be two-fold. At length scales smaller than the characteristic dimension of fibrils, roughness is expected to introduce defects in the fibril tip-substrate contact. This will result in statistical variation of the fibril adhesive strength, $f_{\max}$. Motivated by limited investigations of this effect [45, 107, 109], this is the subject of Chapters 5 and 6. Roughness with larger characteristic length scales is expected to cause statistical variation in the displacement and therefore the load developed in each fibril. While this has been investigated in past work [30, 40, 43, 106], to the author's knowledge the influence of backling layer interactions has not simultaniously been considered.

Chapter 4

Experimental investigation of interfacial misalignment and backing layer compliance

4.1 Introduction

Preceding investigations of the influence of the backing layer on the strength of fibrillar adhesives had suggested that increased compliance is detrimental to the strength of fibril arrays under normal loading due to an increase in the severity of a circumferential load concentration. The results of Chapter 3 suggest that this conclusion may be extremely sensitive to the perturbations in the loading conditions, particularly the alignment of the adhesive patch and substrate. This work of this chapter seeks to experimentally investigate the impact of misalignment on the performance of fibrillar adhesive patches contacting smooth flat surfaces.

4.2 Overview of experiment

Figure 4.1 shows a schematic of the test configuration and micrographs of the adhesive sample. We utilize a synthetic adhesive consisting of array of vertical mushroom-tipped PDMS fibrils on a backing layer of the same material, with the fibril dimensions and array geometry labelled in the figure. The fabrication process is described in ref. [114]. The backing layer compliance

is controlled by preparing the same fibril array with three backing layer thicknesses, $H = 700$ μm, $H = 1700$ μm, and $H = 2700$ μm. The lateral dimensions of the backing layer are much greater than that of the array.

Adhesion tests are performed using a test surface which maintains a fixed angle of misalignment, θ, with respect to the sample surface during approach and retraction. The flat-ended glass cylinder has a radius $R = 2$ mm such that the entire fibril-array may contact the surface. The normal load F and the normal displacement from first contact $\bar{u}$ are recorded. The detachment force $F_{\max}$ is defined as the maximum tensile load attained. The misalignment angle is varied within the range $-1° < \theta < 1°$.

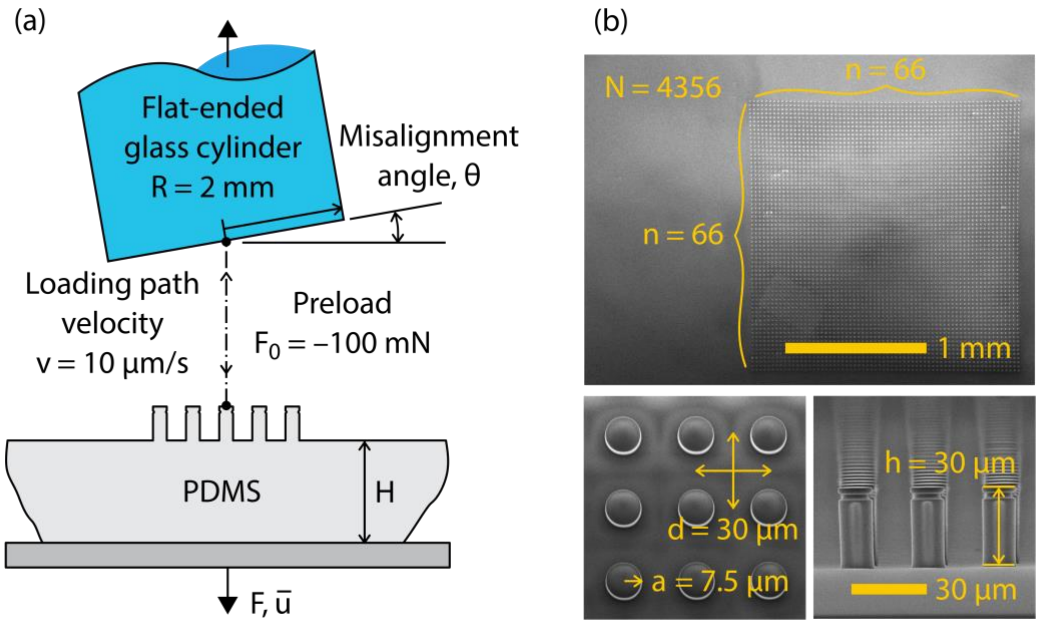

Figure 4.1. (a) Schematic of the experimental set-up for investigation of backing layer compliance and interfacial misalignment. A synthetic adhesive consisting of array of vertical mushroom-tipped PDMS fibrils on a backing layer of the same material, contacts a flat-ended glass cylinder test surface by normal approach and retraction. The approach and retraction velocity $v = 10\ \mu m/s$. Approach is halted and retraction begins when compressive preload $F_0 = -100$ mN is reached. The misalignment angle is varied within the range $-1° < \theta < 1°$. Three backing layer thicknesses are examined, $H = 700\ \mu m$, $H = 1700\ \mu m$, and $H = 2700\ \mu m$; (b) Scanning electron micrographs of the PDMS mushroom-tipped fibril-array. Fibrils are cylindrical with length $h = 30\ \mu m$ and radius $a = 7.5\ \mu m$. Locally the fibrils are arranged in a square packing configuration, with the center-to-center distance $d = 30\ \mu m$. The global array geometry is also square, with the number of fibrils along each axis $n = 66$, yielding a total number of fibrils $N = 4356$.

4.3 Model

We seek to model the attachment and detachment of the synthetic fibrillar adhesive array and test surface, as described in the previous section. The model described in Chapter 3 is adopted, with geometric parameters chosen to match the characteristics of the synthetic adhesive described. All length scales are normalized by the fibril radius such that we prescribe fibril length $h/a = 4$, and the center-to-center distance $d/a = 4$. The number of fibrils along each axis $n_x = n_y = 66$, with the total number of fibrils $N = 4356$. Unidirectional misalignment is considered, with $\theta_x = 0$ and $\theta_y = \theta$. The range of the misalignment angle $-0.8° \leq \theta \leq 0.8°$ is within the limit of (3.14). The preload $F_0/Nf_{\max} = -0.65$ is sufficient to bring all fibrils in to contact at maximum misalignment, $\theta = \pm 0.8°$. The only approximation is associated with the choice of the dimensionless parameter $f_{\max}/\pi a^2 E^*$, related to the strain on a fibril at detachment. It is found that $f_{\max}/\pi a^2 E^* = 0.1$ yields good qualitative agreement to the experimental results. When compared to the parametric study of Chapter 3, an increased emphasis is placed on comparison of results for the rigid backing limit, $H = 0$, and the compliant backing limit, $H = \infty$. All finite thicknesses, including those examined in experiment, are expected to sit between these limits.

4.4 Results and discussion

Figure 4.2 shows the load-displacement characteristics for model system in the aligned state, $\theta = 0°$. For both the rigid and compliant backing layers, the approach involves simultaneous attachment at $\bar{u} = 0$, followed by a linear response in compression. During retraction the rigid backing layer, $H = 0$, exhibits a linear response up to a maximum force $F_{\max}/Nf_{\max} = 1$, at

which point unstable detachment of the entire array occurs and the load drops to zero. This implies that the load distribution is uniform across the array, and the detachment force is the theoretical maximum for the array. For a fixed fibril density, this represents the optimal scaling of the adhesive strength of individual fibrils. For the compliant backing layer, $H = \infty$, the response is initially linear, with the stiffness being lower than in the rigid limit. However, when the load exceeds $F/Nf_{\max} = 0.358$, individual fibril detachment begins, as evidenced by instantaneous drops in the load (inset).

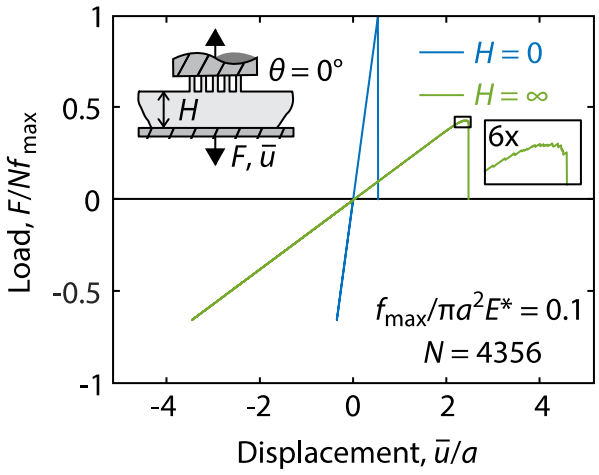

Figure 4.2. Model load-displacement characteristics in the aligned state, $\theta = 0°$. The loading conditions and geometry are described in Section 4.3. Insets show a six-fold magnification of the local detachment of individual fibrils, evidenced by instantaneous drops in the load. The detachment force for $H = 0$ is $F_{\max}/Nf_{\max} = 1$ and for $H = \infty$ is $F_{\max}/Nf_{\max} = 0.432$.

Figure 4.3a shows that for the compliant backing layer, the detachment front propagates circumferentially from the array edge inward (referred to henceforth as circumferential propagation). With this, the adhesive strength of individual fibrils no longer scales to the array

level, and the detachment force $F_{\max}/Nf_{\max} = 0.432$. Figure 4.3b shows that the normal displacement of the compliant backing layer at the array edge lags that at the array center. The strain on fibrils at the array center is only $29\,\%$ of the critical value required for local detachment. This is a consequence of the reduced number of neighboring fibrils locally at the array edge, and the corresponding reduction in the load transmitted locally to the backing layer. Fibrils in this region experience additional stretching, increased load, and eventually detachment as the circumferential defect propagates. This defect propagation is responsible for the $56.8\,\%$ reduction in strength in the limit $H = \infty$ when compared to $H = 0$. This result is in agreement with earlier studies [70, 102] concluding increased backing layer compliance is detrimental to adhesive strength on account of a more severe circumferential load concentration.

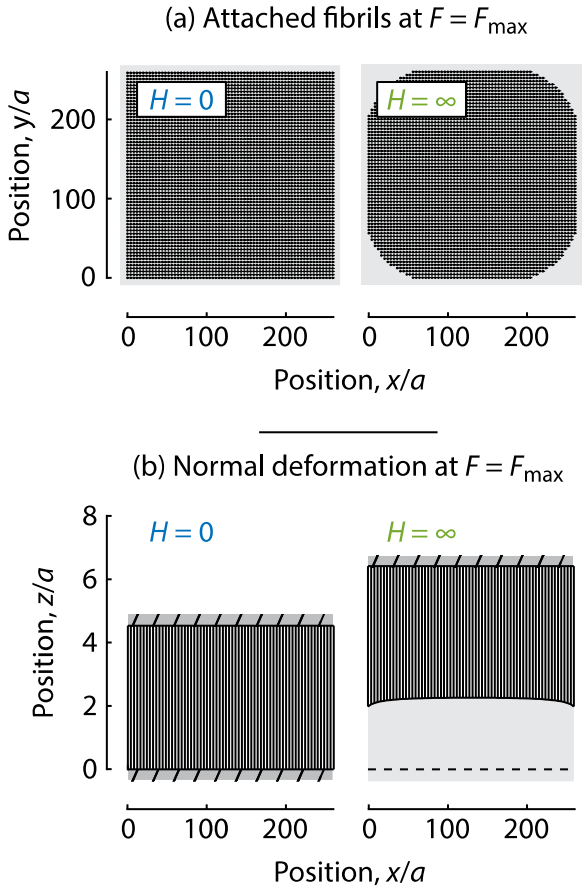

Figure 4.3. Performance of model system in the aligned state, $\theta = 0°$; (a) Attached fibrils at maximum tensile load, $F = F_{max}$; (b) Normal deformation (fibril-array and backing layer) at maximum tensile load, $F = F_{max}$. To visualize the deformation, the z-position is scaled by 40:1 with respect to the x-position.

Figure 4.4 examines the load displacement characteristics for a representative misaligned state, $\theta = 0.4°$. Again, we consider both the rigid backing limit, $H = 0$, and the compliant backing limit, $H = \infty$. First contact occurs at $\bar{u} = 0$ and, for both the rigid and compliant backing layers, the response stiffens as fibrils progressively come in to contact. During retraction the adhesive with a rigid backing layer, $H = 0$,

experiences first detachment prior to the load becoming tensile, $F/Nf_{\max} = -0.013$. As the load becomes tensile, successive detachments continue, with the detachment force $F_{\max}/Nf_{\max} = 0.152$. For the compliant backing layer, $H = \infty$, the onset of first detachment occurs at higher load, $F/Nf_{\max} = 0.120$, and the detachment force is higher, $F_{\max}/Nf_{\max} = 0.192$.

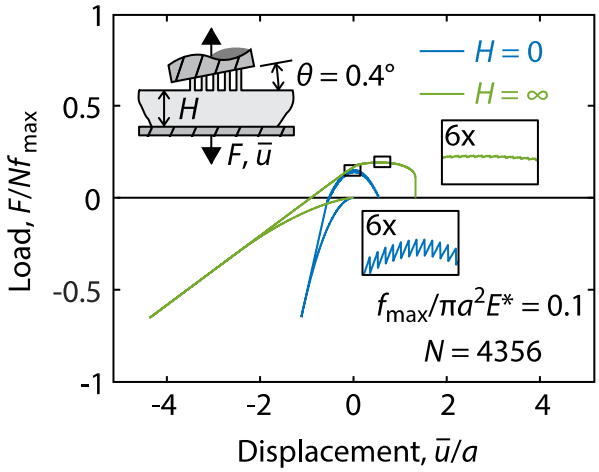

Figure 4.4. Model load-displacement characteristics in a representative misaligned state, $\theta = 0.4°$. The loading conditions and geometry are described in Section 4.3. Insets show a six-fold magnification of the local detachment of individual fibrils, evidenced by instantaneous drops in the load. The detachment force for $H = 0$ is $F_{\max}/Nf_{\max} = 0.152$ and for $H = \infty$ is $F_{\max}/Nf_{\max} = 0.192$.

Figure 4.5a shows that for both the rigid and compliant backing layer, the detachment front is no longer circumferential. It instead propagates from one side of the array to the other (referred to henceforth as peel propagation). For the rigid backing layer, entire rows of fibrils detach simultaneously as they reach their critical load and the detachment front is straight. As a result,

the instantaneous drops in the load are of uniform magnitude throughout peel propagation. For the compliant backing layer, however, the detachment front is curved. This is another manifestation of the effect of reduced numbers of neighboring fibrils locally at the array edge. Drops in the load are of lower magnitude, indicating a smaller number of instantaneous detachments as the curvature of the detachment front changes during peel propagation.

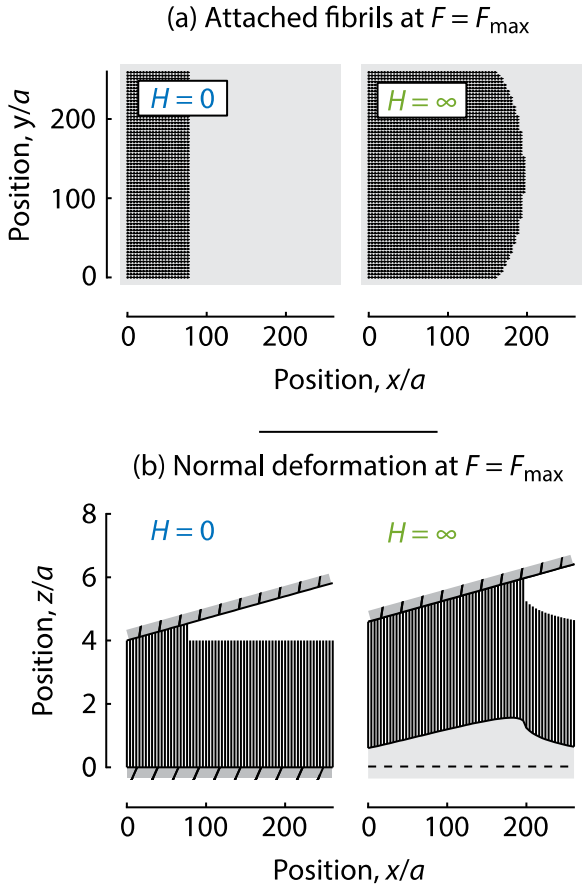

Figure 4.5. Performance of model system in a representative misaligned state, $\theta = 0.4°$; (a) Attached fibrils at maximum tensile load, $F = F_{\max}$; (c) Normal deformation (fibril-array and backing layer) at maximum tensile load, $F = F_{\max}$. To visualize the deformation, the z-position is scaled by 40:1 with respect to the x-position.

Despite similarities in the characteristics of detachment, the strength of the array in peel propagation is greater for the compliant backing layer. Figure 4.5b shows the normal deformation of the array at detachment and reveals the reason for this enhancement in resistance to peel propagation. With load concentrated in fibrils ahead of the detachment front, the backing layer deformation is largest in this region. The effect of this deformation is to reduce the differential stretching of fibrils which occurs in the presence of misalignment. Consequently, the load concentration among fibrils ahead of the detachment front is reduced when compared to the rigid backing layer, leading to an increase in the detachment force. The significance of the backing layer providing resistance to peel propagation will be discussed after experimental results are presented.

Figure 4.6 shows the load-displacement characteristics and attached fibrils in the experimental system for the aligned state, $\theta = 0°$. The load-displacement characteristics reveal that the entire array comes in to contact almost instantaneously at $\bar{u} = 0$, evidenced by the approximately linear response in compression. Increasing the thickness of the backing layer reduces the stiffness of the system, approximated by a linear least-squares fit to the compressive portion of the curve, from $20.8\ \mathrm{N/mm}$ for $H = 700\ \mu\mathrm{m}$ to $8.80\ \mathrm{N/mm}$ for $H = 1700\ \mu\mathrm{m}$, and $6.70\ \mathrm{N/mm}$ for $H = 2700\ \mu\mathrm{m}$. During retraction the load becomes tensile, with a change in the gradient of the load displacement curve indicating the onset of detachment. The load reaches a maximum, $F = F_{\max}$, and ultimately drops to zero upon complete detachment.

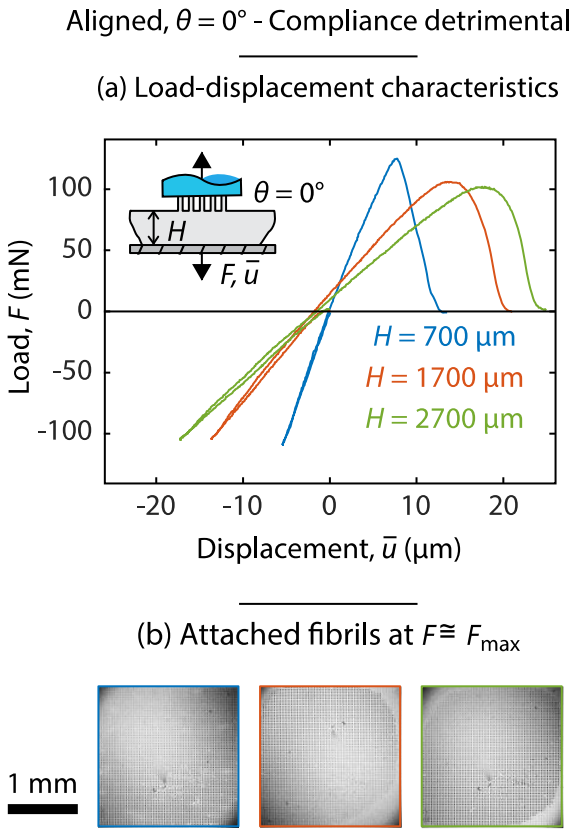

Figure 4.6. Performance of the experimental system in the aligned state, $\theta = 0°$. The loading conditions and geometry of the synthetic adhesive are as described in Section 4.2; (a) Load-displacement characteristics. A representative curve is selected from five repeated measurements. The detachment forces are $F_{\max} = 126 \pm 1$ mN, $F_{\max} = 107 \pm 1$ mN, $F_{\max} = 103 \pm 1$ mN, respectively for $H = 700$ µm, $H = 1700$ µm, and $H = 2700$ µm; (b) Attached fibrils at maximum tensile load, $F \cong F_{\max}$, approximated by comparing the timestamps of the load-cell output to the test-procedure video.

Figure 4.6b demonstrates that detachment occurs via the propagation of a circumferential defect. Full videos of these tests are provided in Supporting Information of ref. [115]. The detachment force decays monotonically with increased backing layer thickness, from $F_{\max} = 126 \pm 1$ mN for $H = 700$ µm to $F_{\max} = 103 \pm 1$ mN for $H = 2700$ µm. This is evidence of

an increasingly severe array edge load concentration for more compliant backing layers. Furthermore, the displacement from first-detachment to full-detachment, crudely approximated by obtaining the timestamps of these events from the test procedure video and multiplying the time increment by the stage velocity, increases from ~ 5 μm for $H = 700$ μm to ~ 15 μm for $H = 2700$ μm. Comparison to the theoretical model, Figure 4.3a, suggests that this is also indicative of a more severe array edge load concentration due to increased backing layer compliance.

Figure 4.7 shows the load-displacement characteristics and attached fibrils in the experimental system for a representative misaligned state, $\theta = 0.4°$. The load-displacement characteristics show that the response stiffens as fibrils progressively come in to contact. During retraction, as the load becomes tensile, first detachment occurs. Figure 4.7b demonstrates that this is associated with the onset of peel propagation. Full videos of these tests are also provided in Supporting Information of ref. [115]. As the detachment front propagates across the array the load is approximately constant and near maximum. Eventually the load drops to zero indicating complete detachment. In contrast to the aligned state, the detachment force now increases monotonically with increased backing layer thickness, from $F_{\max} = 48.3 \pm 0.9$ mN for $H = 700$ μm to $F_{\max} = 68.9 \pm 0.9$ mN for $H = 2700$ μm. This 43 % increase in the adhesive strength corresponds to a 210 % increase in the compliance of the adhesive sample. In addition to providing resistance to peel propagation, the role of backing layer compliance in controlling detachment is further evidenced by the curvature of the detachment front, visible in Figure 4.7b. This curvature becomes more pronounced as the backing layer thickness is increased.

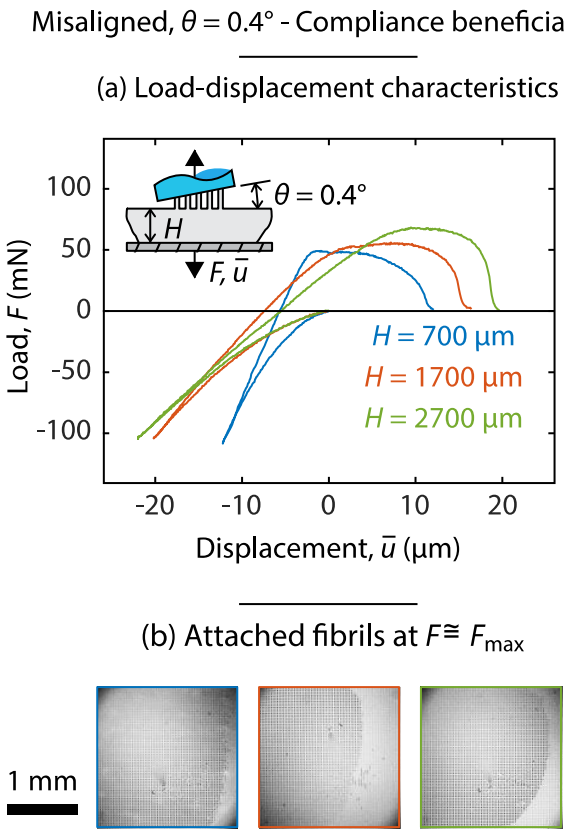

Figure 4.7. Performance of the experimental system in a representative misaligned state, $\theta = 0.4°$. The loading conditions and geometry of the synthetic adhesive are as described in Section 4.2; (a) Load-displacement characteristics. A representative curve is selected from five repeated measurements. The detachment forces are $F_{\max} = 48.3 \pm 0.9$ mN, $F_{\max} = 65.5 \pm 0.6$ mN, $F_{\max} = 68.9 \pm 0.9$ mN respectively for $H = 700$ µm, $H = 1700$ µm, and $H = 2700$ µm; (b) Attached fibrils at maximum tensile load, $F \cong F_{\max}$, approximated by comparing the timestamps of the load-cell output to the test-procedure video.

For both the model and experimental systems we have now identified a detrimental effect of backing layer compliance in the aligned state, and a beneficial effect of backing layer compliance in a representative misaligned state.

Figure 4.8 examines the detachment force as a function of misalignment angle for both (a) the model system, and (b) the experimental system, characterizing the transition between the aforementioned regimes. For the model system, Figure 4.8a, in both limits on backing layer compliance, $H = 0$ and $H = \infty$, the detachment force is maximum in the aligned state, $\theta = 0°$, exhibiting a monotonic decay as the magnitude of the misalignment angle is increased. In the rigid backing layer limit, however, the decay is much more severe than in the compliant backing layer limit. This results in the transition from a compliance detrimental regime to a compliance beneficial regime at a misalignment angle $\theta = 0.173°$ (as approximated by linear interpolation).

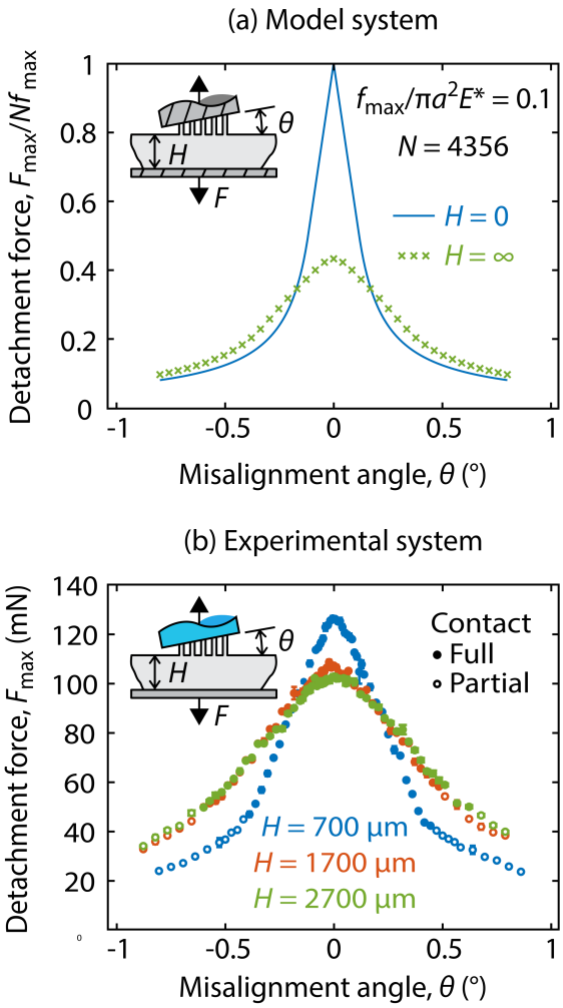

Figure 4.8. Comparison of detachment force vs. misalignment angle for (a) model system, and (b) experimental system. For the model system results are presented in both the rigid backing layer limit, $H = 0$, and the compliant backing layer limit, $H = \infty$, while for the experiment we examine three backing layer thicknesses expected to sit between these limiting cases, $H = 700$ µm, $H = 1700$ µm, and $H = 2700$ µm. For the experimental data, error bars (± one standard deviation from mean of five repeated measurements) are shown. Data points are empty circles where the contact was 'partial' i.e. where misalignment prevented full contact with the array at the specified preload. In the model system, transition between backing layer compliance detrimental and beneficial regimes occurs at $\theta = 0.173°$ (by linear interpolation).

Despite the approximations involved in selecting model parameters associated with strength of individual fibrils, the qualitative similarity to the experimental results is clear, with the transition to a backing layer compliance beneficial regime occurring at $\theta \cong 0.2°$ in experiment. This provides further confidence that the underlying mechanism behind resistance to peel propagation provided by backing layer compliance is indeed deformation at the detachment front, as suggested by the model.

4.5 Discussion

This result highlights that in millimeter-scale bio-inspired fibrillar adhesive patches contacting smooth flat surfaces, normal loading only results in circumferential defect propagation if the alignment of the adhesive and adherend is extremely precise. In the system examined a misalignment angle of just $\theta = 0.4°$, despite not changing the fraction of fibrils in contact with the surface after approach, resulted in a 43 % increase in the detachment force of the thickest backing layer when compared to the thinnest. This enhanced resistance to peel-propagation is the result of backing layer deformation at the detachment front. Differential stretching of fibrils is reduced on account of this deformation, effectively lowering the angle of misalignment and the resulting load concentration. This has implications for the use of fibrillar adhesives applied in normal loading conditions, suggesting that thicker, more compliant backing layers provide an enhanced resistance to peel propagation in the presence of interfacial misalignment.

In regard to this conclusion, it should be noted that to scale adhesive performance to large areas, and to handle complex macroscale curvature of contacting bodies, careful design of

intricate load sharing mechanisms is required [55, 116, 117]. These designs are likely to remain highly application specific, differing significantly depending on the properties of the contacting surface and the specified loading direction. This investigation of the mechanics of misaligned contact under normal loading is only relevant where the millimeter-scale adhesive patch (fibril array and backing layer) is itself held by a stiff surface (e.g. [118]), and is unlikely to provide insight where the backing layer forms a flexible membrane (e.g. [117]).

4.6 Materials and Methods

4.6.1 Microfabrication

The geometry of the fibrillar microstructures was prepared in Inventor CAD software (Autodesk, San Rafael CA, USA). A positive mold was subsequently fabricated in negative photoresist IP-Dip (Nanoscribe, Eggenstein-Leopoldshafen, Germany) by a two-photon polymerization (TPP) system Professional GT (Nanoscribe, Eggenstein-Leopoldshafen, Germany). Surface treatment of fused silica substrates with (3-methacryloyloxypropyl) trichlorosilane was used to promote adhesion of the photoresist. The TPP-device was operated at a constant laser power of 16 mW. After exposure the structures were developed in propylene glycol monomethyl ether acetate (PGMEA) for 20 min at room temperature. The sample was then placed in isopropanol and the photoresist was additionally cross-linked by 365 nm UV exposure for 300 s at 350 mW (OmniCure S1500A, igb-tech, Friedelsheim. Germany) before being dried in air. The IP-Dip positive mold was then treated with (1H,1H,2H,2H-perfluorooctyl) trichlorosilane. Sylgard 184 PDMS (Dow Corning, Midland, MI, USA) was prepared at a 10:1 ratio of base elastomer to curing agent and is mixed and degassed in a

DAC600.2 VAC-P SpeedMixer (Hauschild Engineering, Hamm, Germany) at 2000 rpm for 5 mins. A negative mold was created by pouring the PDMS on to the master structures, degassing, and curing at 95℃ for 60 mins. The negative mold is also treated with (1H,1H,2H,2H- perfluorooctyl) trichlorosilane and the final microstructures are produced by casting the same PDMS mixture in to the negative mold, degassing, and curing at 95℃ for 60 mins. Additional backing layer thickness is added to the sample by casting an unstructured sheet of PDMS following the same curing process as outlined above, before adhering this sheet to the backside of the microstructured sample.

4.6.2 Adhesion measurements

Approach and retraction of the sample is achieved using a motorized stage VP-5ZA and motion controller XPS-C4 (Newport Corporation, Irvine CA, USA). Displacement is monitored by an integrated linear encoder. The glass cylinder test surface, radius 2 mm, is fixed above the sample with the mount allowing for microscope visualization of the contact through the back side of the glass. An attached CCD camera captures video of the attachment and detachment kinematics. Alignment is controlled by two goniometers, GON65-U and GON65-L (Newport Corporation, Irvine CA, USA), located below the adhesive sample. One goniometer is controlled by a micrometer SM-13 (Newport Corporation, Irvine CA, USA) for control of misalignment angle to within $\pm$ 0.003°. The normal load is recorded by a six-axis force and torque sensor Nano17 SI-12-0.12 (ATI Industrial Automation, Apex NC, USA) located below the sample. Hardware interfacing and data acquisition is performed in Labview (National Instruments, Austin TX, USA). The test surface (flat end of glass cylinder) was profiled by

white- light interferometry, Wyko NT1100 Optical Profiling System (Veeco Instruments Inc, Plainview NY, USA). Over the area likely to contact the adhesive the RMS roughness was ~ 70 nm and the maximum height difference was 1.3 μm. Qualitatively, this roughness took the form of small amplitude waves over large areas of the surface.

4.6.3 SEM

The scanning electron micrographs of Figure 4.1 were obtained using a Quanta 250 FEG (FEI, Hillsboro OR, USA) equipped with an Everhart-Thornley detector in high-vacuum mode. The spot size and an accelerating voltage were set to 2.0 and 2 kV, respectively. The specimens were not coated with conductive material. Copper tape was placed on the metallic sample holder to minimize charging effects.

4.6.4 Numerical methods

Data recorded by the custom-built adhesion tester is processed in Matlab (Mathworks, Natick MA, USA). The numerical model is also implemented in Matlab.

Chapter 5

Statistical characterization of fibril adhesive strength

5.1 Introduction

Another feature which emerges as we study adhesive performance at larger length scales is the variability in adhesive strength of individual fibrils. At the interface of the fibril tip and the substrate, we anticipate regions where the separation of the two surfaces exceeds the range of the intermolecular interaction between them. These regions, referred to as cracks or defects, may result from surface roughness, fabrication imperfections, or contaminant particles. The characteristics of the defects may also be dependent on the elastic properties and the preload applied when making contact. Defects are known to be stress raisers, with the severity of the stress concentration being proportional to the lateral extent of the defect. Defects exceeding a critical size will propagate at loads much lower than predicted in the absence of flaws, given the underlying strength of the interaction. For a typical elastomer system adhering by van der Waals forces to a much stiffer substrate, linear elastic fracture mechanics predicts sensitivity of the fibril adhesive strength (applied load on- or elongation of a fibril at detachment) to defects with characteristic dimensions exceeding tens-of-nanometers. Since the characteristic dimensions of typical synthetic fibrils range from several microns to hundreds of microns, it is

anticipated detachment will indeed occur via the propagation of defects at the interface of the fibril tip and substrate. This is supported by various experimental studies (e.g. [59-62]).

Defect propagation is typically localized to the region of the fibril-tip interface where tensile stresses are highest. This is shown schematically for the mushroom tipped fibril in Figure 5.1. Within the high stress region, intense stress magnitudes will be further localized at the tip of individual defects. In combination, these effects yield a dependence on both the defect size and the geometric properties of the fibril. For a compliant fibril adhered to much stiffer substrate, the detachment force has the general form

$$f_c = \beta \left(\frac{EW}{\pi l} \right)^{\frac{1}{2}} \tag{5.1}$$

where E is the elastic modulus of the fibril, W is the work of adhesion, l is the characteristic size of the critical defect, and β is a shape factor which is a function of the geometric properties of the fibril and has units of length squared. For an array of identical fibrils it is expected that one detachment mechanism will dominate, as dictated by the geometry, such that the functional form of β (in addition to the properties E and W) will be unchanged across the array. However, statistical variation in the critical defect size, l, from fibril to fibril in the array is expected as a result of surface roughness, inhomogeneities due to fabrication, or contaminant particles. This will yield a distribution in the adhesive strength of fibrils in the array.

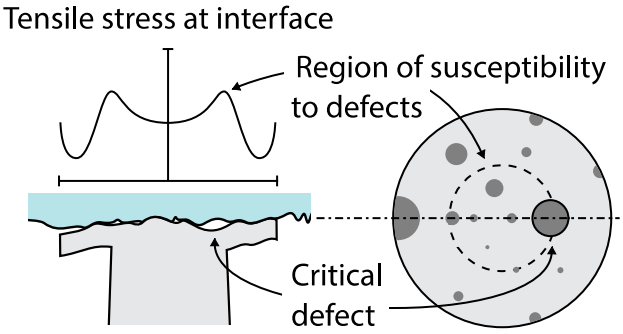

Figure 5.1. Schematic of the effects controlling adhesive strength of an individual mushroom-tipped fibril. The tensile stress distribution shown is hypothesized to arise under the assumption of a perfect contact without roughness. The size of surface asperities and interfacial defects are exaggerated.

For an adhesive patch consisting of an array of fibrillar microstructures, the analysis of the global strength of the contact bears striking similarity to the failure of fibril bundles which have been studied extensively in the context of composite materials. Classical work on this topic showed that, under conditions of equal load sharing, the strength of a bundle decays as the variability in strength of the component fibrils increases [108]. Significant effort in modeling of these systems has since been put forth (as reviewed in ref. [119]), guiding the experimental characterization of the statistical properties of fiber strength (e.g. [120-122]).

An equivalent theoretical approach to the study of fibrillar adhesives was first adopted in by Hui et al. [109], with a theoretical investigation involving Monte Carlo simulations having been performed assuming power law distributed strength across a fibril array. It was confirmed that the strength of the array decayed as the variability in fibril strength increased. It was later hypothesized by McMeeking et al. [45], that defect-dependent detachment of fibrils should follow the statistical theory of fracture [110]. Under the assumption of validity of the empirical

defect density function of Weibull, it was shown that the scaling of adhesive strength with contact perimeter was dependent on the distribution of defect size, potentially reconciling discrepancies across experimental studies [45]. While the role of statistical variation is suggested by these scaling irregularities, it has not been directly verified that the statistical properties of fibril adhesive strength are well described by the Weibull distribution. The work of this chapter seeks to address this by testing the adhesive performance of a fibrillar surface microstructure using a platform which permits in-situ contact visualization, allowing for the determination of the local strength of individual fibril contacts and assessment of the defect character. The results are subject to analysis based on the statistical theory of fracture. Implications for the performance of fibrillar adhesive systems are explored.

5.2 Overview of experiment

Figure 5.2 shows a schematic of the adhesion test performed using an array of mushroom-tipped PDMS fibrils on a backing layer of the same material. Details of the adhesive fabrication process and the experimental platform are given in the Section 5.5. The geometric parameters are given in the figure caption. The adhesive surface and the glass substrate were brought into contact via normal approach, which was halted when the specified compressive preload, P, was reached. They were then separated via normal retraction. The total load, F, and the displacement, u, measured from the position at which $F = 0$, were recorded. In-situ contact visualization was performed, with high contrast between contacting and non-contacting regions obtained by frustrated total internal reflection (FTIR).

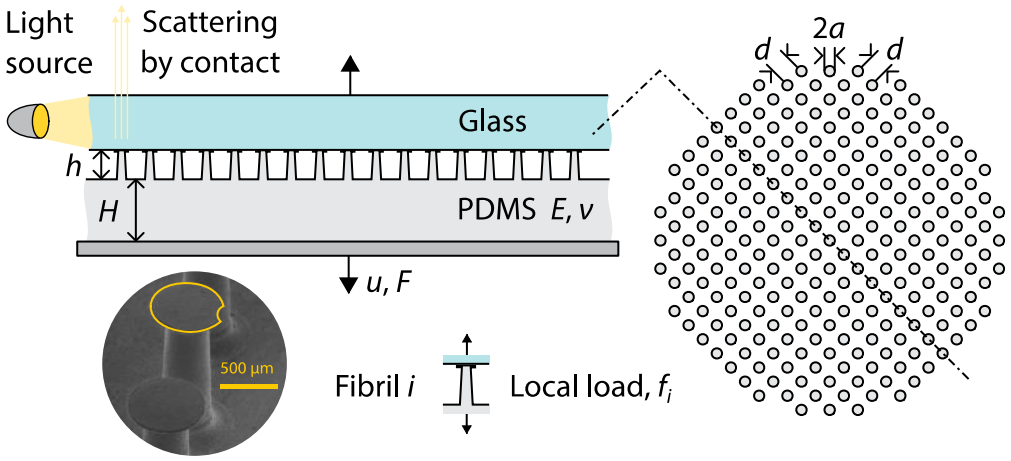

Figure 5.2. Schematic of the adhesion test of an array of mushroom-tipped PDMS fibrils, on a backing layer of the same material, contacting a glass substrate. Fibrils have radius a, and height h. They are arranged in a square packing configuration for which the center-to-center distance is d. The backing layer thickness is H. For the experimental system examined, $a = 200$ µm, $h = 1600$ µm, $d = 800$ µm, and $H = 5000$ µm. SEM of the fibril is also shown, with the mushroom tip outlined to highlight a typical fabrication imperfection. The intended array geometry is exactly as depicted, with $N = 241$, however fibrils lost in fabrication resulted in $N = 237$ [62].

In order to correlate the time of detachment of a fibril from in-situ video with the local load on the fibril at that instant, thus determining the fibril adhesive strength, it is necessary to ensure that load per fibril is uniform across the array. This is achieved when the backing layer is thin, the array dimensions are small, fibrils are compliant and they exhibit high strain at detachment [70]. Load sharing was assessed by ensuring that there is neither a preference for detachment of fibrils close to the array edge, nor any correlation between the detachment of one fibril and subsequent detachment of a neighbor. Verification of a uniform load distribution is detailed in Appendix B. Furthermore, to obtain the adhesive strength of each fibril accurately, the load

cell should be sufficiently stiff so as not to trigger unstable detachment. This is verified by examination of the load-displacement data.

Figure 5.3a shows a plot of the tensile load, F, vs. displacement, u. We observe that as the displacement is increased, separating the surfaces, the load increases. Progressive detachment is evidenced by the reduction in stiffness with increasing load, as well as by in-situ contact visualization shown in the inset. The reduction in stiffness eventually leads to a load maximum, $F_{\max} = 3.92$ N. If the assumption of equal load sharing holds, progressive detachment is evidence of a distribution in the adhesive strength of individual fibrils.

The in-situ contact visualization provides sufficient spatial resolution to determine the character of defect propagation for individual fibrils. We observe two distinct mechanisms of detachment, exemplified in Figure 5.3b. As hypothesized in Figure 5.1, we observe defects nucleating from within the contact, under the edge of the stalk. They propagate outward to the contact edge. These are henceforth referred to as 'center defects'. They account for detachment in 159 of 237 fibrils (67 %). A second mechanism of detachment is also observed, with defects propagating from the perimeter across the contact. These are referred to as 'edge defects'. They account for detachment in the remaining 78 fibrils (33 %).

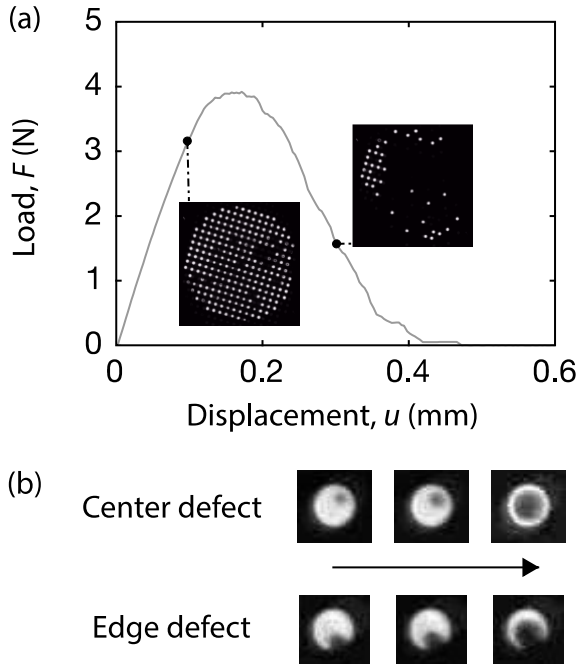

Figure 5.3. (a) Tensile load, F, vs. displacement, u, for the experiment described in Section 5.2. The compressive preload phase, $P = 1$ N, is not shown. Zero displacement is defined at the point of zero load during retraction, such that the fibrils are approximately undeformed. The insets show the contact at two points during retraction, demonstrating progressive detachment of fibrils. (b) Exemplary detachments due to both a *center defect* and an *edge defect*.

Figure 5.4 shows a plot of the detached fibril fraction, N_d/N, vs. displacement, u. Each data point corresponds to the detachment of an individual fibril, as determined by in-situ observation. The displacement for each data point therefore corresponds to the elongation at detachment for that fibril, a convenient measure of the adhesive strength. We seek to combine this data with knowledge of the detachment mechanism, thus giving a more complete picture of the strength distribution.

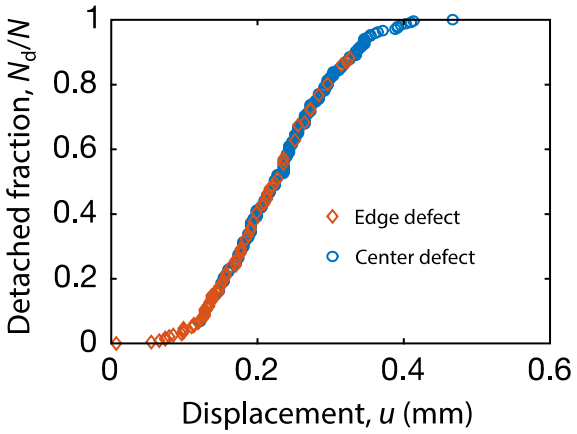

Figure 5.4. Detached fibril fraction, N_d/N, vs. displacement, u. Each data point corresponds to the detachment of an individual fibril. Edge defect detachments and center defect detachments are represented by orange diamonds and blue circles, respectively.

Figure 5.5 shows the histogram of fibril elongation at detachment. The mean $\bar{u}_c = 0.225$ mm, and the standard deviation $\sigma = 0.080$ mm. Determining the statistical properties of each defect population independently is a nuanced problem which is explored in Section 5.3.2. For now, we simply note that the edge defect propagation generally yields lower fibril adhesive strength. Edge defects therefore dominate early in the detachment process.

To summarize, in the majority of fibrils we observe center defect propagation controlled by the characteristic interfacial stress concentration of the mushroom tip geometry. These fibrils operate as anticipated, with the flange having sufficiently reduced strain energy at the contact edge to prevent defect nucleation in this region. However, a significant number of fibrils detach via the propagation of defects from the perimeter across the contact. The adhesive strength for these fibrils is lower than for the fibril-design-controlled center defect detachments. Since very

little strain energy is present in the flange region of the mushroom-tip, the defects causing detachment from the perimeter must be extremely severe. It is hypothesized that they are the result of missing sections of flange, due to unintended damage during demolding. An example of this damage is highlighted in the SEM inset of Figure 5.2. The missing section of flange directly exposes the region at the edge of the stalk, rendering the stress state at the tip of this defect similar to that at the edge of a punch-like fibril [89]. It is therefore unsurprising that the strength of fibrils which detach due to propagation of these defects is greatly reduced when compared to the fundamental mechanism. Given the associated reduction in strength, we anticipate that the existence of this fabrication-imperfection-controlled mechanism is damaging to overall performance. If possible these defects should be eliminated by improving the yield of undamaged flanges in fabrication. With this in mind, as we move to statistically analyze fibril adhesive strength we seek to characterize each distribution independently. If this can be achieved, the properties obtained for the fundamental design-dependent mechanism represent the optimal performance metrics for that specific fibril, substrate, and set of environmental conditions. Furthermore, the properties of the secondary mechanism will allow us to quantify how detrimental it is to overall adhesive performance.

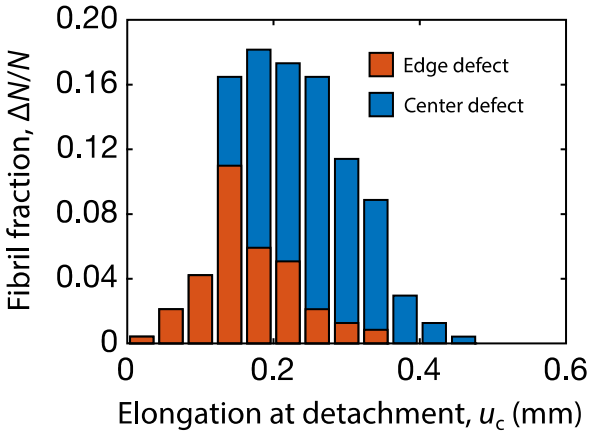

Figure 5.5. Histogram of elongation at detachment, u_c, for the fibril array. The frequency is in the form of the fibril fraction, $\Delta N/N$. The bin size $\Delta u_c = 0.04$ mm.

5.3 Theory and analysis

5.3.1 Unimodal statistical theory

We first consider each defect population independently. For a single population (a single mechanism of detachment) it is assumed that all defects propagate from the same region of the fibril-tip substrate interface, and that this region is symmetric about the fibril center with circumference S. Note that this is equally valid for both defect populations observed in the experiment. For edge defects this region would be the fibril perimeter, while for center defects it would be the axisymmetric region within the contact highlighted by the dashed line in Figure 5.1. The statistical theory of fracture assumes that defects are highly dispersed within these regions. In this case the number of critical defects in non-overlapping sections are independent, the probability of a critical defect existing within a small increment of the region of interest is proportional to its size, dS, and the probability of multiple critical defects existing within this

region is negligible. Known as the Poisson postulates, these are the basis for deriving a governing differential equation for the detachment probability, as detailed in Appendix C. Upon solution of this equation we obtain

$$\phi(f,S) = 1 - \exp\left(-\int_f \int_S g(f,S)\,\mathrm{d}S\mathrm{d}f\right) \tag{5.2}$$

where ϕ is the probability of detachment, f is the local tensile load applied to the fibril, and $g(f,S)$ is the number of defects per unit length of perimeter which yield fibril adhesive strength between f and $f + \mathrm{d}f$. The functional dependence of g on S accounts for the possibility of a non-uniform stress state along the high-stress region. In the system examined the contact is axisymmetric and thus the stress state does not vary along the perimeter. The probability of detachment becomes

$$\phi(f,S) = 1 - \exp\left(-S\int_f g(f)\mathrm{d}f\right) \tag{5.3}$$

The function $g(f)$ is representative of the distribution of size of the critical defect (from fibril to fibril) through its dependence on the load. If the relationship between detachment load and defect size can be deduced from fracture mechanics, i.e. if the parameters in (5.1) are known, then it is possible to obtain this distribution directly from the functional form of $g(f)$.

Having obtained the fundamental law of the statistical theory of fracture, the relevant task becomes characterizing $g(f)$ for a given material system. The most common approach has

been to assume an empirical form and test its suitability by fitting to experimental data. On account of its simplicity and versatility, a power law form of $g(f)$ was proposed by Weibull [110]

$$g(f) = \frac{m}{S_0 f_0}\left(\frac{f}{f_0}\right)^{m-1} \tag{5.4}$$

where S_0 is the reference fibril contact perimeter, f_0 is the reference value for the fibril adhesive strength, and m is the Weibull modulus. This yields the detachment probability

$$\phi = 1 - \exp\left[-\frac{S}{S_0}\left(\frac{f}{f_0}\right)^m\right] \tag{5.5}$$

The dependence on S yields a monotonic increase in the detachment probability with increasing fibril dimensions (assuming self-similar scaling). This is reflective of the increased likelihood of encountering a critical defect as the size of the high-stress region is increased. Moving forward we will consider only an array of identical fibrils, for which $S = S_0$ and the detachment probability simplifies to

$$\phi = 1 - \exp\left[-\left(\frac{f}{f_0}\right)^m\right] \tag{5.6}$$

At this point it is convenient to note the equivalence of the local tensile load, f, and the displacement/elongation, u, in describing the adhesive strength of a fibril. The critical force

identified in (5.1) could be alternatively stated in terms of the elongation at detachment by recognizing that

$$u_c = f_c/k \tag{5.7}$$

where k is the axial stiffness of a fibril. The detachment probability can therefore be written as

$$\phi = 1 - \exp\left[-\left(\frac{u}{u_0}\right)^m\right] \tag{5.8}$$

where u_0 is the reference value for the elongation at detachment. Since elongation at detachment is the most experimentally convenient measure of fibril adhesive strength, we proceed with this definition. We use the term fibril adhesive strength in referring to either the maximum tensile load supported by an individual fibril, or the elongation of the fibril at detachment.

The parameters u_0 and m are reflective of the statistical properties of the fibril strength for a particular substrate and set of environmental conditions. The reference strength, u_0, is related to the arithmetic mean, $\bar{u}_c$, via

$$\bar{u}_c = u_0\,\Gamma\left(\frac{1}{m} + 1\right) \tag{5.9}$$

where Γ is the gamma function. Over the entire physical range of m, the value of Γ varies between 0.88 and 1, meaning that u_0 can be viewed as primarily representative of the average fibril adhesive strength (and therefore dependent upon the average interfacial defect size). The Weibull modulus is a measure of the variability in this strength, with $m = 1$ representing the stochastic limit, and $m = \infty$ representing the deterministic limit in which the strength is uniquely u_0. The Weibull modulus is related to the standard deviation, σ, as

$$\sigma = u_0 \left[\Gamma\left(\frac{2}{m} + 1\right) - \Gamma\left(\frac{1}{m} + 1\right)^2 \right]^{\frac{1}{2}} \tag{5.10}$$

This is a monotonically decreasing function which in the limit $m = 1$ yields $\sigma = u_0$, and in the limit $m = \infty$ yields $\sigma = 0$. We observe that in an absolute sense, the standard deviation is also dependent on the reference strength u_0. The probability density distribution for strength is given by

$$\psi = m \left(\frac{u_c}{u_0}\right)^{m-1} \exp\left[-\left(\frac{u_c}{u_0}\right)^m \right] \tag{5.11}$$

The typical approach in the study of fracture is to test many samples independently, assign a probability to each based on ranking the strength observed. For the purpose of characterization, conditions of equal load sharing dictate that the experiment described in Section 5.2 effectively obtains the adhesive strength data for N fibrils simultaneously. The detached fibril fraction, N_d/N, is exactly the normalized rank in strength from lowest to highest, and is therefore equivalent to the detachment probability

$$\phi = \frac{N_{\mathrm{d}}}{N} \tag{5.12}$$

and, for a single defect population, (5.8) can be fit to these experimental data. If the assumed functional form of the defect density distribution is appropriate, leading to a good fit, then the Weibull statistical properties u_0 and m are obtained.

5.3.2 Bimodal statistical theory

If two defect populations exist concurrently at the interface of the fibril tip and substrate then the situation is complicated significantly. Consider that a fibril detaching due to an edge defect, necessarily contains a center defect which would have resulted in higher adhesive strength. The information about this defect is lost, and the emerging statistical properties of the center defect distribution are distorted.

One possible approach to this problem is to develop a statistical framework which accounts for the possibility of multiple defect populations. Consider that the probability of detachment must be the product of the probabilities of detachment due to each population individually. If the first population exists for all fibrils, while the secondary population exists only among a fraction of all fibrils, α, (known as partial concurrency [123]) then this is given by

$$\phi = 1 - (1-\alpha)\exp\left[-\left(\frac{u}{u_{01}}\right)^{m_1}\right] - \alpha\exp\left[-\left(\frac{u}{u_{01}}\right)^{m_1} - \left(\frac{u}{u_{02}}\right)^{m_2}\right] \tag{5.13}$$

where u_{0i} and m_i are the statistical properties of individual populations. Note that in the limit $\alpha = 0$ we obtain the result for a single population, while in the limit $\alpha = 1$ we have full concurrency of the two populations among all fibrils. The issue is that in this form, absent additional information, (5.13) lacks utility for fitting to experimental data. The parameter space is extremely large and the probability itself is not unique for all combinations of parameters.

The other approach, afforded by knowledge of the detachment mechanism on a fibril-by-fibril basis, is to try to decouple the populations and use the unimodal framework of Section 5.3.1 to characterize their statistical properties individually. The simplest approach is to isolate the center defects and re-rank them within the interval $[1, N]$, relaxing the constraint on integer ranking and evenly spacing the data points. However, this approach neglects the influence of coupling of the populations. An improved method is mean order ranking [124], which considers the position of edge defects within the sequence. The more edge defects which are encountered, the lower the rank assigned to the next center defect relative to the simple reranking approach. This reflects the increased probability that the disguised center defect strengths would have exceeded subsequent data in the sequence. Mathematically this is achieved by considering each data point in the sequence in order. When an edge defect is encountered in the sequence, the increment in the rank for the next center defect is recalculated as

$$\Delta = \frac{N + 1 - j}{1 + (N - i)} \tag{5.14}$$

where j is the re-rank of the previous center defect in the sequence. Upon re-ranking, the associated detachment probability is calculated as

$$\phi = \frac{j}{N} \tag{5.15}$$

Figure 5.6 shows the detachment probability, ϕ, vs. displacement, u for both the mean order ranked center defect data, and the original bimodal data. The shift in center defect data achieved for both simple reranking (not shown) and mean order reranking, reflects the higher strength of center defects. However, mean order reranking accounts for the dominance of edge defects at low displacement by reducing the detachment probability in this region, relative to simple reranking. With the mean order rank of center defect detachments, we are able to fit the unimodal statistical framework of (5.8). A non-linear least squares fitting method is preferred, as described in Appendix D. This yields a reference strength $u_0 = 0.285$ mm and Weibull modulus $m = 4.08$. The corresponding average elongation at detachment, obtained from (5.9), is $\bar{u}_c = 0.259$ mm. The standard deviation, obtained from (5.10), is $\sigma = 0.091$ mm.

If the experimental platform is not able to determine the defect character for each fibril, the data has to be treated as if only one defect family controls the adhesive strength. The raw experimental data would then be fitted to a single Weibull model. While this does yield a reasonable fit, the extracted statistical parameters (given in the caption of Figure 5.6) do not accurately characterize either defect population. They represent an underestimation of the reference strength and Weibull modulus of the fundamental detachment mechanism by 12 %

and 25 %, respectively. Furthermore, this mischaracterization, on account of a failure to recognize bimodality, would lead to a loss of insight when considering the performance of fibrillar microstructured samples. This will be discussed in detail in Section 5.4.

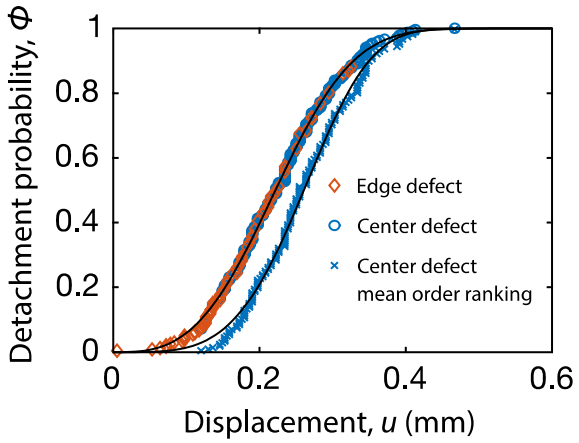

Figure 5.6. Detachment probability, ϕ, vs. displacement, u. Raw experimental data, containing both edge defect detachments (orange diamonds) and center defect detachments (blue circles), is shown alongside mean order ranked data for center defects (blue crosses). Results of fitting (5.8) to each data set are shown as solid lines. For the mean order ranked data the associated parameters are $u_0 = 0.285$ mm and $m = 4.08$. The root mean square error of the fit is $\Sigma = 0.036$. For the raw data the associated parameters are $u_0 = 0.250$ mm and $m = 3.05$. The root mean square error for the fit is $\Sigma = 0.020$.

For now, we seek to characterize the statistical properties of the edge defect population. Mean order ranking could be applied to this population, but this would assume that edge defects exist in all fibrils. Given the hypothesis that edge defects are primarily associated with damaged mushroom tips, this is unlikely. Accordingly, we adopt an alternative approach. As we now have an estimate of the statistical properties of the center defect population, the parameter

space of (5.13) can be greatly reduced. With u_{01} and m_1 taken from the preceding analysis, we perform a non-linear least squares fit of this equation to the raw experimental data to obtain the three remaining unknown parameters, u_{02}, m_2, and α, all associated with the edge defect population.

Figure 5.7 shows the fit when mean order ranked statistical properties of the center defect population are combined with the bimodal framework of (5.13). We prescribe $u_{01} = 0.285$ mm and $m_1 = 4.08$, and obtain the statistical properties of the edge defect population as $u_{02} = 0.201$ mm and $m_2 = 3.35$. The fraction of fibrils exhibiting the edge defect population is determined to be $\alpha = 0.390$ or 39 %. This is physically meaningful, given that 33 % of detachments were due to edge defects in the experiment. It is expected that this value should be less than α given that some fibrils with edge defects will still detach due to large, and therefore critical, center defects. In Figure 5.7 we also show the probability functions associated with each population individually (dashed curves), to highlight the limits between which the coupled behavior lies.

Given the large parameter space of the bimodal framework, we seek to confirm the validity of the statistical parameters obtained. To this end we perform a Monte Carlo simulation which takes as its input the statistical parameters u_{01}, m_1, u_{02}, m_2, and α, and generates a discrete bimodal distribution in which the statistical origins of each data point can be identified. This permits the generation of a histogram of fibril adhesive strength, decomposed by defect type. Differences in these histograms are observed, even where combinations of parameters lead to very similar attachment probability distributions. This is described in detail in Appendix E.

Histograms generated are compared qualitatively to the experimental result of Figure 5.5. Excellent agreement is observed for the parameters obtained by combining the method of mean order ranking of the primary population with non-linear least squares fitting of the bimodal framework for the secondary population. This gives confidence that each defect distribution independently has been well characterized.

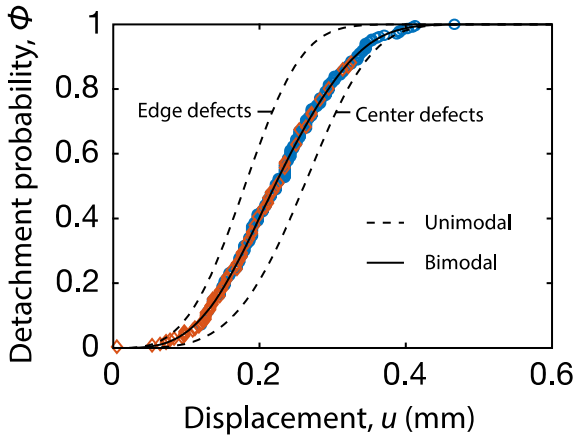

Figure 5.7. Detachment probability, ϕ, vs. displacement, u, showing the resulting fit when combining the statistical properties of center defects obtained by mean order ranking, $u_{01} = 0.285$ mm and $m_1 = 4.08$, with the bimodal detachment probability of (5.13). The three unspecified parameters obtained by fitting are $u_{02} = 0.201$ mm, $m_2 = 3.35$, and $\alpha = 0.390$. The root mean square error for the fit is $\Sigma = 0.020$. The associated unimodal detachment probabilities are shown for each defect population.

5.3.3 Performance of fibril arrays exhibiting Weibull distributed strength

Fibril adhesive strength, in the form of elongation at detachment, appears to be well described by Weibull's statistical theory of fracture. We therefore seek to examine the influence of this

statistical variation on the adhesive performance of a fibrillar microstructured surface. For the fibrillar array (shown in Figure 5.2), the load developed during contact

$$F = \sum_{i=1}^{N_\mathrm{a}} f_i \tag{5.16}$$

where N_a is the number of attached fibrils and f_i is the local load experienced by fibril i. Under conditions of equal load sharing, the total load is

$$F = N_\mathrm{a} f \tag{5.17}$$

where f is the local load experienced by all attached fibrils. This can be stated in terms of the displacement as

$$F = N_\mathrm{a} k u \tag{5.18}$$

The probability of individual fibril detachment is equivalent to the fraction of fibrils within the array which have detached, yielding

$$N_\mathrm{a} = N - N_\mathrm{d} = (1 - \phi) N \tag{5.19}$$

For an array exhibiting two partially concurrent defect populations, the load is given by

$$F = Nku\left[(1-\alpha)\exp\left(-\left(\frac{u}{u_{01}}\right)^{m_1}\right)+\alpha\exp\left(-\left(\frac{u}{u_{01}}\right)^{m_1}-\left(\frac{u}{u_{02}}\right)^{m_2}\right)\right] \tag{5.20}$$

In the limit of a single population, $\alpha = 0$, an analytical expression for the maximum load can be obtained by determining the point of zero gradient, as

$$u|_{\frac{dF}{du}=0} = u_0\left(\frac{1}{m}\right)^{\frac{1}{m}} \tag{5.21}$$

yielding

$$F_{\max} = Nku_0\left(\frac{1}{m}\right)^{\frac{1}{m}}\exp\left(-\frac{1}{m}\right) \tag{5.22}$$

which is an upper bound on the adhesive strength of a fibril array exhibiting the statistical parameters u_0, and m. As expected, increase in the average fibril adhesive strength, or equivalently reduction in the average defect size, results in increase of the array adhesive strength. Of equal significance in determining the array strength is the variability in strength or defect size, as reflected by the dependence on m. Terms in m yield a reduction in the strength by a factor of 0.368 in the stochastic limit, $m = 1$, as compared to the deterministic limit, $m = \infty$. This is a consequence of weak fibrils in the distribution, which cannot be compensated for by fibrils with higher than average adhesive strength. Early detachments are more damaging as they increase the share of load on fibrils which remain in contact and lead to a load maximum at lower displacement.

The preceding results allow for the assessment of the influence of the weaker edge defect population on the performance of the fibril array tested. We obtain the stiffness of the fibril array from the experimental load-displacement data as $Nk = 41.6\ \mathrm{N\ mm^{-1}}$. In combination with the statistical parameters of the fundamental mechanism, $u_0 = 0.285$ mm and $m = 4.08$ (i.e. obtained from center defect mean order ranking), (5.22) provides an estimate of the upper bound on load, $F_{\max} = 6.58$ N. The maximum load observed in experiment was just $F_{\max} = 3.92$ N, suggesting that the impact of the edge defect population is a reduction in the adhesive strength of the fibril array on the order of 40 %. This is close to the percentage of fibrils which possess these fabrication imperfections, and highlights the adhesive strength which may be gained by improving the yield of undamaged fibril tips.

5.4 Discussion

Eq. (5.22) demonstrates that the variability in local adhesive strength from fibril to fibril can play an important role in determining the global adhesive strength of a microstructured sample. This emphasizes the significance of characterizing the statistical properties of fibril adhesive strength in a systematic way. By in-situ observation of the contact we have demonstrated that it is possible to determine elongation at detachment on a fibril-by-fibril basis across the array. In addition to observing defect propagation from within the contact below the stalk edge, defect propagation was also observed at the contact edge. This extraneous detachment mechanism is most likely associated with mushroom tips damaged during fabrication. While the statistical theory of fracture suggests a framework for characterization of the statistical properties of fibril adhesive strength, the coupling of these two defect populations complicates this process.

Detachments due to one mechanism disguise statistical information about the other. The expectation that edge defects exist among only a fraction of all fibrils further increases the parameter space. These challenges are addressed by first decoupling the statistical properties of the fundamental center defect population, before combining the statistical properties which emerge from this method with a bimodal probability framework. On the basis of this analysis it is observed that, individually, the populations appear to be well characterized by the defect density function of Weibull. The capability of the model to predict an upper bound on array adhesive strength subsequently proved useful in determining the influence of the secondary, fabrication-dependent mechanism. We observe that the percentage reduction in strength is of the same order as the percentage of fibrils with fabrication imperfections, approximately 40 %, and thus large increases in strength may be possible by increasing the yield of undamaged mushroom tips. It is anticipated that when making improvements to the fabrication process, repetition of this statistical analysis would be a valuable tool in the assessment of progress.

In considering how the results may change for different fibril geometries, we return to the discussion of Section 1 and the fibril adhesive strength given in (5.1). It is noted that each defect type will be associated with a different form of the shape factor β. For edge defects, as compared to center defects, it is expected that this will lead to lower strength for the same characteristic defect size. Unfortunately, to the authors knowledge, no analysis of these specific defect types has been performed. Analyses of mushroom tipped fibrils have typically focused on comparison to punch-like fibrils for defects at the contact edge (e.g. [64]), and have not analyzed the strength due to defects within the contact. Consequently, exact solutions for the shape factors as a function of geometric features (fibril length, stalk diameter, flange diameter,

flange thickness) are not available. Intuitively we expect that for center defects nucleating below where the stalk meets the flange, reduction in the thickness or reduction of the diameter of the flange will give lower fibril adhesive strength. Increase in the diameter of the stalk should also lead to lower strength for both center defects and for edge defects associated with missing sections of flange. These effects are expected to change the average strength, with limited impact on the defect size distribution and thus the statistical variation in fibril adhesive strength. The dependence of the adhesive strength of a fibrillar sub-contact on the fibril length is expected to be weak, although fibril length can play an important role on system performance in other ways, for example governing the contributing to the toughness at large length scales [40, 46, 49, 50] or controlling the tendency for fibril mating [7, 41, 48, 50, 100, 101].

Changes in the stalk diameter have further significance in that, unlike other geometric properties discussed, they are expected to directly influence the statistical aspects of failure for the center defect population. Increasing the stalk diameter increases the extent of the high stress region highlighted in Figure 5.1. The probability of sampling a critical defect thus increases, as is reflected in (5.5). One option for comparison of fibrils with different stalk diameters is to use (5.6), which contains no explicit size effect, for fitting purposes. In this case the changes in geometry will be reflected implicitly in the values of f_0 and m obtained. Alternatively, (5.5) can be utilized directly to verify that the scaling of strength with stalk diameter is as predicted by this statistical framework.

The study of fibrils with reduced characteristic dimensions is an important technical challenge to be addressed in future work, and will require consideration of both the resolution of in-situ

visualization capabilities and the ability to maintain equal load sharing conditions. In regard to the latter, backing layer effects are expected to become more pronounced as the fibril length is reduced, and as the array size is increased [70]. Contact height differences due to inhomogeneities in the backing layer or roughness at the fibril scale [40, 106, 109], as well as loading imperfections [115, 125], will become more pronounced with respect to the fibril length. Statistical models may therefore have to account for non-equal load sharing, as has been required in the study of the failure of fibers in composite materials [126].

5.5 Materials and methods

The microstructured sample was made from polydimethylsiloxane (PDMS, Sylgard 184, Dow Corning, Midland, MI, USA) via replica molding as described in detail in ref. [62]. Briefly, for replica molding, an aluminum mold with milled microscopic holes (negative of the mushroom structure) was used as template. The bottom of the mold was sealed using a polyethylene terephthalate (PET) film, Sigma (SIG GmbH, Düsseldorf, Germany). The surface roughness of the PET film was transferred to tips of the mushroom shaped microstructures. This has been characterized by atomic force microscopy and is determined to have a Hurst exponent close to unity, and a roll of wave number of $2.5\ \mu m^{-1}$. Qualitatively the roughness is on the scale of tens of nanometers, with an RMS height difference of $37\ nm$ and an RMS gradient of 35.

Adhesion tests were performed with a tensile tester (Inspekt table BLUE, Hegewald & Peschke, Nossen, Germany) equipped with a $50\ N$ load cell. We corrected the measured displacement by accounting for the machine compliance of $7.43\ \mu m/N$. The tensile tester was modified to perform adhesion tests on a smooth and nominally flat glass substrate. A θ-ϕ-

goniometer (MOGO, Owis, Staufen im Breisgau, Germany) was utilized in order to align the substrate with the microstructured sample. A mirror and a camera were mounted below the transparent glass substrate. The contact of each pillar with the substrate was visualized in situ by the principle of frustrated total internal reflection, as described in detail in ref. [62]. Videos of contact formation and detachment were recorded and, subsequently, correlated with force and displacement data.

In the adhesion measurements, specimen and substrate were brought together until a compressive preload, $P = 1$ N was reached. The velocity of approach and retraction was $v = 1\,\mathrm{mm/min}$. After reaching the compressive preload, the specimen was immediately withdrawn until it detached from the substrate. Measurements were performed using one adhesive specimen, repeated at three different positions on the substrate. There were no significant differences between the tests, hence a representative result is shown.

Force-displacement data was correlated with image sequences as follows. Image sequences were binarized by threshold using Fiji [127] such that contact (white) and non-contact (black) areas of mushroom pillars were identified. The position of each contact, together with the time of attachment and detachment, were determined using the 'Analyze Particle' tool in Fiji. Position and time data were imported into a MATLAB routine (MathWorks, MA, USA) and correlated with force, time and displacement data from the adhesion test. For synchronization, the image showing the detachment of the last pillar was attributed to the time when the tensile force relaxed to zero. Crack types were determined manually for each fibril in the array.

Chapter 6

Modeling the effect of non-uniform load distribution and statistical variation in fibril adhesive strength

6.1 Introduction

It is well known that synthetic fibrils designed for dry adhesion undergo defect-controlled detachment. In Chapter 5 it was demonstrated that the statistical distribution of strength among fibrils in an array, which results due to differences in defect size, was well characterized by Weibull's statistical theory of fracture. A requirement of the experimental characterization of strength on a fibril-by-fibril basis was assurance of a uniform load distribution among fibrils. However, in many situations of relevance to both experimental characterization and real-world application, geometric and material features of the system at length scales on the order of the fibril array size give rise to load concentrations among a subset of fibrils. These result in distinct modes of detachment of the fibril array, and lead to changes in the adhesive strength observed at the array scale. Examples of this include backing layer compliance and misalignment between the sample and substrate (which were the subject of Chapters 3 and 4) as well as substrate curvature. This chapter seeks to explore the coupling of variability in the

strength of fibrillar sub-contacts to large scale adhesive performance, examining the influence on the modes of detachment at the array scale and the resulting adhesive strength.

6.2 Theory

6.2.1 Overview

In this theoretical investigation we choose to examine two effects, backing layer compliance and curvature of the substrate. These are arguably the most ubiquitous sources of non-uniform load distribution, with relevance to both experimental characterization and practical application. Substrate curvature, as considered, is a purely geometric effect which gives rise to an array edge load concentration. Backing layer compliance, which can be controlled by both the geometry (i.e. the thickness) and the elastic properties of the component material, also gives rise to an array edge load concentration.

Figure 6.1 is a schematic representation of the contact of the fibrillar adhesive array and rigid substrate. The surface microstructures are assumed to be cylindrical, with radius a and height h. While the schematic shows mushroom-tipped fibrils, the tip is assumed to have negligible influence on the elastic response and thus the tip shape need not be evoked in the analysis which follows. Fibrils are arranged in a regular hexagonal array, with local hexagonal packing. The fibril spacing is d, and the array dimension is described by the length of the edge, D. The total number of fibrils is therefore

$$N = \frac{3D}{d}\left(1 + \frac{D}{d}\right) + 1 \tag{6.1}$$

The fibrils sit on a backing layer, which has thickness H and is itself backed by a rigid tile. The backing layer is composed of the same material as the fibrils, with Young's modulus, E, and Poisson ratio, ν. The substrate is assumed to possess idealized curvature, with radius R.

Fibrils in contact develop axial load, f_i, with the total load being

$$F = \sum_{i=1}^{N} f_i \tag{6.2}$$

The tip displacement of a fibril in contact is dependent on the curvature of the substrate and the applied displacement, $\bar{u}$, according to

$$u_i = \bar{u} + \frac{{x_i}^2}{2R} + \frac{{y_i}^2}{2R} \tag{6.3}$$

where a series expansion in the radial distance from the apex, $r_i = \sqrt{{x_i}^2 + {y_i}^2}$, is utilized. Higher order terms are neglected on the basis that the ratio of the maximum radial position to the radius of curvature, D/R, is small.

The relationship between tip displacement and axial load is dependent on both the fibril compliance and the compliance of the backing layer. In general it may be written that

$$u_i = c_{ij} f_j \tag{6.4}$$

where the terms of the compliance matrix were given in (3.7) and (3.8) for the limits of a rigid backing layer and fully compliant backing layer, respectively.

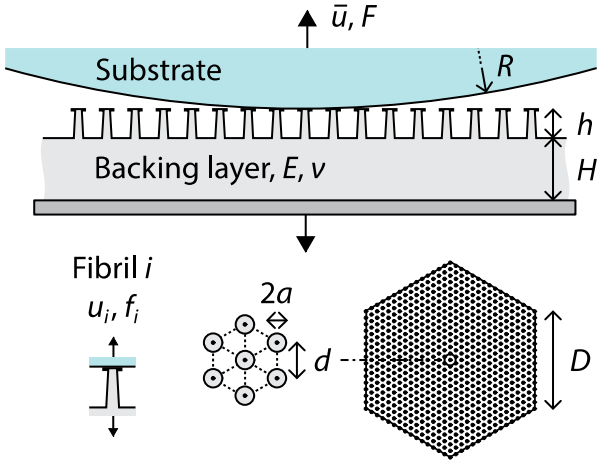

Figure 6.1. Schematic of the adhesive contact of an array of fibrillar microstructures with a curved rigid substrate. The fibril array is on a backing layer of the same material, with Young's modulus, E, and Poisson ratio, ν. Each fibril has radius a, and undeformed length h. Fibrils are arranged in a hexagonal array, with characteristic fibril spacing d. The array size is described by the length D, with the total number of fibrils being N. The force, F, generates a relative displacement of the substrate, $\bar{u}$, which is zero when the fibril at the array center is unstretched.

It is assumed that a single design-controlled mode of detachment dominates. It was shown in Chapter 5 that severe fabrication imperfections can lead to the concurrent observation of an extraneous secondary detachment mechanism within a fibril array. While this complicates the

characterization of the statistical properties of fibril performance, it is not expected to result in significantly different qualitative behavior with respect to the coupling of the array scale load distribution and statistical variation in fibril adhesive strength, which are the subject of this work.

For a single defect population which is well-characterized by Weibull's statistical theory of fracture, the probability of detachment of fibril i is

$$\phi_i = 1 - \exp\left[-\left(\frac{f_i}{f_0}\right)^m\right] \quad \forall i \tag{6.5}$$

where f_0 is the reference value for the fibril adhesive strength and m is the Weibull modulus. For an array of N fibrils it is known that the detachment probability is equivalent to the normalized rank in strength

$$\phi_i = \frac{i}{N} \quad \forall i \tag{6.6}$$

Combining (6.5) and (6.6) we can solve for the discrete fibril adhesive strengths in the array as

$$f_{\max}^i = f_0\left[-\ln\left(1 - \frac{i}{N}\right)\right]^{\frac{1}{m}} \quad \forall i \tag{6.7}$$

The mean strength is given by

$$\bar{f}_{\max} = f_0 \, \Gamma\left(\frac{1}{m} + 1\right) \tag{6.8}$$

where Γ is the gamma function. The standard deviation is

$$\sigma = f_0 \left[\Gamma\left(\frac{2}{m} + 1\right) - \Gamma\left(\frac{1}{m} + 1\right)^2\right]^{\frac{1}{2}} \tag{6.9}$$

In the limit of a rigid backing layer, $H = 0$, contacting a flat substrate, $R = \infty$, the load distribution among fibrils is uniform. In this case, as was derived in Chapter 5, an analytical solution is available. Repeating the result here for completeness, the load as a function of displacement

$$F = Nku \left[\exp\left(-\left(\frac{ku}{f_0}\right)^m\right)\right] \tag{6.10}$$

and the adhesive strength of the array, as reflected by the detachment force, is

$$F_{\max} = N f_0 \left(\frac{1}{m}\right)^{\frac{1}{m}} \exp\left(-\frac{1}{m}\right) \tag{6.11}$$

When the load distribution among fibrils in the array is non-uniform, an additional source of stochastic behavior is introduced. The performance will depend on the position of strong fibrils in the array relative to the regions of high load. Consequently, the most convenient path forward is to adopt a numerical approach akin to a Monte Carlo simulation, where the strength data of (6.7) is randomly assigned to fibrils within the array. The averaged behavior over a series of tests is then considered.

6.2.2 Numerical implementation

For a given test, the strength data is assigned to fibrils in the array using a pseudorandom number generator. The condition on detachment, $f_i > f_{\max}^i$, differs for each fibril in the array. Several other small differences exist when compared to the numerical implementation of the attachment and detachment processes described in Section 3.2. In the case of the curved substrate, approach continues until all fibrils are in contact. In this condition, the difference in strain between the fibrils at the array center and the array edge is given by

$$\Delta\varepsilon = \frac{D^2}{2hR} \tag{6.12}$$

For ease of comparison between the load-displacement characteristics of curved substrates, we chose to adjust the datum and plot displacement, u, where $u = 0$ is the point at which the load becomes tensile.

In all tests described in the subsequent sections, the fibril length $h/a = 4$, the fibril separation $d/a = 4$, and the array dimension $D/a = 60$, such that the total number of fibrils $N = 721$. As in preceding chapters, we approximate the parameter closely related to the critical strain on a fibril at detachment as $f_0/\pi a^2 E^* = 0.1$, where we note that the normalization process now involves the Weibull measure of fibril adhesive strength, f_0. For the smallest radius of curvature examined, $R/a = 1250$, the difference in strain $\Delta\varepsilon = 0.36$. For each case involving a non-uniform load distribution ($H = \infty$ and/or $R \neq \infty$), the model test is repeated ten times. A representative result is shown for the load-displacement behavior, and the mean of all tests is reported for the normalized detachment force, $F_{\max}/Nf_0$.

6.3 Results

6.3.1 Uniform load distribution

Figure 6.2 shows the load-displacement characteristics for an adhesive with a rigid backing layer, $H = 0$, contacting a flat substrate, $R = \infty$, for which it is anticipated that the load distribution among fibrils is uniform. Two values of Weibull modulus are considered, representing large statistical variation in strength ($m = 5$) and deterministic strength ($m = \infty$). While an analytical result for this case is provided in (6.11), the numerical model is still utilized to visualize the detachment in the array. In particular, the insets of Figure 6.2 show the attached fibrils at the instant $F = F_{\max}$.

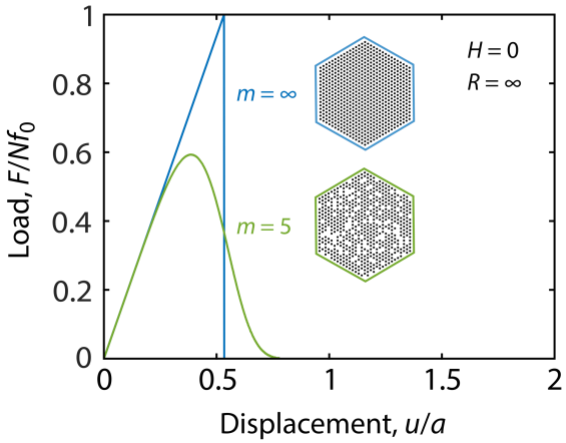

Figure 6.2. Model load-displacement characteristics for an adhesive with rigid backing layer, $H = 0$, for two values of the Weibull modulus, $m = 5$ and $m = \infty$ (deterministic fibril adhesive strength). Insets show the attached fibrils at the instant $F = F_{\max}$.

In the deterministic limit it is observed that simultaneous detachment occurs as all fibrils exceed their critical load, f_0, with the normalized detachment force being $F_{\max}/Nf_0 = 1$. In the stochastic case it is observed that weak fibrils in the array detach prior to the attainment of maximum load. Random detachments are observed across the array at the point of maximum load, with the normalized detachment force being $F_{\max}/Nf_0 = 0.59$.

The mean strength is marginally impacted by the reduction in the Weibull modulus, with (6.8) giving $\bar{f}_{\max} = 0.92f_0$ for $m = 5$. However, this $\sim 8\,\%$ reduction in mean strength when compared to $m = \infty$ cannot account for the percentage drop in strength of the array, which is $\sim 41\,\%$. It is the increase in the variability which must therefore be responsible. Consider that for a broad distribution in fibril adhesive strength, the mean would only be observed at the array scale if all fibrils could be made to bear their critical load simultaneously. Since the load

distribution among fibrils is dictated by features of the loading configuration (and in the current case is uniform), we observe that premature detachment of weak fibrils in the array cannot be compensated for by stronger than average fibrils. Mechanically, they reduce the overall stiffness and render the increase in load supported by fibrils in contact insufficient to compensate for further fibril detachments.

6.3.2 Backing layer compliance

Figure 6.3 shows the load-displacement characteristics for an adhesive with a fully compliant backing layer, $H = \infty$, contacting a flat substrate, $R = \infty$. Again, two values of the Weibull modulus are considered, $m = 5$ and $m = \infty$.

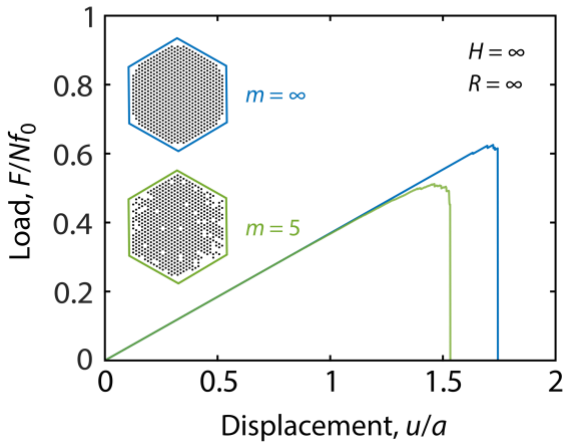

Figure 6.3. Model load-displacement characteristics for an adhesive with a fully compliant backing layer, $H = \infty$, for two values of the Weibull modulus, $m = 5$ and $m = \infty$ (deterministic fibril adhesive strength). Insets show the attached fibrils at the instant $F = F_{\max}$.

In the deterministic limit we observe that the characteristic array edge load concentration gives rise to the detachment of fibrils in this region. There is an accompanying reduction in the adhesive strength of the array, with the normalized detachment force being $F_{\max}/Nf_0 = 0.63$. In the stochastic case, there is also clear bias for detachment toward the array edge. The detachment of weaker fibrils in random positions throughout the array is also evident. These two effects act in combination to further reduce the adhesive strength of the array, with the normalized detachment force being $F_{\max}/Nf_0 = 0.52$. Significantly, however, the percentage reduction in adhesive strength of the array between $m = \infty$ and $m = 5$ is ~ 17 %. This is much lower than in the case of the rigid backing layer. This motivates exploration of the entire range of physically relevant Weibull modulii, and the comparison of the rigid and fully compliant backing layers.

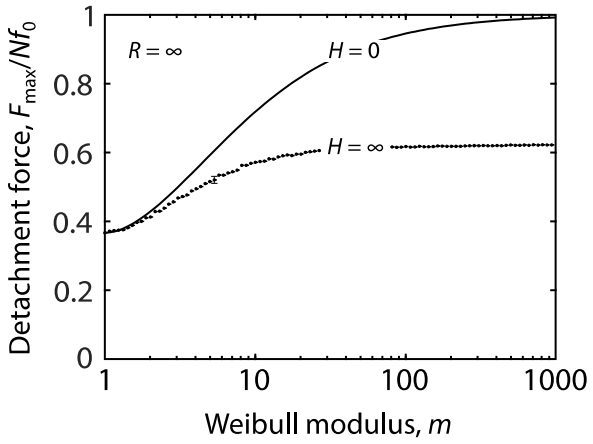

Figure 6.4. Normalized detachment force, $F_{\max}/Nf_0$, versus Weibull modulus, m. Results are presented for both a rigid backing layer, $H = 0$, and a fully compliant backing layer, $H = \infty$. The substrate considered is flat, $R = \infty$. For, $H = \infty$, where each data point represents the mean of ten repeat tests, an error bar showing the maximum standard deviation across all Weibull modulii is included.

Figure 6.4 examines the normalized detachment force, $F_{\max}/Nf_0$, as a function of the Weibull modulus, m, for both the rigid backing layer, $H = 0$, and fully compliant backing layer, $H = \infty$. The former is obtained from the analytical result of (6.11).

For the rigid backing layer, a monotonic reduction in the adhesive strength of the array is observed as the Weibull modulus is reduced (and the statistical variation in fibril adhesive strength increases). For the fully compliant backing layer, an extensive regime exists in which the strength of the array appears close to the limit associated with deterministic strength ($m = \infty$). In this regime the load concentration is dominant in its influence on the adhesive strength of the array. For low Weibull modulus we observe a monotonic reduction in the adhesive strength of the array as both the load concentration and statistical variation in fibril strength act in combination.

Perhaps most significantly, at sufficiently low Weibull modulus the strength of the array on a rigid backing layer and fully compliant backing layer are approximately equal. Weak fibrils across the array, rather than fibrils within the region of the load concentration, are the dominant contributor to the early detachments which give rise to the load maxima. The statistical properties consequently control the adhesive strength of the array. The convergence of the two results indicates that the distribution of fibril adhesive strength modulates the detrimental influence of the backing layer compliance related load concentration.

6.3.3 Substrate curvature

Figure 6.4 shows the load-displacement characteristics for an adhesive contacting a substrate with curvature, $R/a = 12500$. Attention is limited to a rigid backing layer, $H = 0$. Again, two values of the Weibull modulus are considered, $m = 5$ and $m = \infty$.

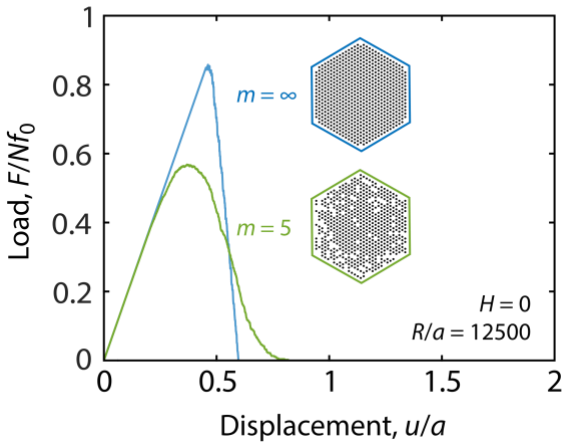

Figure 6.4. Model load-displacement characteristics for an adhesive on a curved substrate, $R/a = 12500$, for two values of the Weibull modulus, $m = 5$ and $m = \infty$ (deterministic fibril adhesive strength). The backing layer is rigid, $H = 0$. Insets show the attached fibrils at the instant $F = F_{\max}$.

Qualitatively, in these cases, the effect of substrate curvature is similar to backing layer compliance. For $m = \infty$ we observe an array edge load concentration which leads to the detachment of fibrils around the perimeter and reduces the strength as compared to a flat substrate. The normalized detachment force is $F_{\max}/Nf_0 = 0.86$. Introduction of variability in fibril adhesive strength, with $m = 5$, leads to further decay in the adhesive strength, with the normalized detachment force being $F_{\max}/Nf_0 = 0.58$.

The benefit of studying curvature is that, unlike backing compliance where we only possess solutions in the limiting cases of thickness, the severity of the array edge load concentration can be systematically varied by changing the radius. Note that the severity of the backing layer-controlled load concentration could also be increased by increasing the array size, but at additional computational cost.

Figure 6.5 examines the normalized detachment force, $F_{\max}/Nf_0$, as a function of the Weibull modulus, m, for a range of substrate curvatures. For each curvature we observe a regime in which the adhesive strength of the array is relatively constant, having approached the limit associated with dominance of the array edge load concentration. As the radius of curvature is reduced, this load concentration becomes more severe. Consequently, the range of Weibull modulii over which this regime extends increases.

For large radii of curvature, $R/a = 6250$ or $R/a = 12500$, the same effect as evidenced for backing layer compliance is observed. As the statistical variation in fibril strength is increased (via reduction in the Weibull modulus), there is a decay in the adhesive strength of the array. At sufficiently low Weibull modulii, the statistical properties of fibril strength dominate. The adhesive strength of the array is approximately independent of curvature.

For small radii of curvature, $R/a = 1250$ or $R/a = 2500$, several interesting trends emerge. The first is that the adhesive strength at $m = 1$ does not converge upon the same value, indicating that a regime of statistical dominance is not encountered over the entire physical range of Weibull modulii. Furthermore, the load concentration becomes so severe that it falls

below the strength associated with statistical control in the limit $m = 1$. Consequently, as the influence of statistical variation is felt for low Weibull modulii, it has a positive influence on the adhesive strength of the array. This reveals additional complexity which was not evidenced in the examination of backing layer compliance. When the load is highly localized to the contact edge, the detrimental impact of weak fibrils detaching across the array is minimal in comparison the benefit of adding high strength fibrils to the highly stretched region. These fibrils contribute significantly to the total load, and the adhesive strength of the array is increased.

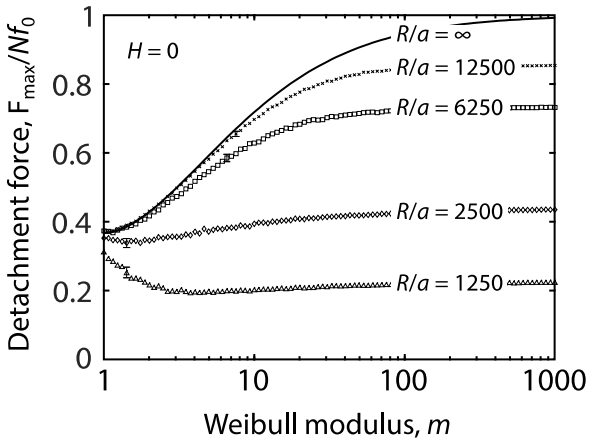

Figure 6.5. Normalized detachment force, $F_{\max}/Nf_0$, versus Weibull modulus, m, for a range of values of substrate curvature, R/a. Results are presented for a rigid backing layer, $H = 0$. For all $R/a \neq \infty$, where each data point represents the mean of ten repeat tests, an error bar showing the maximum standard deviation across all Weibull modulii is included.

6.4 Discussion

This work has revealed a nuanced dependence of the adhesive strength of a fibrillar array on both the statistical distribution of the adhesive strength of individual fibrils and the load distribution at the array scale. For limited statistical variation in the fibril adhesive strength, load concentrations play a dominant role. For large statistical variation, transition to a regime independent of the load distribution may occur. Depending on the severity of the load concentration, increased statistical variation can have either a detrimental or beneficial impact on adhesive strength.

The observation that the statistical properties of the adhesive strength of sub-contacts can modulate the influence of the load concentrations at a fibrillar interface is of great significance in the study of dry adhesives. Experimental characterization approaches often require consideration of the geometry of the loading configuration, and the resulting load distribution, to extract a metric for fibril performance. Consider the model of Schargott et al. [103], which provides an analytical result for the problem of fibrils on a rigid backing layer indented by a spherical probe. The detachment force was given in (2.48), and yields agreement with the model presented only in the limit $m = \infty$.

The influence of statistical variation in fibril strength may also play a role in design of fibrillar dry adhesives. The decay in array strength with increasing size, which necessitates structural hierarchy in order to scale load bearing capability, is controlled by backing layer compliance. Since the influence of backing layer compliance is modulated by the variability in fibril

adhesive strength, both design criterion and anticipated performance may be influenced by the statistical properties of fibril strength.

Chapter 7

Conclusions

7.1 Summary

Bioinspired dry adhesives have the potential to address the requirements for strong, reversible, and repeatable temporary bonding in a range of emerging applications. While there have been considerable advances in the understanding of the mechanics of these microstructures, there is a need for further investigation of the mechanics across length scales to both guide systematic experimental characterization of adhesives and understanding the scaling of performance to large areas. This work has attempted to address several requirements in this regard.

We have, for the first time, studied the response to non-ideal loading of fibrillar adhesive patches in the form of misalignment at the interface. Chapter 3 describes a parametric investigation based on a discrete contact mechanics model which considered the effects of backing layer compliance and the substrate geometry. Numerical implementation was required to capture the non-linear response associated with attachment and detachment of the fibril array. As fibril spacing, fibril length, and misalignment angle were varied, regimes of dominance of either backing layer compliance or misalignment in controlling the detachment were revealed. The misalignment dominated regime was of particular significance, as the role

of backing layer compliance was seen to switch from being detrimental to the strength of the fibrillar array to being beneficial. This was associated with a shielding effect at the detachment front, with backing layer deformation reducing the differential stretching of fibrils. While compliance has been known to have a beneficial effect for the formation of contact, the existence of this enhancement of resistance to peel propagation during detachment was previously unknown.

Subsequent experimental investigation, detailed in Chapter 4, revealed this regime was prevalent in an adhesive patch consisting of an array of mushroom-tipped PDMS microfibrils on a backing layer of the same material. It was shown that the circumferential array edge detachment mechanism which controls the strength in ideally flat adhesive contacts gave way to a peel-like detachment for misalignment of just $\sim 0.2°$ over a patch size of 2 mm. In this regime backing layer compliance was found to be beneficial to the adhesive strength. Understanding this detachment mechanism is important for application of fibrillar adhesive patches in applications involving flat substrates without precise control of alignment or where surface undulations at the length scales larger than the size of the patch are present, for example in pick-and-place component handling.

The same model also revealed the promise of radial compliance gradients in improving the load distribution among fibrils. Not only was the adhesive strength of the array improved in the aligned state, but enhanced resistance to peel propagation was also observed. Future research directions in this area will be discussed in the subsequent section.

Despite past work suggesting the significance of the variability in fibril adhesive strength in controlling the behavior of fibril arrays, the statistical characterization of performance had received limited attention. The work described in Chapter 5 represents the first attempt to characterize the statistical properties of fibril strength in a systematic way. The framework for this was based upon the statistical theory of fracture. Utilizing experimental set-up with high resolution in-situ contact visualization, we were able to characterize adhesive strength on a fibril-by-fibril basis. Additionally, this visualization provided information about the character of the critical defect at each fibril. Two distinct detachment modes were revealed. The first is associated with the fundamental fibril-geometry-dependent mechanism, with defect nucleation in the mushroom-tipped fibril occurring in the region of the interface under the intersection of stalk and flange. The second is extraneous to the anticipated operation, being associated with fabrication imperfections in the mushroom flange. The concurrent existence of these two populations complicates the statistical characterization of each population individually. A methodology was adopted to address this, first involving a specialized approach to ranking of fibril strength which approximately decouples the fundamental population. Upon characterizing the associated statistical properties, a bimodal probability framework was used to characterize the extraneous secondary mechanism. The allows for the assessment of the impact of this mechanism on overall performance, with the reduction in adhesive strength of ~ 40 % being of the same order as the number of fibrils with fabrication imperfections. The ability to decouple fundamental and extraneous mechanisms, identifying an upper bound on strength associated with the former, is a powerful tool for the analysis of fibrillar adhesive performance moving forward. Understanding the distribution in defect size also has the potential to reveal the role of surface roughness, contaminant particles, and fabrication

imperfections in controlling the adhesive strength of fibrillar sub-contacts. Future research opportunities in this area are discussed in the subsequent section.

This study also raised the question of how variability in fibril adhesive strength and non-uniform load distribution at the array scale, together determine performance of adhesive patches. Utilizing the discrete contact mechanics model previously described, and including ideally Weibull distributed strength, these effects were investigated in Chapter 6. Statistical variation in fibril adhesive strength is found to modulate the influence of load concentrations in controlling the strength of the array. For low variability, the load distribution is found to dominate. For high variability, statistical properties can dominate. The latter leads to insensitivity of the adhesive performance to changes in backing layer compliance or substrate curvature. Depending on the severity of the load concentration, increase in variability can be associated with either an improvement or reduction in strength. This is the first time that this nuanced interplay between the statistical properties of fibril adhesive strength and the load distribution have been revealed.

7.2 Future work

Despite continued progress in understanding the performance of bioinspired dry adhesives, challenges preventing their widespread application remain. Advances are likely to be closely tied to the capabilities of novel fabrication techniques, and emerging research areas such as mechanical metamaterials. Designs are likely to remain highly application specific. Several interesting avenues for future research have been suggested by the work described here.

Thus far the performance of dry adhesives on rough substrates, particularly over large areas, has been limited. Structural hierarchy and compliance are known to be key to this effort. Multi-level fibrillar structures have proven challenging from a fabrication perspective, and mechanisms to improve the strength on these surfaces should focus on commensurability with fabrication capabilities. Theoretical investigation of improved adhesive performance of fibril arrays by inclusion of radial compliance gradients at the interface, detailed in Chapter 3, have motivated further investigation in this area. At the fibril scale, bimaterial structures with curved interfaces have been shown to improve the interfacial load distribution and in turn the adhesive strength [13]. Incorporation of equivalent features in the backing structure, achieving a radial gradient in backing layer compliance, could represent a promising form of structural hierarchy without the need for fibrillar subdivision. Moving forward, advances in additive manufacturing will likely offer new opportunities to achieve radial compliance gradients by local tailoring of material composition [128].

Investigation of the statistical properties of fibril adhesive strength remains in its nascent stages. Moving forward, it is our hope that the statistical characterization of fibril strength will prove to be a useful tool for assessment of performance in a variety of conditions. Of particular interest is the examination of adhesion on substrates with more severe surface roughness [97-99]. Where roughness exists on much smaller scales than the fibrils themselves (as in Chapter 5) we anticipate that the tip geometry will control the interfacial stress distribution and thus the region from which defect propagation occurs. Roughness will control the size of nucleation points within this region. As the length scale of roughness increases, the dominant role of the tip geometry may be precluded. Defects may propagate from multiple regions across the tip-

substrate interface. In this case it will be necessary to consider the non-uniform load distribution at the interface within the statistical framework if the defect size distribution is to be characterized, as has been done in the context of brittle fracture [129, 130]. We also note that the influence of surface roughness may change in the presence of fluid at the interface, with the formation of capillary bridges effectively extending the range of the surface interaction [131]. Molecular dynamics simulations (e.g. [132]) may prove to be a useful tool in bridging the gap between surface roughness and defect size, and any efforts in this regard should consider the dependence on the compressive preload applied when making contact.

Other topics of interest include systematic assessment of the role of surface contaminants [133], where introduction of a known size distribution of particles to the substrate may provide insight as to how these give rise to defects and in turn control fibril strength. Intentional introduction of fabrication imperfections [21] could also provide fundamental insight in to the mechanics governing fibril adhesive strength. Furthermore, statistical characterization at various stages of cyclic loading can shed light on the durability of fibrils, where damage may accumulate over time [118]. The presence of shear at the interface [134] will also change the characteristics of the interfacial stress distribution and thus likely the statistical properties of fibril adhesive strength.

References

1. Creton, C., *Pressure-Sensitive Adhesives: An Introductory Course.* MRS Bulletin, 2013. **28**(6): p. 434-439.
2. Gay, C. and L. Leibler, *On Stickiness.* Physics Today, 1999. **52**(11): p. 48-52.
3. Gent, A.N., P.B. Lindley, and E.K. Rideal, *Internal rupture of bonded rubber cylinders in tension.* Proceedings of the Royal Society of London. Series A. Mathematical and Physical Sciences, 1959. **249**(1257): p. 195-205.
4. Kaelble, D.H., *Peel Adhesion: Micro - Fracture Mechanics of Interfacial Unbonding of Polymers.* Transactions of the Society of Rheology, 1965. **9**(2): p. 135-163.
5. Andrews, E.H. and A.J. Kinloch, *Mechanics of Adhesive Failure. I.* Proceedings of the Royal Society of London. Series A, Mathematical and Physical Sciences, 1973. **332**: p. 385-399.
6. Fantoni, G., et al., *Grasping devices and methods in automated production processes.* CIRP Annals - Manufacturing Technology, 2014. **63**(2): p. 679-701.
7. Sitti, M. and R.S. Fearing, *Synthetic gecko foot-hair micro/nano-structures as dry adhesives.* Journal of Adhesion Science and Technology, 2003. **17**(8): p. 1055-1073.
8. Geim, A.K., et al., *Microfabricated adhesive mimicking gecko foot-hair.* Nature Materials, 2003. **2**(7): p. 461-463.
9. Northen, M.T. and K.L. Turner, *A batch fabricated biomimetic dry adhesive.* Nanotechnology, 2005. **16**(8): p. 1159-1166.
10. del Campo, A., C. Greiner, and E. Arzt, *Contact Shape Controls Adhesion of Bioinspired Fibrillar Surfaces.* Langmuir, 2007. **23**(20): p. 10235-10243.
11. Sameoto, D. and C. Menon, *Deep UV patterning of acrylic masters for molding biomimetic dry adhesives.* Journal of Micromechanics and Microengineering, 2010. **20**(11): p. 115037.
12. Minsky, H.K. and K.T. Turner, *Achieving enhanced and tunable adhesion via composite posts.* Applied Physics Letters, 2015. **106**(20): p. 201604.
13. Fischer, S.C.L., E. Arzt, and R. Hensel, *Composite Pillars with a Tunable Interface for Adhesion to Rough Substrates.* ACS Applied Materials & Interfaces, 2017. **9**(1): p. 1036-1044.
14. Minsky, H.K. and K.T. Turner, *Composite Microposts with High Dry Adhesion Strength.* ACS Applied Materials and Interfaces, 2017. **9**(21): p. 18322-18327.
15. Fischer, S.C.L., et al., *Funnel-Shaped Microstructures for Strong Reversible Adhesion.* Advanced Materials Interfaces, 2017: p. 1700292.
16. Parness, A., et al., *A microfabricated wedge-shaped adhesive array displaying gecko-like dynamic adhesion, directionality and long lifetime.* Journal of The Royal Society Interface, 2009. **6**(41): p. 1223-1232.
17. Yu, J., et al., *Gecko-Inspired Dry Adhesive for Robotic Applications.* Advanced Functional Materials, 2011. **21**(16): p. 3010-3018.
18. Tamelier, J., S. Chary, and K.L. Turner, *Vertical anisotropic microfibers for a gecko-inspired adhesive.* Langmuir, 2012. **28**(23): p. 8746-8752.
19. Chary, S., J. Tamelier, and K. Turner, *A microfabricated gecko-inspired controllable and reusable dry adhesive.* Smart Materials and Structures, 2013. **22**(2): p. 25013.

20. Murphy, M.P., B. Aksak, and M. Sitti, *Gecko-inspired directional and controllable adhesion.* Small, 2009. **5**(2): p. 170-175.
21. Khaled, W.B. and D. Sameoto, *Anisotropic dry adhesive via cap defects.* Bioinspiration & Biomimetics, 2013. **8**(4): p. 44002.
22. Noderer, W.L., et al., *Enhanced adhesion and compliance of film-terminated fibrillar surfaces.* Proceedings of the Royal Society of London A: Mathematical, Physical and Engineering Sciences, 2007. **463**(2086): p. 2631-2654.
23. Bartlett, M.D., et al., *Looking beyond fibrillar features to scale gecko-like adhesion.* Advanced Materials, 2012. **24**(8): p. 1078-1083.
24. Gorb, S.N., *Attachment Devices of Insect Cuticle*. 2001, New York, NY: Springer Science & Business Media. 1-305.
25. Irschick, D.J., et al., *A comparative analysis of clinging ability among pad-bearing lizards.* Biological Journal of the Linnean Society, 1996. **59**(1): p. 21-35.
26. Irschick, D.J., et al., *Effects of loading and size on maximum power output and gait characteristics in geckos.* Journal of Experimental Biology, 2003. **206**(22): p. 3923-3934.
27. Cartier, O., *Studien über den feineren Bau der Epidermis bei den Geckotiden*. 1872, Stahel'sche Buchdr.
28. Schmidt, H.R., *Zur anatomie und physiologie der geckopfote.* Jena Z Naturw, 1904. **39**: p. 551.
29. Ruibal, R. and V. Ernst, *Structure of Digital Setae of Lizards.* Journal of Morphology, 1965. **117**(3): p. 271-293.
30. Kim, T.W. and B. Bhushan, *Effect of stiffness of multi-level hierarchical attachment system on adhesion enhancement.* Ultramicroscopy, 2007. **107**(10-11): p. 902-912.
31. Russell, A.P., *The morphological basis of weight-bearing in the scansors of the tokay gecko (Reptilia: Sauria).* Canadian Journal of Zoology, 1986. **64**(4): p. 948-955.
32. Peattie, A.M., et al., *Ancestrally high elastic modulus of gecko setal β-keratin.* Journal of The Royal Society Interface, 2007. **4**(17): p. 1071-1076.
33. Hansen, W.R. and K. Autumn, *Evidence for self-cleaning in gecko setae.* Proceedings of the National Academy of Sciences, 2005. **102**(2): p. 385-389.
34. Gravish, N., et al., *Rate-dependent frictional adhesion in natural and synthetic gecko setae.* Journal of The Royal Society Interface, 2010. **7**(43): p. 259-269.
35. W.D., D., *Zur anatomie und physiologie der Geckozehe.* Jena Z Naturw, 1934. **68**: p. 613-656.
36. Hiller, U., *Untersuchungen zum Feinbau und zur Funktion der Haftborsten von Reptilien.* Zeitschrift für Morphologie der Tiere, 1968. **62**(4): p. 307-362.
37. Autumn, K., et al., *Adhesive force of a single gecko foot-hair.* Nature, 2000. **405**(6787): p. 681-685.
38. Autumn, K., et al., *Evidence for van der Waals adhesion in gecko setae.* Proceedings of the National Academy of Sciences, 2002. **99**(19): p. 12252-12256.
39. Kamperman, M., et al., *Functional Adhesive Surfaces with "Gecko" Effect: The Concept of Contact Splitting.* Advanced Engineering Materials, 2010. **12**(5): p. 335-348.
40. Persson, B.N.J., *On the mechanism of adhesion in biological systems.* The Journal of Chemical Physics, 2003. **118**(16): p. 7614-7621.

41. Glassmaker, N.J., et al., *Design of biomimetic fibrillar interfaces: 1. Making contact.* Journal of The Royal Society Interface, 2004. **1**(1): p. 23-33.
42. Autumn, K., et al., *Effective elastic modulus of isolated gecko setal arrays.* Journal of Experimental Biology, 2006. **209**(18): p. 3558-3568.
43. Schargott, M., *A mechanical model of biomimetic adhesive pads with tilted and hierarchical structures.* Bioinspiration & Biomimetics, 2009. **4**(2): p. 26002.
44. Arzt, E., S. Gorb, and R. Spolenak, *From micro to nano contacts in biological attachment devices.* Proceedings of the National Academy of Sciences, 2003. **100**(19): p. 10603-10606.
45. McMeeking, R.M., E. Arzt, and A.G. Evans, *Defect Dependent Adhesion of Fibrillar Surfaces.* The Journal of Adhesion, 2008. **84**(7): p. 675-681.
46. Hui, C.Y., et al., *Design of biomimetic fibrillar interfaces: 2. Mechanics of enhanced adhesion.* Journal of The Royal Society Interface, 2004. **1**(1): p. 35-48.
47. Tang, T., C.-Y. Hui, and N.J. Glassmaker, *Can a fibrillar interface be stronger and tougher than a non-fibrillar one?* Journal of The Royal Society Interface, 2005. **2**(5): p. 505-516.
48. Gao, H., et al., *Mechanics of hierarchical adhesion structures of geckos.* Mechanics of Materials, 2005. **37**(2–3): p. 275-285.
49. Jagota, A. and S.J. Bennison, *Mechanics of Adhesion Through a Fibrillar Microstructure.* Integrative and Comparative Biology, 2002. **42**(6): p. 1140-1145.
50. Yao, H. and H. Gao, *Mechanics of robust and releasable adhesion in biology: Bottom–up designed hierarchical structures of gecko.* Journal of the Mechanics and Physics of Solids, 2006. **54**(6): p. 1120-1146.
51. Yao, H. and H. Gao, *Multi-scale cohesive laws in hierarchical materials.* International Journal of Solids and Structures, 2007. **44**(25–26): p. 8177-8193.
52. Autumn, K., et al., *Dynamics of geckos running vertically.* Journal of Experimental Biology, 2006. **209**(2): p. 260-272.
53. Autumn, K., et al., *Frictional adhesion: A new angle on gecko attachment.* Journal of Experimental Biology, 2006. **209**(18): p. 3569-3579.
54. Hawkes, E.W., et al. *Grasping without squeezing: Shear adhesion gripper with fibrillar thin film*. in *2015 IEEE International Conference on Robotics and Automation (ICRA)*. 2015.
55. Jiang, H., et al. *Scaling controllable adhesives to grapple floating objects in space*. in *Proceedings - IEEE International Conference on Robotics and Automation*. 2015.
56. Paretkar, D., et al., *Bioinspired pressure actuated adhesive system.* Materials Science and Engineering: C, 2011. **31**(6): p. 1152-1159.
57. Paretkar, D., et al., *Preload-responsive adhesion: effects of aspect ratio, tip shape and alignment.* Journal of The Royal Society Interface, 2013. **10**(83): p. 20130171.
58. Isla, P.Y. and E. Kroner, *A Novel Bioinspired Switchable Adhesive with Three Distinct Adhesive States.* Advanced Functional Materials, 2015. **25**(16): p. 2444-2450.
59. Gorb, S.N. and M. Varenberg, *Mushroom-shaped geometry of contact elements in biological adhesive systems.* Journal of Adhesion Science and Technology, 2007. **21**(12-13): p. 1175-1183.

60. Varenberg, M. and S. Gorb, *Close-up of mushroom-shaped fibrillar adhesive microstructure: contact element behaviour.* Journal of the Royal Society, Interface, 2008. **5**(24): p. 785-789.
61. Heepe, L., et al., *Adhesion Failure at 180 000 Frames per Second: Direct Observation of the Detachment Process of a Mushroom-Shaped Adhesive.* Physical Review Letters, 2013. **111**(10): p. 104301.
62. Tinnemann, V., et al., *In Situ Observation Reveals Local Detachment Mechanisms and Suction Effects in Micropatterned Adhesives.* Advanced Functional Materials, 2019: p. 1807713.
63. Spuskanyuk, A.V., et al., *The effect of shape on the adhesion of fibrillar surfaces.* Acta Biomaterialia, 2008. **4**(6): p. 1669-1676.
64. Balijepalli, R.G., et al., *Numerical simulation of the edge stress singularity and the adhesion strength for compliant mushroom fibrils adhered to rigid substrates.* International Journal of Solids and Structures, 2016. **85-86**: p. 160-171.
65. Murphy, M.P., S. Kim, and M. Sitti, *Enhanced Adhesion by Gecko-Inspired Hierarchical Fibrillar Adhesives.* ACS Applied Materials & Interfaces, 2009. **1**(4): p. 849-855.
66. Wang, Y., et al., *Fabrication of Well-Defined Mushroom-Shaped Structures for Biomimetic Dry Adhesive by Conventional Photolithography and Molding.* ACS Applied Materials & Interfaces, 2014. **6**(4): p. 2213-2218.
67. Brodoceanu, D., et al., *Hierarchical bioinspired adhesive surfaces-A review.* Bioinspiration and Biomimetics, 2016. **11**(5): p. 051001.
68. Long, R. and C.Y. Hui, *The effect of preload on the pull-off force in indentation tests of microfibre arrays.* Proceedings of the Royal Society A: Mathematical, Physical and Engineering Sciences, 2009. **465**: p. 961-981.
69. Kroner, E., et al., *Adhesion of Flat and Structured PDMS Samples to Spherical and Flat Probes: A Comparative Study.* The Journal of Adhesion, 2011. **87**(5): p. 447-465.
70. Long, R., et al., *Modeling the soft backing layer thickness effect on adhesion of elastic microfiber arrays.* Journal of Applied Physics, 2008. **104**(4): p. 0-9.
71. Israelachvili, J.N., *Intermolecular and Surface Forces*. 2011, San Diego: Academic Press. 3-22.
72. London, F., *The general theory of molecular forces.* Transactions of the Faraday Society, 1937. **33**: p. 8-26.
73. de Boer, J.H., *The influence of van der Waals' forces and primary bonds on binding energy, strength and orientation, with special reference to some artificial resins.* Transactions of the Faraday Society, 1936. **32**: p. 10-36.
74. Hamaker, H.C., *The London—van der Waals attraction between spherical particles.* Physica, 1937. **4**(10): p. 1058-1072.
75. Bradley, R.S., *LXXIX. The cohesive force between solid surfaces and the surface energy of solids.* The London, Edinburgh, and Dublin Philosophical Magazine and Journal of Science, 1932. **13**(86): p. 853-862.
76. Derjaguin, B.V., *Friction and adhesion. IV. The theory of adhesion of small particles.* Kolloid Zeitschrift, 1934. **69**(2): p. 155-164.

77. Griffith, A.A., *The Phenomena of Rupture and Flow in Solids.* Philosophical Transactions of the Royal Society of London. Series A, Containing Papers of a Mathematical or Physical Character, 1921. **221**: p. 163-198.
78. Irwin, G.R., *Onset of fast crack propagation in high strength steel and aluminum alloys.* Sagamore Research Conference Proceedings, 1956. **2**: p. 289-305.
79. Sneddon, I.N., *The Distribution of Stress in the Neighbourhood of a Crack in an Elastic Solid.* Proceedings of the Royal Society of London A: Mathematical, Physical and Engineering Sciences, 1946. **187**(1009): p. 229-260.
80. Irwin, G.R., *Analysis of stresses and strains near the end of a crack traversing a plate.* Journal of Applied Mechanics, 1957. **24**: p. 361-364.
81. Hutchinson, J.W. and Z. Suo, *Mixed Mode Cracking in Layered Materials*, W.H. John and Y.W. Theodore, Editors. 1992, Elsevier. p. 63-191.
82. Dundurs, J., *Discussion: "Edge-Bonded Dissimilar Orthogonal Elastic Wedges Under Normal and Shear Loading" (Bogy, D. B., 1968, ASME J. Appl. Mech., 35, pp. 460–466).* Journal of Applied Mechanics, 1969. **36**(3): p. 650-652.
83. Rice, J.R., *Elastic Fracture Mechanics Concepts for Interfacial Cracks.* Journal of Applied Mechanics, 1988. **55**(1): p. 98-103.
84. Dugdale, D.S., *Yielding of steel sheets containing slits.* Journal of the Mechanics and Physics of Solids, 1960. **8**(2): p. 100-104.
85. Maugis, D., *Adhesion of spheres: The JKR-DMT transition using a dugdale model.* Journal of Colloid and Interface Science, 1992. **150**(1): p. 243-269.
86. Barthel, E., *On the Description of the Adhesive Contact of Spheres with Arbitrary Interaction Potentials.* Journal of Colloid and Interface Science, 1998. **200**(1): p. 7-18.
87. Kassir, M.K. and A.M. Bregman, *The Stress-Intensity Factor for a Penny-Shaped Crack Between Two Dissimilar Materials.* Journal of Applied Mechanics, 1972. **39**(1): p. 308-310.
88. Kendall, K., *The adhesion and surface energy of elastic solids.* Journal of Physics D: Applied Physics, 1971. **4**(8): p. 1186.
89. Khaderi, S.N., et al., *Detachment of an adhered micropillar from a dissimilar substrate.* Journal of the Mechanics and Physics of Solids, 2015. **75**: p. 159-183.
90. Johnson, K.L., *Contact Mechanics*. 1985, Cambridge; New York: Cambridge University Press.
91. Bogy, D.B., *Two Edge-Bonded Elastic Wedges of Different Materials and Wedge Angles Under Surface Tractions.* Journal of Applied Mechanics, 1971. **38**(2): p. 377-386.
92. Johnson, K.L., K. Kendall, and A.D. Roberts, *Surface Energy and the Contact of Elastic Solids.* Proceedings of the Royal Society of London. Series A, Mathematical and Physical Sciences, 1971. **324**(1558): p. 301-313.
93. Derjaguin, B.V., V.M. Muller, and Y.P. Toporov, *Effect of contact deformations on the adhesion of particles.* Journal of Colloid and Interface Science, 1975. **53**(2): p. 314-326.
94. Hertz, H., *Uber die Berührung fester elatischer Körper (On the contact of elastic solids).* Journal Reine und angewandte Mathematik, 1882. **92**(110): p. 156-171.
95. Tabor, D., *Surface forces and surface interactions.* Journal of Colloid and Interface Science, 1977. **58**(1): p. 2-13.

96. Balijepalli, R.G., et al., *Numerical study of adhesion enhancement by composite fibrils with soft tip layers.* Journal of the Mechanics and Physics of Solids, 2017. **99**: p. 357-378.
97. Canas, N., et al., *Effect of nano- and micro-roughness on adhesion of bioinspired micropatterned surfaces.* Acta Biomaterialia, 2012. **8**(1): p. 282-288.
98. Kasem, H. and M. Varenberg, *Effect of counterface roughness on adhesion of mushroom-shaped microstructure.* Journal of The Royal Society Interface, 2013. **10**(87): p. 20130620.
99. Barreau, V., et al., *Fibrillar Elastomeric Micropatterns Create Tunable Adhesion Even to Rough Surfaces.* Advanced Functional Materials, 2016. **26**(26): p. 4687-4694.
100. Hui, C.Y., et al., *Constraints on Microcontact Printing Imposed by Stamp Deformation.* Langmuir, 2002. **18**(4): p. 1394-1407.
101. Cranford, S., et al., *A single degree of freedom 'lollipop' model for carbon nanotube bundle formation.* Journal of the Mechanics and Physics of Solids, 2010. **58**(3): p. 409-427.
102. Kim, S., et al., *Effect of backing layer thickness on adhesion of single-level elastomer fiber arrays.* Applied Physics Letters, 2007. **91**(16): p. 161905.
103. Schargott, M., V.L. Popov, and S. Gorb, *Spring model of biological attachment pads.* Journal of Theoretical Biology, 2006. **243**(1): p. 48-53.
104. Guidoni, G.M., et al., *Discrete contact mechanics of a fibrillar surface with backing layer interactions.* Journal of the Mechanics and Physics of Solids, 2010. **58**(10): p. 1571-1581.
105. Greiner, C., et al., *Experimental Parameters Controlling Adhesion of Biomimetic Fibrillar Surfaces.* The Journal of Adhesion, 2009. **85**(9): p. 646-661.
106. Bhushan, B., A.G. Peressadko, and T.-W. Kim, *Adhesion analysis of two-level hierarchical morphology in natural attachment systems for 'smart adhesion'.* Journal of Adhesion Science and Technology, 2006. **20**(13): p. 1475-1491.
107. Hui, C.-Y., et al., *Design of bio-inspired fibrillar interfaces for contact and adhesion — theory and experiments.* Journal of Adhesion Science and Technology, 2007. **21**(12-13): p. 1259-1280.
108. Daniels Henry, E. and H. Jeffreys, *The statistical theory of the strength of bundles of threads. I.* Proceedings of the Royal Society of London. Series A. Mathematical and Physical Sciences, 1945. **183**: p. 405-435.
109. Porwal, P.K. and C.Y. Hui, *Strength statistics of adhesive contact between a fibrillar structure and a rough substrate.* Journal of the Royal Society Interface, 2008. **5**(21): p. 441-448.
110. Weibull, W., *A statistical theory of the strength of materials*. Ingeniörsvetenskapsakademiens handlingar. 1939, Stockholm: Generalstabens litografiska anstalts förlag.
111. Stark, S., M.R. Begley, and R.M. McMeeking, *The Buckling and Postbuckling of Fibrils Adhering to a Rigid Surface.* Journal of Applied Mechanics, 2013. **80**(4): p. 41022.
112. Yao, H. and H. Gao, *Gibson-soil-like materials achieve flaw-tolerant adhesion.* Journal of Computational and Theoretical Nanoscience, 2010. **7**(7): p. 1299-1305.

113. Gao, H. and H. Yao, *Shape insensitive optimal adhesion of nanoscale fibrillar structures.* Proceedings of the National Academy of Sciences, 2004. **101**(21): p. 7851-7856.
114. Purtov, J., et al., *Improved development procedure to enhance the stability of microstructures created by two-photon polymerization.* Microelectronic Engineering, 2018. **194**: p. 45-50.
115. Booth, J.A., et al., *Benefit of Backing-Layer Compliance in Fibrillar Adhesive Patches-Resistance to Peel Propagation in the Presence of Interfacial Misalignment.* Advanced Materials Interfaces, 2018: p. 1800272.
116. Hawkes, E.W., et al., *Human climbing with efficiently scaled gecko-inspired dry adhesives.* Journal of The Royal Society Interface, 2015. **12**(102).
117. Song, S., et al., *Controllable load sharing for soft adhesive interfaces on three-dimensional surfaces.* Proceedings of the National Academy of Sciences, 2017. **114**(22): p. E4344-E4353.
118. Hensel, R., K. Moh, and E. Arzt, *Engineering Micropatterned Dry Adhesives: From Contact Theory to Handling Applications.* Advanced Functional Materials, 2018. **28**(28): p. 1800865.
119. Hansen, A., P.C. Hemmer, and S. Pradhan, *The fiber bundle model: modeling failure in materials*. 2015: John Wiley & Sons.
120. Chi, Z., T.-W. Chou, and G. Shen, *Determination of single fibre strength distribution from fibre bundle testings.* Journal of Materials Science, 1984. **19**(10): p. 3319-3324.
121. R'Mili, M., T. Bouchaour, and P. Merle, *Estimation of Weibull parameters from loose-bundle tests.* Composites Science and Technology, 1996. **56**(7): p. 831-834.
122. Berger, M.H. and D. Jeulin, *Statistical analysis of the failure stresses of ceramic fibres: Dependence of the Weibull parameters on the gauge length, diameter variation and fluctuation of defect density.* Journal of Materials Science, 2003. **38**(13): p. 2913-2923.
123. Johnson, C.A., *Fracture statistics of multiple flaw distributions*, in *Fracture mechanics of ceramics*, R.G. Brandt, et al., Editors. 1981, Plenum: New York. p. 365-385.
124. Johnson, L.G., *The statistical treatment of fatigue experiments*. 1964, Amsterdam: Elsevier.
125. Bacca, M., et al., *Load sharing in bioinspired fibrillar adhesives with backing layer interactions and interfacial misalignment.* Journal of the Mechanics and Physics of Solids, 2016. **96**: p. 428-444.
126. Harlow, D.G. and S.L. Phoenix, *Approximations for the strength distribution and size effect in an idealized lattice model of material breakdown.* Journal of the Mechanics and Physics of Solids, 1991. **39**(2): p. 173-200.
127. Schindelin, J., et al., *Fiji: an open-source platform for biological-image analysis.* Nature Methods, 2012. **9**: p. 676-682.
128. Yang, Y., et al., *Recent Progress in Biomimetic Additive Manufacturing Technology: From Materials to Functional Structures.* Advanced Materials, 2018: p. 1706539.
129. Matthews, J.R., F.A. Mcclintock, and W.J. Shack, *Statistical Determination of Surface Flaw Density in Brittle Materials.* Journal of the American Ceramic Society, 1976. **59**(7-8): p. 304-308.

130. Evans, A.G. and R.L. Jones, *Evaluation of a Fundamental Approach for the Statistical Analysis of Fracture.* Journal of the American Ceramic Society, 1978. **61**(3‐4): p. 156-160.
131. Kovalev, A.E., M. Varenberg, and S.N. Gorb, *Wet versus dry adhesion of biomimetic mushroom-shaped microstructures.* Soft Matter, 2012. **8**(29): p. 7560-7566.
132. Pastewka, L. and M.O. Robbins, *Contact area of rough spheres: Large scale simulations and simple scaling laws.* Applied Physics Letters, 2016. **108**(22): p. 221601.
133. Amador, G.J., T. Endlein, and M. Sitti, *Soiled adhesive pads shear clean by slipping: a robust self-cleaning mechanism in climbing beetles.* Journal of The Royal Society Interface, 2017. **14**: p. 20170134.
134. Gorb, S. and M. Varenberg, *Shearing of fibrillar adhesive microstructure: friction and shear-related changes in pull-off force.* Journal of The Royal Society Interface, 2007. **4**(15): p. 721-725.
135. Griffiths, W.D. and N.-W. Lai, *Double Oxide Film Defects in Cast Magnesium Alloy.* Metallurgical and Materials Transactions A, 2007. **38**(1): p. 190-196.
136. Meganck, J.A., et al., *Biaxial flexure testing of calcium phosphate bioceramics for use in tissue engineering.* Journal of Biomedical Materials Research Part A, 2005. **72**(1): p. 115-126.
137. Eisaabadi Bozchaloei, G., et al., *Effect of oxide bifilms on the mechanical properties of cast Al–7Si–0.3Mg alloy and the roll of runner height after filter on their formation.* Materials Science and Engineering: A, 2012. **548**: p. 99-105.
138. Khalili, A. and K. Kromp, *Statistical Properties of Weibull Estimators.* Journal of Materials Science, 1991. **26**(24): p. 6741-6752.
139. Li, T., W.D. Griffiths, and J. Chen, *Weibull Modulus Estimated by the Non-linear Least Squares Method: A Solution to Deviation Occurring in Traditional Weibull Estimation.* Metallurgical and Materials Transactions A: Physical Metallurgy and Materials Science, 2017. **48**(11): p. 5516-5528.
140. The MathWorks, I. *fmincon: Find minimum of constrained nonlinear multivariable function*. 2019 2/8/2019]; Available from: https://www.mathworks.com/help/optim/ug/fmincon.html.

Appendix A. Error associated with point load approximation for loading of elastic half space

The displacement at the base of a fibril generated by a point load applied to the backing layer at the center of the base of a neighboring fibril is given by the first term of (3.5). An improved approximation of the real system is obtained if we consider uniform pressure applied to the circular section at the base of the neighboring fibril. This is also provided by Johnson [90], with the ratio between this solution and the point load approximation given by

$$\frac{\left(u_i^{\mathrm{BL}}\right)_j}{\left(u_i^{\mathrm{BL}}\right)_j^{\mathrm{A}}} = \frac{4{r_{ij}}^2}{\pi a^2}\left[\mathrm{E}\left(\frac{a}{r_{ij}}\right) - \left(1 - \frac{{r_{ij}}^2}{a^2}\right)\mathrm{K}\left(\frac{a}{r_{ij}}\right)\right] \tag{A.1}$$

where $\left(u_i^{\mathrm{BL}}\right)_j^{\mathrm{A}}$ is the displacement computed by the first term in (3.5), and K and E are the complete elliptic integrals of the first and second kind, respectively. The error associated with use of the point load approximation is therefore

$$e_{ij} = \left|\frac{\left(u_i^{\mathrm{BL}}\right)_j}{\left(u_i^{\mathrm{BL}}\right)_j^{\mathrm{A}}} - 1\right| \tag{A.2}$$

which is a function of r_{ij}/a. We find that the error is maximum for the minimum fibril separation, $r_{ij} = 2a$, and is 3.34 %.

Appendix B. Verification of uniform load distribution

Figure B.1. is a histogram showing the number of neighbors in contact at detachment of each fibril in the array. The experimental data is compared to three simulated cases using the real areal geometry of the array. The first simulated case corresponds to random detachment, as would be expected if the fibrils detachments were uncoupled and the load distribution were uniform. One representative test is shown. The three remaining cases are designed to mimic detachment modes which may result from non-uniform load distributions. The array edge detachment is characteristic of backing layer compliance [70]. The sequence is based upon the position relative to the array center, from furthest to closest. The peel-like detachments are characteristic of misalignment [115, 125], occurring according to position along a single axis. Two such detachment sequences are shown, corresponding to alignment with the axis along which the fibril separation is d and the axis along which it is $\sqrt{2}d$, respectively.

Fibrils in the bulk of a square array have four nearest neighbors. If the detachment is random then there is a steady reduction in the number of neighbors in contact when a fibril detaches. The distribution is fairly uniform, with a slight bias toward lower numbers of neighbors in contact. Conversely, all simulated sources of correlation in the detachment sequence lead to a clear peak of two attached neighbors. The similarity of the random simulated data and the experimental data is clear, leading to the conclusion that the load distribution is uniform and the detachment sequence is controlled by the distribution in fibril adhesive strength.

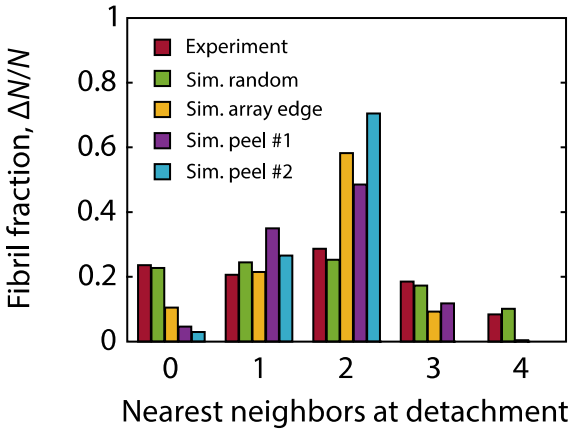

Figure B.1. Histogram of nearest neighbors in contact at detachment for all fibrils in the array. The experimental data is compared to three simulated cases, a random detachment process, an array edge detachment, and a peel-like detachment from one side of the array to the other.

Appendix C. Derivation of failure probability using the Poisson postulates

The Poisson postulates are as follows – (1) the number of critical defects in non-overlapping regions are independent; (2) The probability of a critical defect existing within the increment of perimeter, δS, is proportional to its size; (3) The probability of multiple critical defects within this increment is negligible. The second postulate yields

$$\phi(f, \delta S) = \lambda(f, S)\delta S \tag{C.1}$$

where λ is defect density, i.e. the number of critical defects per unit length. This is determined by the local stress state, leading to the dependence on both the remote load, f, and position within the region of interest, S. The size dependence of the failure probability is obtained by considering an incremental change in the size of the region of interest, such that

$$1 - \phi(f, S + \delta S) = (1 - \phi(f, S))(1 - \phi(f, \delta S)) \tag{C.2}$$

where $1 - \phi$ is the survival probability. Substituting (C.1) we obtain

$$1 - \phi(f, S + \delta S) = (1 - \phi(f, S))(1 - \lambda(f, S)\delta S) \tag{C.3}$$

In the limit $\delta S \to 0$ we obtain a differential equation for the failure probability

$$\phi'(f, S) + \lambda(f, S)\phi(f, S) = \lambda(f, S) \tag{C.4}$$

for which the solution is

$$\phi(f,S) = 1 - \exp\left(-\int_V \lambda(f,S)\,\mathrm{d}S\right) \tag{C.5}$$

The defect density, λ, is often stated in the form

$$\lambda = \int_f g(f,S)\mathrm{d}f \tag{C.6}$$

where $g(f,S)$ is the number of defects per unit volume which yield a detachment force between f and $f + \mathrm{d}f$. This leads to

$$\phi(f,S) = 1 - \exp\left(-\int_\sigma \int_V g(f,S)\,\mathrm{d}S\mathrm{d}f\right) \tag{C.7}$$

Appendix D. Fitting method for detachment probability

It is possible to linearize (5.8) for the purpose of least squares fitting. However, this transformation is found to cause significant bias when small deviations occur at low strength (e.g. [135-137]). In general, maximum likelihood [138] or non-linear least squares methods [139] are preferred. We proceed with the latter on the basis of general observation of lower root mean square error. A constrained minimization is performed using a sequential quadratic programming method in the Matlab subroutine 'fmincon' [140]. The constraints imposed are $0 \leq u_0 \leq \infty$, $1 \leq m \leq \infty$, and, where the third parameter is involved, $0.32 \leq \propto \leq 1$. Error estimates on the statistical properties are obtained by performing Monte Carlo simulations, based on randomly resampling N fibril adhesive strengths from the resulting distribution and refitting [138]. In each case the standard deviation is very small, $< 0.01\,\%$, and so is not reported on a case by case basis.

Appendix E. Monte Carlo simulation of bimodal distribution

A Monte Carlo simulation is performed to generate a discrete bimodal probability distribution. Two strengths, one from each distribution, are randomly sampled. This is repeated for n samples, with only αn being assigned a strength from the secondary mode. For each fibril, the minimum of the two strengths persists in the resulting discrete bimodal distribution. The distribution from which the lower strength is obtained is stored along with the strength itself. This permits the generation of a histogram, decomposed by defect type. Such a histogram can be compared qualitatively to the experimental result of Figure 5.5.

Figure E.1 shows histograms of fibril adhesive strength for two combinations of bimodal statistical parameters. The first combination, shown in Figure E.1a, are those obtained in Section 5.3.2 by combining fitting of (5.8) to mean order ranked data for the center defect population with fitting of (5.13) to raw data to obtain the remaining three parameters. The other combination, shown in Figure E.1b, is obtained by fitting raw data to (5.13) for all five parameters, with the constraints $0 \leq u_{0i} \leq \infty$, $1 \leq m_i \leq \infty$, and $0.32 \leq \propto \leq 1$. This also results in a high-quality fit, $\Sigma = 0.0102$, and yields almost identical behavior when considering the cumulative strength distribution. However, when decomposed by defect type we observe that the behavior is very different. Only in Figure E.1a do we observe qualitative similarity to the experimental result of Figure 5.5. This highlights the issue fitting of (5.13) without fibril-by-fibril knowledge of the detachment mechanism, and gives confidence in the result obtained by using the mean order ranking method to reduce the parameter space before fitting.

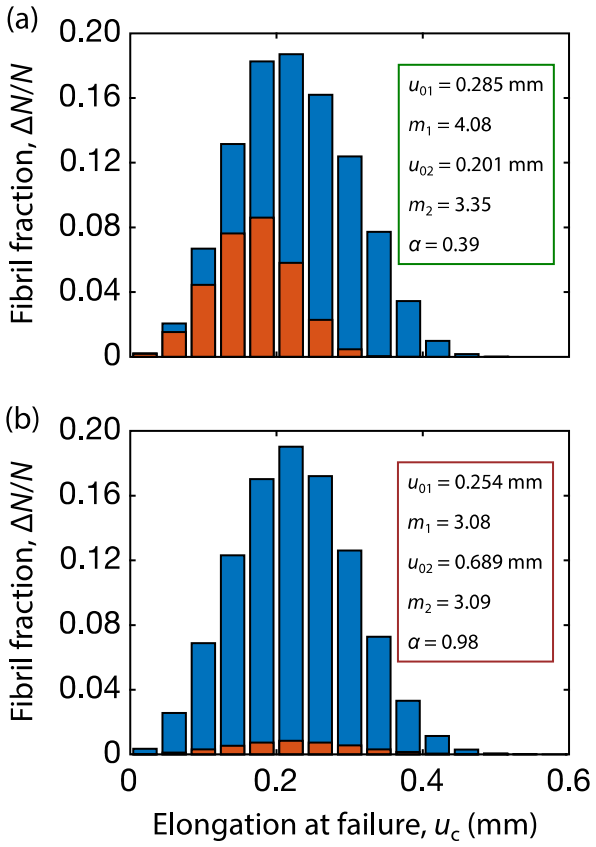

Figure E.1. Histogram of elongation at detachment, u_c, produced by Monte Carlo simulation for two partially concurrent defect populations exhibiting the statistical parameters given in the insets of (a) and (b). To avoid discretization error, the number of samples $n = 100000$. The bin size $\Delta u_c = 0.04$ mm.